

AD-A171 564

CHALCOGENIDE GLASSES PART 4 CRYSTALLIZATION AND GLASS  
TRANSITION CHARACTE. (U) AIR FORCE WRIGHT AERONAUTICAL  
LABS WRIGHT-PATTERSON AFB OH K WHITE ET AL. JUN 86

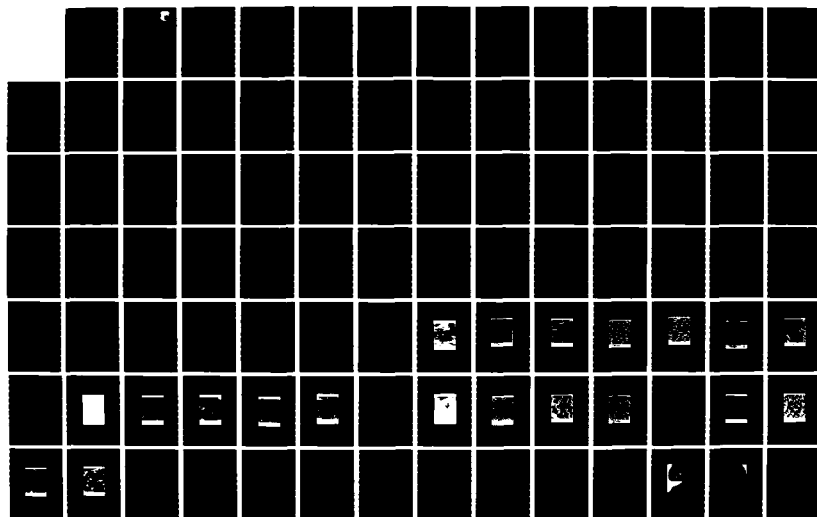
1/2

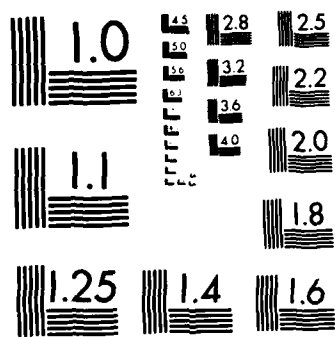
UNCLASSIFIED

AFMRL-TR-86-4075

F/G 1/2

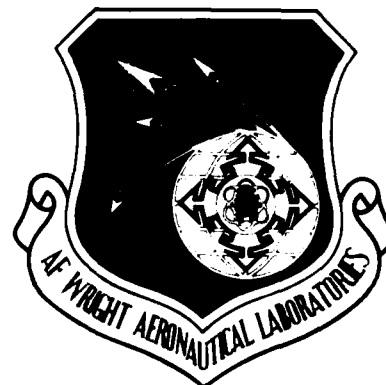
NL





MICROCOPY RESOLUTION TEST CHART

AFWAL-TR-86-4075

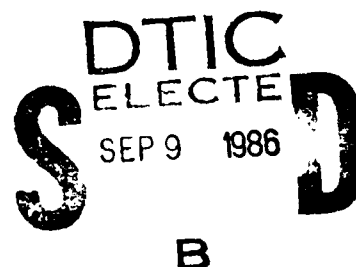


CHALCOGENIDE GLASSES (PART IV)

CRYSTALLIZATION AND GLASS TRANSITION CHARACTERISTICS  
IN  $\text{As}_{2-x}\text{Sb}_x\text{S}_3$  GLASS-FORMING SYSTEM

Koto White and Robert L. Crane  
Laser Hardened Materials Branch  
Electromagnetic Materials Division

James A. Snide  
University of Dayton  
Dayton, ohio 45469



June 1986

Final Report for Period 1 November 1983 - 31 March 1986

Approved for public release; distribution unlimited

MATERIALS LABORATORY  
AIR FORCE WRIGHT AERONAUTICAL LABORATORIES  
AIR FORCE SYSTEMS COMMAND  
WRIGHT-PATTERSON AIR FORCE BASE, OHIO 45433

86 9 09 972

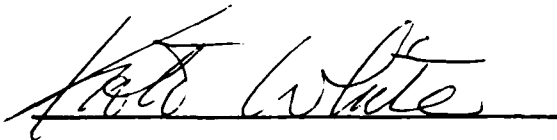
AD-A171 564

DTIC FILE COPY

## NOTICE

When Government drawings, specifications, or other data are used for any purpose other than in connection with a definitely related Government procurement operation, the United States Government thereby incurs no responsibility nor any obligation whatsoever; and the fact that the government may have formulated, furnished, or in any way supplied the said drawings, specifications, or other data, is not to be regarded by implication or otherwise as in any manner licensing the holder or any other person or corporation, or conveying any rights or permission to manufacture, use, or sell any patented invention that may in any way be related thereto.

This technical report has been reviewed and is approved for publication.



Koto White  
Project Engineer



William R. Woody, Acting Chief  
Laser Hardened Materials Branch  
Electromagnetic Materials Div.

FOR THE COMMANDER:



William C. Kessler, Acting Chief  
Electromagnetic Materials Division

"If your address has changed, if you wish to be removed from our mailing list, or if the addressee is no longer employed by your organization please notify AFWAL/MLPJ, W-P AFB, OH 45433 to help maintain a current mailing list".

Copies of this report should not be returned unless return is required by security considerations, contractual obligations, or notice on a specific document.

Unclassified

SECURITY CLASSIFICATION OF THIS PAGE

AD A171 564

## REPORT DOCUMENTATION PAGE

1a. REPORT SECURITY CLASSIFICATION Unclassified			1b. RESTRICTIVE MARKINGS	
2a. SECURITY CLASSIFICATION AUTHORITY			3. DISTRIBUTION/AVAILABILITY OF REPORT  Approved for public release; distribution unlimited	
2b. DECLASSIFICATION/DOWNGRADING SCHEDULE				
4. PERFORMING ORGANIZATION REPORT NUMBER(S)  AFWAL-TR-86- 4075			5. MONITORING ORGANIZATION REPORT NUMBER(S)	
6a. NAME OF PERFORMING ORGANIZATION Air Force Wright Aeronautical Laboratories, Material's Lab.		6b. OFFICE SYMBOL (If applicable) AFWAL/MLPJ	7a. NAME OF MONITORING ORGANIZATION	
6c. ADDRESS (City, State and ZIP Code)  Wright-Patterson Air Force Base Ohio 45433			7b. ADDRESS (City, State and ZIP Code)	
8a. NAME OF FUNDING/SPONSORING ORGANIZATION		8b. OFFICE SYMBOL (If applicable)	9. PROCUREMENT INSTRUMENT IDENTIFICATION NUMBER	
8c. ADDRESS (City, State and ZIP Code)			10. SOURCE OF FUNDING NOS.	
			PROGRAM ELEMENT NO.	PROJECT NO.
			62102F	2422
			TASK NO.	WORK UNIT NO.
			242204	24220401
11. TITLE (Include Security Classification) Chalcogenide Glasses (part IV) Crystallization and Glass Transition				
12. PERSONAL AUTHOR(S) Characteristics in As <sub>2</sub> Sb <sub>2</sub> S <sub>3</sub> Glass-Forming System. Koto White, Robert L. Crane, and James A. Snide				
13a. TYPE OF REPORT Final		13b. TIME COVERED FROM 11-1-83 TO 3-31-86		14. DATE OF REPORT (Yr., Mo., Day) 1986 June
				15. PAGE COUNT 167
16. SUPPLEMENTARY NOTATION				
17. COSATI CODES			18. SUBJECT TERMS (Continue on reverse if necessary and identify by block number)	
FIELD	GROUP	SUB GR	chalcogenide glass, crystallization, glass transition, kinetic parameter, DSC, SEM, X-ray, Film, arsenic trisulfide antimony trisulfide	
20	06	-		
19. ABSTRACT (Continue on reverse if necessary and identify by block number) The crystallization characteristics of As <sub>2</sub> Sb <sub>2</sub> S <sub>3</sub> chalcogenide glasses with nominal compositions ranging from x=0.0 to 2.0 in a melt quenched bulk form and a thin film form were studied, and a self-consistent model of crystallization mechanism was developed. Scanning electron microscopy and X-ray diffraction analysis were used to examine the microstructure and phases present as a function of composition. Differential scanning calorimetry, both in isothermal and dynamic mode, was utilized to determine the kinetic parameters, glass forming tendency, and glass transition characteristics as a function of composition. All results for the melt quenched bulk glasses were consistent with the proposed model in which; (1) the glasses exhibit two phase heterogeneity consisting of Sb <sub>2</sub> S <sub>3</sub> phase and As <sub>2</sub> S <sub>3</sub> matrix phase, (2) the nucleation sites are at the surface of the bulk in the Sb <sub>2</sub> S <sub>3</sub> phase, and (3) the Sb <sub>2</sub> S <sub>3</sub> crystals grow in the glassy As <sub>2</sub> S <sub>3</sub> matrix by diffusion of antimony atoms through As <sub>2</sub> S <sub>3</sub> phase, and subsequent inter-connection of Sb <sub>2</sub> S <sub>3</sub> phase.				
20. DISTRIBUTION/AVAILABILITY OF ABSTRACT  UNCLASSIFIED/UNLIMITED <input checked="" type="checkbox"/> SAME AS RPT <input type="checkbox"/> DTIC USERS <input type="checkbox"/>			21. ABSTRACT SECURITY CLASSIFICATION  Unclassified	
22a. NAME OF RESPONSIBLE INDIVIDUAL  White, Koto			22b. TELEPHONE NUMBER (Include Area Code) (513)255-3228	22c. OFFICE SYMBOL  AFWAL/MLPJ

DD FORM 1473, 83 APR

EDITION OF 1 JAN 73 IS OBSOLETE

Unclassified  
SECURITY CLASSIFICATION OF THIS PAGE

Copy 1 Unclassified

SECURITY CLASSIFICATION OF THIS PAGE

The experimental results with the vapor deposited film samples suggested a slightly different model, in which no heterogeneity existed in the as-deposited state.



✓

DTIC  
ELECTE  
SEP 9 1986  
S B

DTIC	
ELECTE	
SEP 9 1986	
S B	
A-1	

Unclassified

SECURITY CLASSIFICATION OF THIS PAGE

## FOREWORD

This report describes in-house research performed at the Laser Hardened Materials Branch of the Materials Laboratory, Air Force Wright Aeronautical Laboratories, Wright-Patterson Air Force Base, from November 1 1983 to March 31 1986 under work unit number 24220401. This is the part IV of a four part study in chalcogenide glasses.

The authors are grateful to Messrs. George F. Schmitt and William R. Woody, Drs. William C. Kessler and Merrill L. Minges of the Materials Laboratory for thier continuing support and encouragement throughout the course of this research. They wish to acknowledge the helpful assistance and encouragement of Drs. Ivan J. Goldfarb, Joseph P. Gallagher, John C. Wurst, John W. McCloskey, Ronald A. Servais, Binod Kumar, and Charles L. Strecker.

Their acknowledgement extends to Mr. T. Kerschner for conducting the chemical analysis, Messrs. R. Bacon and E. Harper of SRL for microscopy, Mr. J. Ray of glass shop for glass sealing, Mr. M. Dornbusch of PME for instrumental assistance and Dr. R. Ruh for letting us use the X-ray equipment, which is under his care.

## TABLE OF CONTENTS

SECTION	PAGE
I. INTRODUCTION.....	1
1. THEORY AND BACKGROUND.....	3
a. Chalcogenide Glasses.....	3
b. Arsenic-Antimony Chalcogenides.....	4
c. Glass Formation.....	12
d. Crystallization.....	13
e. Glass Transition.....	19
II. EXPERIMENT AND DATA ANALYSIS PROCEDURE.....	25
1. SPECIMEN PREPARATION.....	25
a. Bulk Specimens.....	25
b. Film Specimens.....	26
2. THERMAL ANALYSIS.....	28
a. Dynamic Heating Experiments.....	29
b. Isothermal Experiments.....	32
c. Error Analysis for Activation Energy Calculations.....	37
3. OTHER CHARACTERIZATIONS.....	39
III. RESULTS AND DISCUSSION.....	41
1. CHEMICAL COMPOSITIONS.....	41
2. X-RAY ANALYSIS.....	43
3. SCANNING ELECTRON MICROSCOPY.....	48
4. THERMAL ANALYSIS.....	67
a. Characteristic Temperatures ( $T_g$ , $T_c$ , and $T_1$ ) Determined by the Dynamic Heating Method	67
b. Kinetics of Crystallization .....	91
c. Activation Energy of Glass Transition....	100
d. Effect of Annealing on Glass Transition..	102
e. A Self-Consistent Model of Crystalliza- tion Mechanism.....	104
IV. SUMMARY.....	109
V. FUTURE WORK.....	113

## APPENDIX

A.	THERMAL ANALYSIS.....	114
B.	EFFECT OF DEPOSITION RATE ON PHYSICAL AND STRUCTURAL PROPERTIES OF $\text{As}_2\text{S}_3$ FILMS.....	116
C.	CRYSTALLIZATION KINETICS DATA.....	125
	REFERENCES.....	150

# LIST OF ILLUSTRATIONS

1.	As-Sb Phase Diagram.....	5
2.	Glass-Forming Region in As-Sb-S System.....	7
3.	As <sub>2</sub> Se <sub>3</sub> -Sb <sub>2</sub> Se <sub>3</sub> Phase Diagram.....	9
4.	Glass-Forming Region in As-Sb-Se system.....	11
5.	Free Energy Change During Crystallization Process .....	14
6.	Thermodynamic Properties as a Function of Temperature.....	21
7.	Thermodynamic Properties(a) and Specific Heat(b) of Glasses as a Function of Temperature at Different Heating and Cooling Rate.....	22
8.	Effect of DSC Sample Weight on Measured Melting Temperature of Lead.....	30
9.	An Example of Isothermal Crystallization Data.....	33
10.	Effect of Sample Weight on Isothermal Crystallization.....	35
11.	Effect of Sample's Surface Area on Isothermal Crystallization.....	36
12.	Glass-Forming Region in As <sub>2-x</sub> Sb <sub>x</sub> S <sub>3</sub> for different Cooling Rates.....	47
13a.	Microstructure of Slow Cooled Sb <sub>2</sub> S <sub>3</sub> (unetched).....	49
13b.	Microstructure of Slow Cooled As <sub>0.2</sub> Sb <sub>1.8</sub> S <sub>3</sub> (unetched).....	50
13c.	Microstructure of Slow Cooled As <sub>0.4</sub> Sb <sub>1.6</sub> S <sub>3</sub> (unetched).....	51
13d.	Microstructure of Slow Cooled As <sub>0.6</sub> Sb <sub>1.4</sub> S <sub>3</sub> (unetched).....	52
13e.	Microstructure of Slow Cooled As <sub>0.6</sub> Sb <sub>1.4</sub> S <sub>3</sub> (etched).....	53

13f.	Microstructure of Slow Cooled $\text{As}_{0.8}\text{Sb}_{1.2}\text{S}_3$ (unetched).....	54
13g.	Microstructure of Slow Cooled $\text{As}_{0.8}\text{Sb}_{1.2}\text{S}_3$ (etched).....	55
13h.	Microstructure of Slow Cooled $\text{As}_{2-x}\text{Sb}_x\text{S}_3$ where $x = 1.1, 0.8, 0.6, \text{ and } 0.4$ (unetched).....	57
13i.	Microstructure of Slow Cooled $\text{As}_{2-x}\text{Sb}_x\text{S}_3$ where $x < 1.1$ (etched).....	58
14a.	Microstructure of Quenched $\text{As}_{0.2}\text{Sb}_{1.8}\text{S}_3$ (etched).....	59
14b.	Microstructure of Quenched $\text{As}_{0.4}\text{Sb}_{1.6}\text{S}_3$ (unetched).....	60
14c.	Microstructure of Quenched $\text{As}_{0.4}\text{Sb}_{1.6}\text{S}_3$ (etched).....	61
14d.	Microstructure of Quenched $\text{As}_{2-x}\text{Sb}_x\text{S}_3$ where $x < 1.4$ (unetched).....	63
14e.	Microstructure of Quenched $\text{As}_{2-x}\text{Sb}_x\text{S}_3$ where $x < 1.4$ (etched).....	64
15a.	Microstructure of Slow Cooled Sulfur Deficient $\text{As}_{1.0}\text{Sb}_{1.0}\text{S}_{2.66}$ (unetched).....	65
15b.	Microstructure of Slow Cooled Sulfur Deficient $\text{As}_{1.0}\text{Sb}_{1.0}\text{S}_{2.66}$ (etched).....	66
15c.	Microstructure of Quenched Sulfur Deficient $\text{As}_{1.0}\text{Sb}_{1.0}\text{S}_{2.67}$ (unetched).....	68
15d.	Microstructure of Quenched Sulfur Deficient $\text{As}_{1.0}\text{Sb}_{1.0}\text{S}_{2.67}$ (etched).....	69
15e.	Microstructure of Quenched Sulfur Deficient $\text{As}_{1.2}\text{Sb}_{0.8}\text{S}_{2.55}$ (unetched).....	70
15f.	Microstructure of Quenched Sulfur Deficient $\text{As}_{1.2}\text{Sb}_{0.8}\text{S}_{2.55}$ (etched).....	71
16.	DSC Traces for Quenched Stoichiometric Specimens.....	72
17.	DSC Traces for Slow Cooled Stoichiometric Specimens.....	74

18.	DSC Trace for Quenched Sulfur Deficient Specimen.....	75
19.	DSC Trace for Slow Cooled Sulfur Deficient Specimen.....	76
20.	As-S Phase Diagram.....	77
21.	DSC Traces for Vapor Deposited Films.....	78
22a.	DSC Traces- Comparison of Bulk Sample and Powdered Sample of the Same Composition.....	80
22b.	Crystallization Starting at the Surface of $\text{As}_{0.8}\text{Sb}_{1.2}\text{S}_3$ Bulk Specimen.....	81
22c.	Dendritic Growth in the Surface Crystallization of $\text{As}_{0.8}\text{Sb}_{1.2}\text{S}_3$ Bulk Specimen.....	82
23.	Glass Transition Onset Temperature, $T_g$ , as a Function of Composition for Bulk Samples.....	87
24.	Temperature at the Maximum Crystallization Rate, $T_c$ , as a Function of Composition for Various Forms of Samples.....	88
25.	Liquidus Temperature, $T_l$ , as a Function of Composition.....	90
26.	Hruby's Parameter as a Function of Composition for Various Forms of Samples.....	92
27.	Crystallization Starting Around the Internal Pores.....	96
28.	Isothermal Trace for Films.....	98
29.	Activation Energy of Glass Transition, $H_a$ , as a Function of Composition for Various Forms of Samples.....	101
30.	Area under $T_g$ Peak, $Q$ , as a Function of Annealing Time for Different Compositions (Bulk Samples).....	103
31a.	Model of Crystallization Mechanism Antimony Rich Compositions.....	107
31b.	Model of Crystallization Mechanism Arsenic Rich Compositions.....	107

32.	Deposition Rate as a Function of Source Temperature.....	119
33.	Sulfur Stoichiometry, $x$ , as a Function of Film Deposition Rate in $\text{As}_2\text{S}_x$ Films.....	120
34.	DSC Traces for Films and a Bulk Arsenic Sulfide.....	122
35.	X-Ray Diffraction Patterns for Films and a Bulk Arsenic Sulfide.....	123
36a.	Dynamic Heating Crystallization Data for Activation Energy Calculation ( $\text{As}_{0.8}\text{Sb}_{1.2}\text{S}_3$ Bulk).....	126
36b.	Dynamic Heating Crystallization Data for Activation Energy Calculation ( $\text{As}_{0.6}\text{Sb}_{1.4}\text{S}_3$ Bulk).....	127
36c.	Dynamic Heating Crystallization Data for Activation Energy Calculation ( $\text{As}_{0.4}\text{Sb}_{1.6}\text{S}_3$ Bulk).....	128
36d.	Dynamic Heating Crystallization Data for Activation Energy Calculation ( $\text{As}_{1.2}\text{Sb}_{0.8}\text{S}_{2.55}$ Bulk).....	129
36e.	Dynamic Heating Crystallization Data for Activation Energy Calculation ( $\text{As}_{1.0}\text{Sb}_{1.0}\text{S}_{2.67}$ Bulk).....	130
36f.	Dynamic Heating Crystallization Data for Activation Energy Calculation ( $\text{As}_{0.8}\text{Sb}_{1.2}\text{S}_3$ Film).....	131
36g.	Dynamic Heating Crystallization Data for Activation Energy Calculation ( $\text{As}_{0.4}\text{Sb}_{1.6}\text{S}_3$ Film).....	132
36h.	Dynamic Heating Crystallization Data for Activation Energy Calculation ( $\text{Sb}_2\text{S}_3$ Film).....	133
37a.	Isothermal Crystallization Data for Activation Energy Calculation Step I ( $\text{As}_{0.8}\text{Sb}_{1.2}\text{S}_3$ Bulk)...	134
37b.	Isothermal Crystallization Data for Activation Energy Calculation Step II ( $\text{As}_{0.8}\text{Sb}_{1.2}\text{S}_3$ Bulk)...	135

37c.	Isothermal Crystallization Data for Activation Energy Calculation Step I ( $\text{As}_{0.6}\text{Sb}_{1.4}\text{S}_3$ Bulk)...	136
37d.	Isothermal Crystallization Data for Activation Energy Calculation Step II( $\text{As}_{0.6}\text{Sb}_{1.4}\text{S}_3$ Bulk)...	137
37e.	Isothermal Crystallization Data for Activation Energy Calculation Step I ( $\text{As}_{0.4}\text{Sb}_{1.6}\text{S}_3$ Bulk)...	138
37f.	Isothermal Crystallization Data for Activation Energy Calculation Step II( $\text{As}_{0.4}\text{Sb}_{1.6}\text{S}_3$ Bulk)...	139
37g.	Isothermal Crystallization Data for Activation Energy Calculation Step I ( $\text{As}_{1.2}\text{Sb}_{0.8}\text{S}_{2.55}$ Bulk).	140
37h.	Isothermal Crystallization Data for Activation Energy Calculation Step II( $\text{As}_{1.2}\text{Sb}_{0.8}\text{S}_{2.55}$ Bulk).	141
37i.	Isothermal Crystallization Data for Activation Energy Calculation Step I ( $\text{As}_{1.0}\text{Sb}_{1.0}\text{S}_{2.67}$ Bulk).	142
37j.	Isothermal Crystallization Data for Activation Energy Calculation Step II( $\text{As}_{1.0}\text{Sb}_{1.0}\text{S}_{2.67}$ Bulk).	143
37k.	Isothermal Crystallization Data for Activation Energy Calculation Step I ( $\text{As}_{0.8}\text{Sb}_{1.2}\text{S}_3$ Bulk)...	144
37l.	Isothermal Crystallization Data for Activation Energy Calculation Step II( $\text{As}_{0.8}\text{Sb}_{1.2}\text{S}_3$ Bulk)...	145
37m.	Isothermal Crystallization Data for Activation Energy Calculation Step I ( $\text{As}_{0.4}\text{Sb}_{1.4}\text{S}_3$ Film)...	146
37n.	Isothermal Crystallization Data for Activation Energy Calculation Step II( $\text{As}_{0.4}\text{Sb}_{1.6}\text{S}_3$ Film)...	147
37o.	Isothermal Crystallization Data for Activation Energy Calculation Step I ( $\text{Sb}_2\text{S}_3$ Film).....	148
37p.	Isothermal Crystallization Data for Activation Energy Calculation Step II( $\text{Sb}_2\text{S}_3$ Film).....	149

## LIST OF TABLES

1.	List of Sample Compositions and Analysis Conducted on Samples.....	42
2.	Measured Lattice Spacing Values from X-ray Analysis.....	44
3.	Summary of DSC Data - T <sub>g</sub> , T <sub>c</sub> , and T <sub>i</sub> Values Measured at Four Different Heating Rate.....	84
4.	Summary of Calculated Kinetic Parameters.....	94

## I. INTRODUCTION

The chalcogenide glasses, which are transparent in the infrared wavelength range, are being used in commercial optical applications. Among the chalcogenide compositions, arsenic trisulfide ( $\text{As}_2\text{S}_3$ ) glass has been utilized most frequently in bulk infrared optics and optical coatings, because of its excellent transmission, great glass-forming tendency, and resistance to moisture and chemicals[Ref.1-3].

A graded refractive index, which is required in some applications, may be produced in the arsenic trisulfide glass of both bulk and thin film forms by gradually replacing arsenic component with chemically similar antimony atoms. This approach will fail if the resultant glass crystallizes or undergoes a gross phase separation, because they cause scattering.

Only a few references exist for  $\text{As}_{2-x}\text{Sb}_x\text{S}_3$  system, and no data on its crystallization characteristics have been found [Ref.4-7]. More information can be found for the selenide glass counterpart,  $\text{As}_{2-x}\text{Sb}_x\text{Se}_3$  system, and the data should aid in the understanding of the sulfide glass system because these two systems are chemically and structurally very similar [Ref.8-12]. The crystallization characteristics of these two glass systems, on the contrary, should be quite different because the  $\text{As}_2\text{Se}_3$  glass has greater tendency to crystallize than the  $\text{As}_2\text{S}_3$  glass [Ref.13-15].

Several discrepancies have been found in the literature for the sulfide and selenide glass-forming systems, and these discrepancies need to be clarified in order to fully understand the crystallization and glass formation characteristics of these glasses. First discrepancy was in the structure of glasses. There have been experimental data suggestive of a two phase microheterogeneous glass structure [Ref.5 and 6], while other researchers reported an absence of the phase separation and microheterogeneities [Ref.11 and 12]. Secondly, among the data supporting the existence of a two phase glass structure, some data were best interpreted with no interaction term between two phases [Ref.7], while others should be explained in terms of an interaction between them [Ref.5 and 6]. Third discrepancy was in the structure of these compositions in the crystallized state. A totally immiscible phase diagram has been reported for  $\text{As}_2\text{Se}_3\text{-Sb}_2\text{Se}_3$  system [Ref.8], while other data seem to indicate the formation of a solid solution [Ref.11 and 12]. The phase diagram information for the  $\text{As}_2\text{S}_3\text{-Sb}_2\text{S}_3$  system could not be located.

The purpose of this study was to understand the crystallization mechanism of  $\text{As}_{2-x}\text{Sb}_x\text{S}_3$  glasses in a melt quenched bulk form and a thin film form. This consisted of the following; (1) clarifying the questions concerning the nature of the glassy state, more specifically the possible existence of heterogeneity and interaction between phases.

This will be achieved by a microscopy and by studies of glass transition and glass forming tendency as a function of composition using differential scanning calorimeter, (2) Verifying the totally immiscible crystallized state using SEM and X-ray diffraction technique, and (3) obtaining crystallization kinetic parameters as a function of composition to aid understanding of crystallization mechanism. A self consistent model of crystallization mechanism was developed as a result of this study.

The remainder of Chapter I provides a detailed summary of previous works in arsenic antimony chalcogenide glasses, and also provided are the background information and brief theory of the most frequently used terms hereafter throughout the thesis.

## 1. THEORY AND BACKGROUND INFORMATION

### a. Chalcogenide Glasses

Chalcogenide glasses are glasses based on sulfur, selenium and tellurium. Most of the early studies were conducted on the arsenic chalcogenides because of their excellent glass forming ability. In addition to the arsenic chalcogenides, many chalcogenides containing elements from Group IIIA, IVA, VA and VIIA of the periodic table have been discovered to form glasses over wide ranges of compositions, in recent years [Ref.1-3].

A great deal of information, both experimental and theoretical, on oxide glass formation and crystallization

can be found in the literature, whereas papers on the chalcogenide glasses are rather scarce. The well known theories of glass formation, based on glass formers and modifiers [Ref.16], which explain the glass forming mechanism in the oxide glasses, do not seem to apply directly to the chalcogenide glasses.

Because these chalcogen elements form relatively weak bonds with other elements, the chalcogenide glasses in general are softer, electrically more conductive and optically transparent further into the infrared wavelength region as compared to the oxide and fluoride glasses. The compositions with desirable infrared optical properties and generally with high electrical resistance are useful in infrared optics (windows, optical fibers and laser components), whereas the glasses with semiconducting properties have applications as switching diodes, electrically activated memory cells, optical storage media and solar cells [Ref.2 and 3].

#### b. Arsenic-Antimony Chalcogenide

The elemental arsenic and antimony both belong to the Group VA of the periodic table and crystallize in rhombohedral symmetry, indicating their chemical and structural similarity. Though complete miscibility between such similar components are expected, a possible existence of a subliquidus immiscibility dome as shown in Figure 1

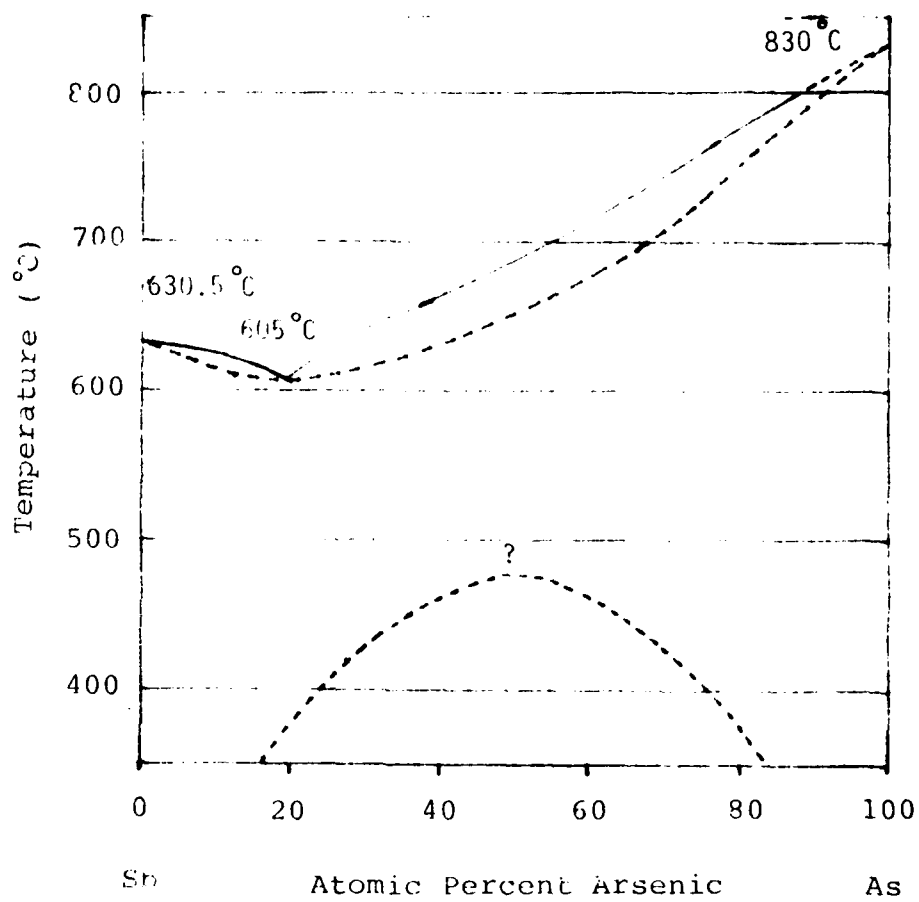


Figure 1. As-Sb Phase Diagram [Ref.17]

[Ref.17] has been reported. This is due to the substantial difference in their atomic radii (1.18Å for arsenic and 1.36<sup>0</sup>Å for antimony) [Ref.18]. Despite the chemical and structural similarity between elemental arsenic and antimony, their sulfur compounds,  $\text{As}_2\text{S}_3$  and  $\text{Sb}_2\text{S}_3$ , have different structures.  $\text{As}_2\text{S}_3$  is primary glassy and  $\text{Sb}_2\text{S}_3$  is crystalline under melt quenching synthesis conditions. The  $\text{As}_2\text{S}_3$  glass has very little tendency to crystallize and the crystallization of  $\text{As}_2\text{S}_3$  glass by annealing has not been reported. The crystal structure of the naturally occurring mineral  $\text{As}_2\text{S}_3$  (orpiment) and a synthetic  $\text{As}_2\text{S}_3$  prepared hydrothermally or under a high pressure is monoclinic while  $\text{Sb}_2\text{S}_3$  has the orthorhombic structure [Ref.19]. The ionic radii of antimony is 30 percent larger than that of arsenic in +3 valence state [Ref.18].

The glass-forming region in As-Sb-S system [Ref.4-6] is shown in Figure 2. The glass-forming region near Sb-S tie line is bound by a liquid-liquid immiscibility region in the sulfur rich side, and a crystallization region in the sulfur deficient side. Kawamoto and Tsuchihashi [Ref.5 and 6] reported that glasses formed up to 70 mole percent  $\text{Sb}_2\text{S}_3$  content on the  $\text{As}_2\text{S}_3$ - $\text{Sb}_2\text{S}_3$  tie line, when these compositions were air quenched in evacuated ampules. Stability of these glasses against crystallization was not studied. The infrared absorption spectra and the scattered X-ray intensity of these glasses were simply an addition of those

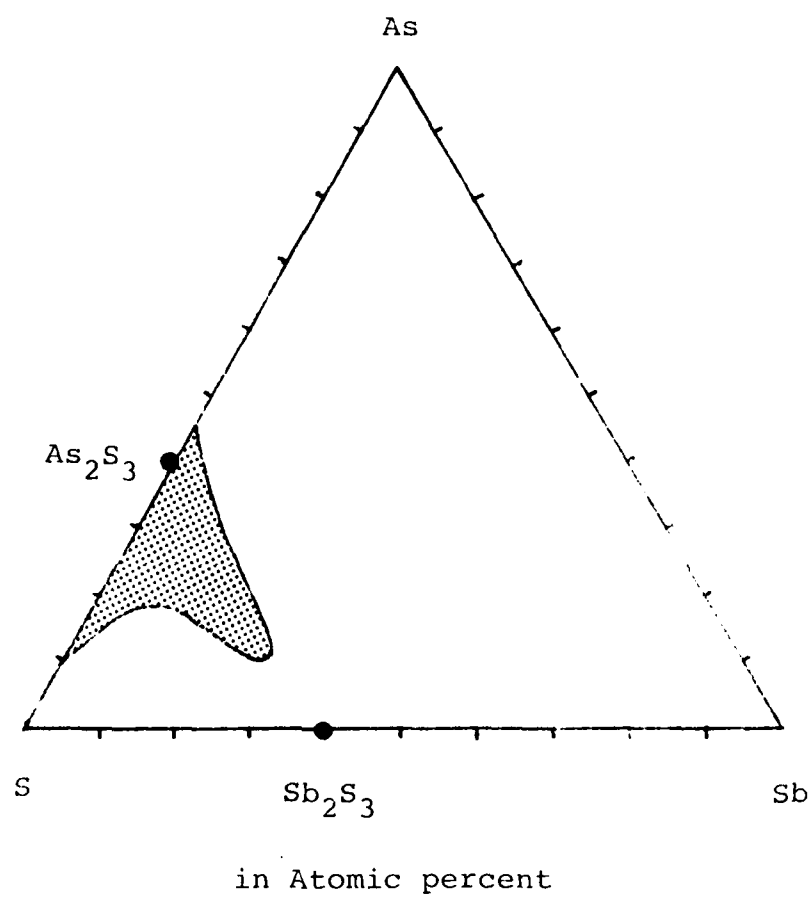


Figure 2. Glass-Forming Region in As-Sb-S System [Ref.5].

for  $\text{As}_2\text{S}_3$  and  $\text{Sb}_2\text{S}_3$ , suggesting a microheterogeneous glass structure consisting of independent  $\text{As}_2\text{S}_3$  and  $\text{Sb}_2\text{S}_3$  regions. However, they proposed an existence of As-S-Sb strained bonds connecting these two regions to explain their radial distribution and chemical dissolution (in conc. HCl) experiments. Also, they proposed a glass morphology with a continuous  $\text{As}_2\text{S}_3$  network and isolated  $\text{Sb}_2\text{S}_3$  phases, which become continuous only at high antimony concentrations. Tichy et al. [Ref.7] reported that the optical gap changed linearly with composition in this system, suggesting an absence of interactions between these two phases. The phase diagram of the corresponding stabilized system as well as the crystallization characteristics as a function of composition for As-Sb-S system have not been reported. Data on vapor deposited As-Sb-S films also are not reported.

More data are available for the selenide glass counterpart, As-Sb-Se system. The chemical, physical and structural properties of  $\text{As}_2\text{Se}_3$  and  $\text{Sb}_2\text{Se}_3$  are similar to those of  $\text{As}_2\text{S}_3$  and  $\text{Sb}_2\text{S}_3$ , except that the crystallization kinetics of the  $\text{As}_2\text{Se}_3$  glass is faster than that in the  $\text{As}_2\text{S}_3$  glass [Ref.13-15]. Berkes and Mayers [Ref.8] investigated the phase equilibria in  $\text{As}_2\text{Se}_3$ - $\text{Sb}_2\text{Se}_3$  system, utilizing a differential thermal analysis technique and a quench/X-ray technique. Their result, as shown in Figure 3, demonstrated a totally immiscible system with eutectic temperature near the melting point of  $\text{As}_2\text{Se}_3$  and with a two

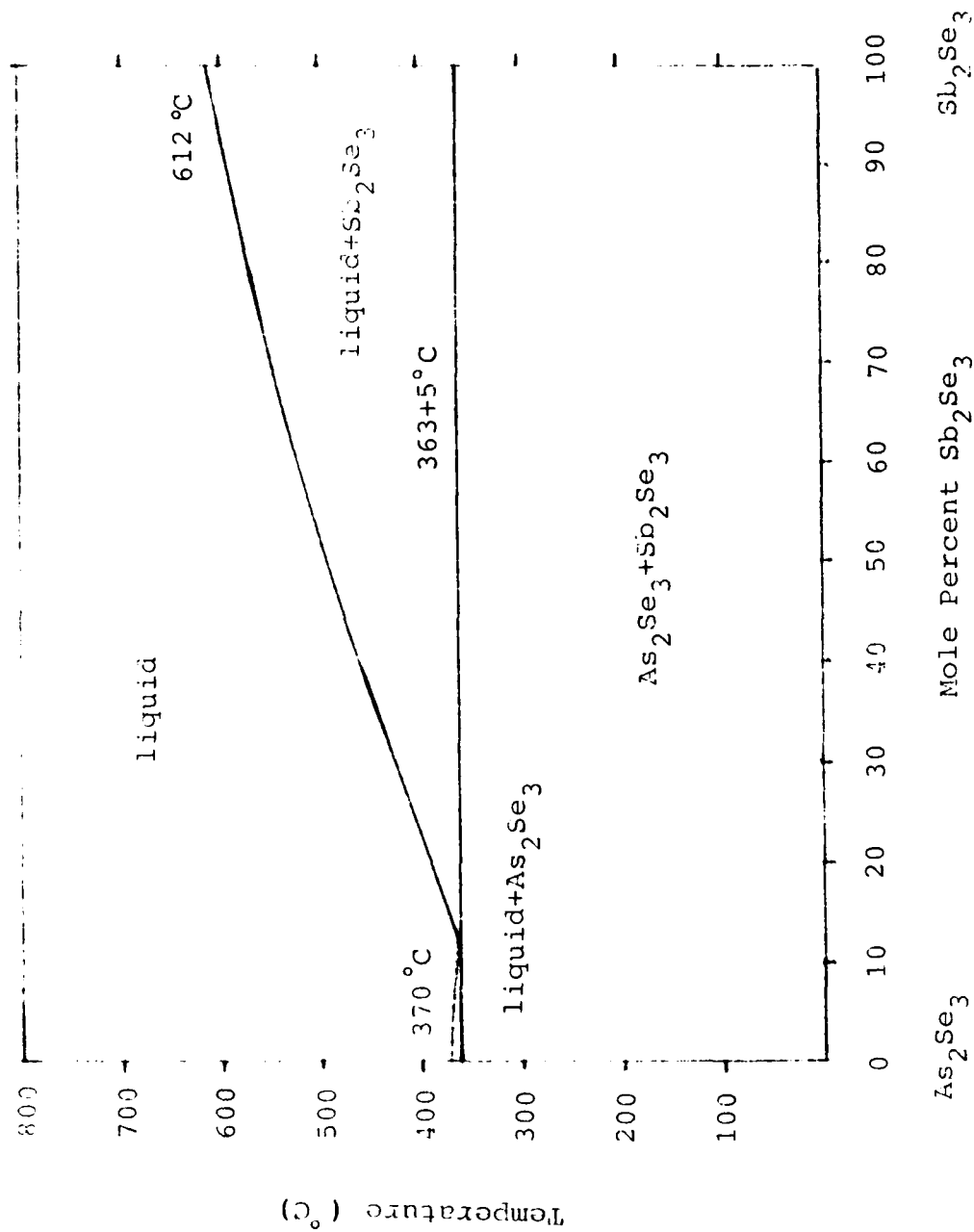


Figure 3.  $\text{As}_2\text{Se}_3$ - $\text{Sb}_2\text{Se}_3$  Phase Diagram [Ref. 8].

phase structure below the eutectic temperature throughout the compositional range. The glass-forming region in As-Sb-Se system under the air quenching condition (Figure 4) [Ref.8 and 9] has been reported, and the heterogeneous microstructure has been observed in high selenium compositions [Ref.9 and 10]. Platakis et al.[Ref.11 and 12] determined the apparent activation energy of  $\text{As}_{1.8}\text{Sb}_{0.2}\text{Se}_3$  to be 38 kcal/mole. The activation energies for compositions with higher antimony content, up to  $\text{AsSbSe}_3$ , were 50 kcal/mole and were composition independent. These activation energies were calculated from time required for the first crystal to become visible under microscope as a function of temperature. Their X-ray diffraction study of the crystallized system showed that the compositions with high arsenic content crystallized in monoclinic structure, antimony rich compositions crystallized in orthorhombic structure, and intermediate compositions exhibited both structures. Although this observation by itself indicates that the stabilized system is totally immiscible, they observed also a compositional gradient at the interface of these crystals, suggesting the possible solid solution formation. In the glasses formed in this system, they reported an absence of phase separation and micro-heterogeneities.

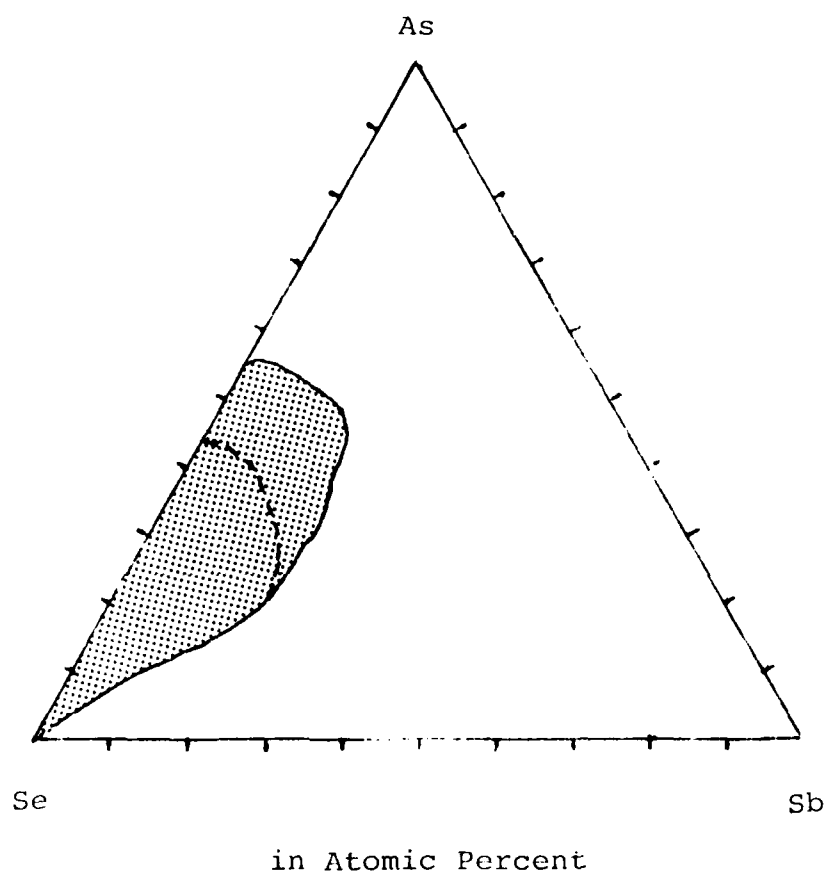


Figure 4. Glass-Forming Region in As-Sb-Se System  
[Ref. 9 ].

### c. Glass Formation

Viscous melts are known to form good glasses because their atoms have low mobility and they can not rearrange themselves toward more stable crystalline configurations during a quench process [Ref.2 and 3]. Homogeneous glasses may be formed over wide ranges of composition by quenching the melts sufficiently fast to avoid phase separation and crystallization. More rapid quenching, which is achievable by physical vapor deposition, has enabled various investigators to fabricate glasses in immiscible systems. However, such glasses may be metastable, and they may approach the lower free energy states through phase separation and subsequent crystallization when they are heated to near their glass transition temperatures, where atoms become mobile [Ref.10 and 20].

The glass-forming tendency of a composition can be examined in two ways. The most straightforward method is a melt quench/X-ray diffraction technique. This method is generally used qualitatively to determine the glass-forming boundaries in the compositional system with a pre-determined melt quenching rate. Detailed information on the glass-forming tendency can be obtained only by examining a large number of different quench rates. Even though it is theoretically possible, a correlation of X-ray diffraction intensity to the degree of crystallinity is not at all straightforward, because many factors affect the diffracted

X-ray intensity.

The second method makes inferences from a dynamic heating differential scanning calorimetry (DSC) measurement, utilizing the empirical Hruby's parameter [Ref.21 and 22]. See Appendix A for the discussion of the DSC technique. Hruby's parameter,  $K_{gl}$ , which quantifies glass-forming ability, is defined as;

$$K_{gl} = \frac{T_c - T_g}{T_l - T_c} \quad (1)$$

where  $T_g$ ,  $T_c$ , and  $T_l$  are the glass transition temperature, crystallization temperature, and liquidus temperature, respectively.

#### d. Crystallization

Crystallization is defined as a phase transformation from a metastable glassy state to a stable crystalline state as described by the free energy diagram in Figure 5 [Ref.23]. Since the free energies of these two states are minima and two minima must be separated by a maxima, an atom or a molecule in the glassy state has to overcome this thermodynamic (or activation energy) barrier in order to reach the crystalline state. The energy necessary to overcome the barrier is supplied by thermal fluctuations. The crystallization process is highly statistical because the energy distribution among atoms or molecules is not uniform, and only those with sufficient energy will

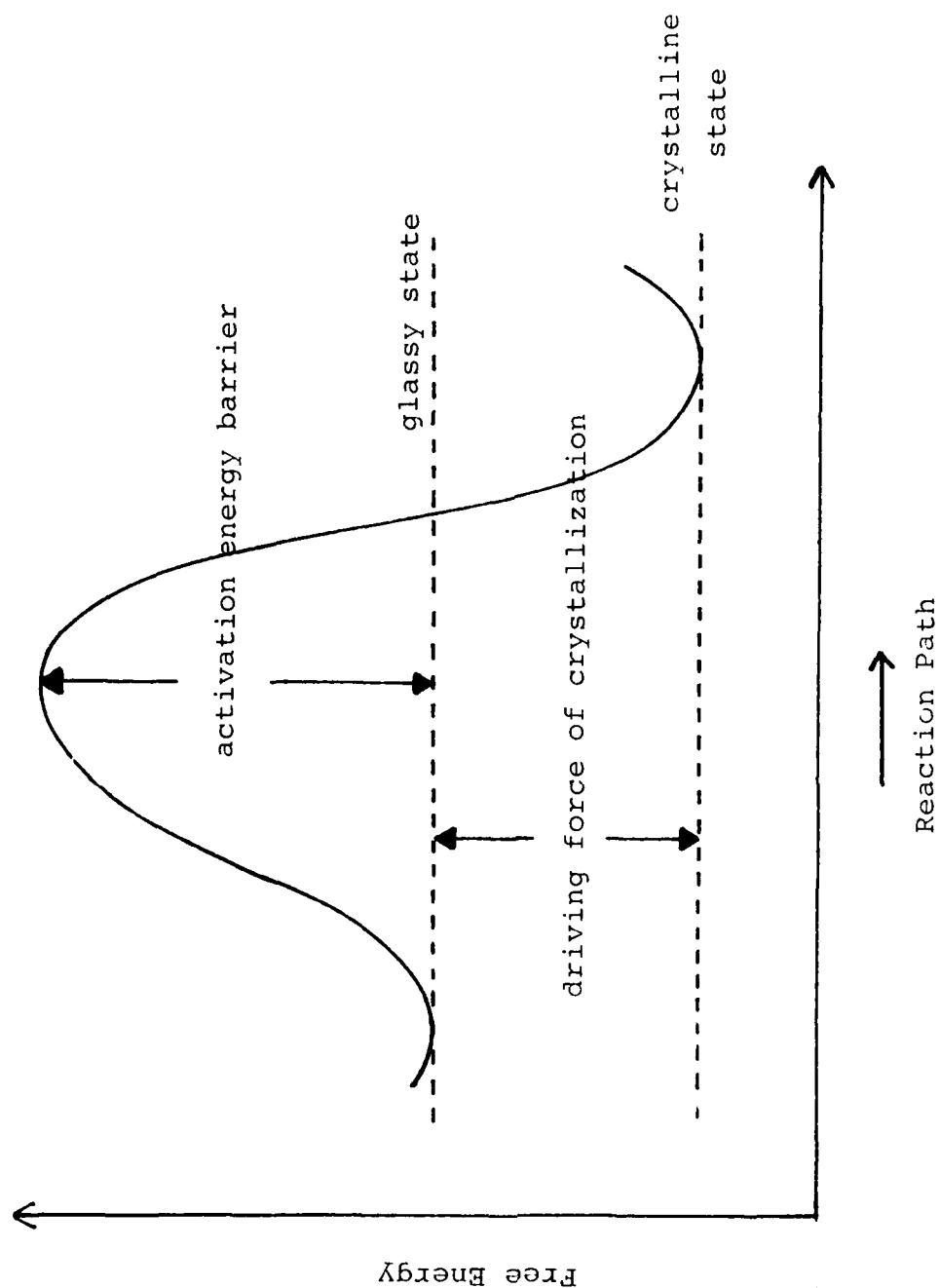


Figure 5. Free Energy Change During Crystallization Process.

transform while those with insufficient energy must wait until they acquire the necessary activation energy. Hence the crystallization process is usually described by fraction crystallized in a given time interval  $t$ ,  $x(t)$  defined as the ratio of the number of crystallized atoms per unit volume at time  $t$  to the number per unit volume available for crystallization at  $t=0$ .

The crystallization process is a heterogeneous reaction which occurs at the phase boundary, and consists of two consecutive events; (1) atomic or molecular diffusion to the phase boundary, and (2) crystallization reaction at the boundary [Ref.23]. Though the crystallization process may be interpreted in terms of various theoretical kinetic models [Ref.23-25], the most applicable and successful empirical equation for a crystallization of inorganic glasses is the Johnson-Mehl-Avrami (JMA) equation [Ref.26-30]. The JMA equation was originally developed with assumptions that; (1) the system is in a quasi-equilibrium state and the rate at which atoms leave the initial state is so small that the energy distribution in the initial state is un-disturbed, (2) the rate is not diffusion limited, and (3) the crystallization mechanism is a nucleation and growth type, (4) nucleation is spatially random, and (5) the process takes place under isothermal conditions. The JMA equation was derived from the formal theory of transformation kinetics, in which the transformed mole

fraction,  $x$ , can be expressed as;

$$x = 1 - \exp \left( -g \int_0^t I_v \left( \int_{t'}^t u d\tau \right)^m dt' \right) \quad (2)$$

where  $g$  is a geometric factor,  $I_v$  the nucleation rate,  $u$  the growth rate,  $m$  is the number of growth dimensions, and  $t$  is time. Assuming that  $I_v$  and  $u$  are temperature dependent and time independent, Equation 2 can be integrated under isothermal conditions to yield a equation in a form;

$$x = 1 - \exp(-Kt^n) \quad \text{--- JMA equation} \quad (3)$$

where  $n$  is a reaction order parameter, which depends on mechanism of reaction, or nucleation rate and growth morphology [Ref.31 and 32]. The rate parameter,  $K$ , is generally assumed to depend only on temperature with Arrhenius temperature dependence defined as;

$$K = K_0 \exp \left( -E_a / RT \right) \quad (4)$$

where  $E_a$  is the activation energy described in Figure 5, the pre-exponential factor  $K_0$  is a frequency of attempts to overcome the energy barrier, which reflects the number of nucleation sites, and  $R$  is the gas constant.

Equation 3 also holds for diffusion limited crystallization processes, in spite of the original constraint for this equation. Since the growth rate  $u$  is proportional to  $\sqrt{t}$  in the diffusion limited processes, Equation 2 can be integrated to yield Equation 3 with a

different  $n$  value. However, it would be difficult to determine if the crystallization process is diffusion limited merely from the  $n$  value, because other factors also affect the  $n$  values.

The magnitude of  $E_a$  may be theoretically interpreted to describe the transformation mechanism only if the transformation involves a single event. In the case of heterogeneous reaction as in crystallization,  $E_a$  is likely to be a superposition of more than one activation energy, and the theoretical interpretation becomes difficult. Therefore,  $E_a$  in crystallization is often called "apparent activation energy" or "macroscopic activation energy", which is an empirical parameter of a practical importance to express the crystallization kinetics.

The crystallization of a glass upon heating may be studied by monitoring various physical and structural properties such as electrical resistivity, hardness, and microstructure [Ref.11,12,14,33-35]. An observation of crystallization using the hot stage X-ray technique is also possible. Since the crystallization is highly exothermic, monitoring the evolved heat by a differential scanning calorimeter is the most popular method of quantifying the crystallization process. Appendix A describes the theory of operation for the thermal analysis.

There are two basically different methods for performing differential thermal analysis; (1) isothermal and

(2) dynamic heating. In the former method, the sample is brought quickly to a specific temperature and the evolved heat during the crystallization process is recorded as a function of holding time. It is necessary to take data at several temperatures to estimate the apparent activation energy. A majority of kinetics studies have been carried out isothermally, since these data are simple to interpret in terms of the JMA equation. However, an isothermal measurement is possible only when the thermal response time of the measuring system is faster than the rate of crystallization. Otherwise, crystallization begins to occur before the system reaches the temperature of interest. In such case, a non-isothermal dynamic heating technique has an advantage.

In the dynamic heating method, the sample is heated through the crystallization temperature range at a constant heating rate, and the evolved heat is recorded as a function of temperature. Because of the dynamic nature of the crystallization process, the temperature at the maximum crystallization rate appears shifted as a function of the heating rate. At higher heating rates, the apparent crystallization appears at higher temperatures. The amount of temperature shift, in turn, can be used to calculate the kinetic parameters of crystallization. However, extending a use of the JMA equation to interpret the dynamic heating data is controversial since the analysis requires time

differentiation of the JMA equation with the implicit assumptions that the process parameters are independent of time [Ref.36-38]. The non-isothermal approach is based on the fact that the slope of the exothermic heat versus temperature trace is zero ( $d^2x/dt^2 = 0$ ) at  $T = T_c$ , where  $T_c$  is the temperature at the maximum crystallization rate. The dynamic heating crystallization equation;

$$\ln \frac{q}{T_c} = \text{const.} - \frac{E_a}{nRT_c} \quad (5)$$

can be obtained by differentiating Equation 3 twice, assuming that  $n$  and  $K$  stay fairly constant with time near  $T=T_c$ , and substituting Equation 4 and  $dT/dt = q =$  heating rate. Some researchers have claimed that their non-isothermal experimental results, fitted to Equation 5, agreed well to the isothermal results [Ref.25 and 30].

Very little is known about the nature of the crystallization process in multi-component chalcogenide glasses. Since  $\text{As}_2\text{S}_3$  has a strong tendency to form a glass and  $\text{Sb}_2\text{S}_3$  has a strong tendency to crystallize, glasses in  $\text{As}_2\text{S}_3$ - $\text{Sb}_2\text{S}_3$  system may present a wide range of crystallization kinetics, which may aid our understanding of the crystallization process in multi-component glasses.

#### e. Glass Transition

A plot of thermodynamic properties such as energy( $E$ ), enthalpy( $H$ ), entropy( $S$ ) and volume( $V$ ) as a function of

temperature is shown in Figure 6. On cooling a liquid, there is a discontinuous change in the thermodynamic properties at the melting point if the liquid crystallizes. However, the properties continue to decrease at the same rate past the melting point if the liquid becomes supercooled and does not crystallize. On further cooling, the rate of change in these properties slows down gradually because the material becomes highly viscous ( $10^{12}$ - $10^{13}$  poise) and the atomic mobility decreases at sufficiently low temperature. Consequently, the material can not relax to its equilibrium state at the cooling rate used. This area is called the glass transition region, and the supercooled liquid becomes a glass and exhibits solid like behavior below this temperature range. If a slower cooling rate is used, the supercooled liquid state persists to a lower temperature because more time is available for the structure to relax. On the other hand, at a faster cooling rate, a thermal arrest of molecular motion or a freezing of the structure appears at a higher temperature, as shown in Figure 7(a) [Ref.4,39-44].

Moynihan et al. [Ref.39] have described that the glass transition begins around the temperature range where the rate of structural relaxation becomes sufficiently slow during cooling that the properties of the supercooled liquid depart from that of the equilibrium liquid, and the transition region ends around the temperature range where

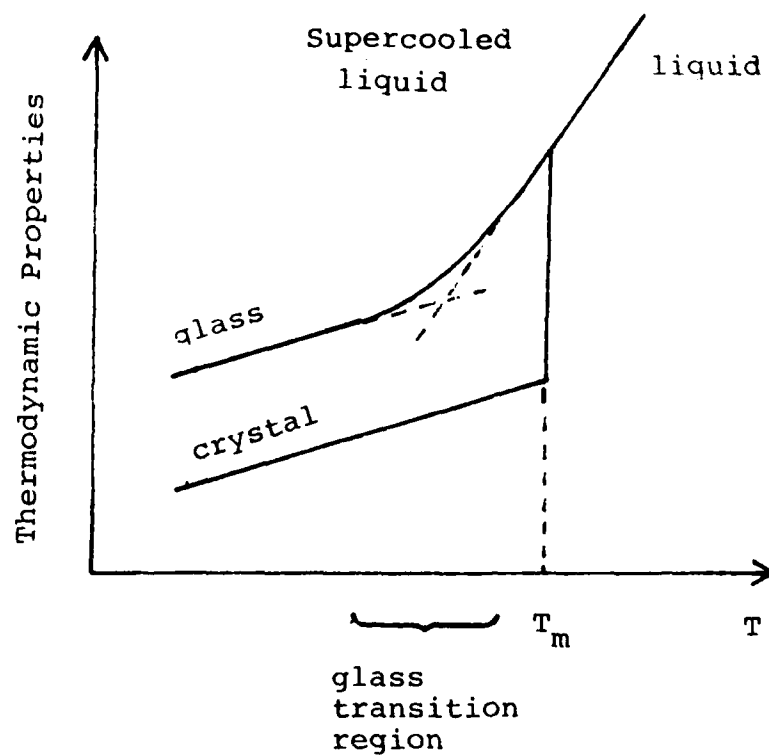


Figure 6. Thermodynamic Properties as a Function of Temperature.

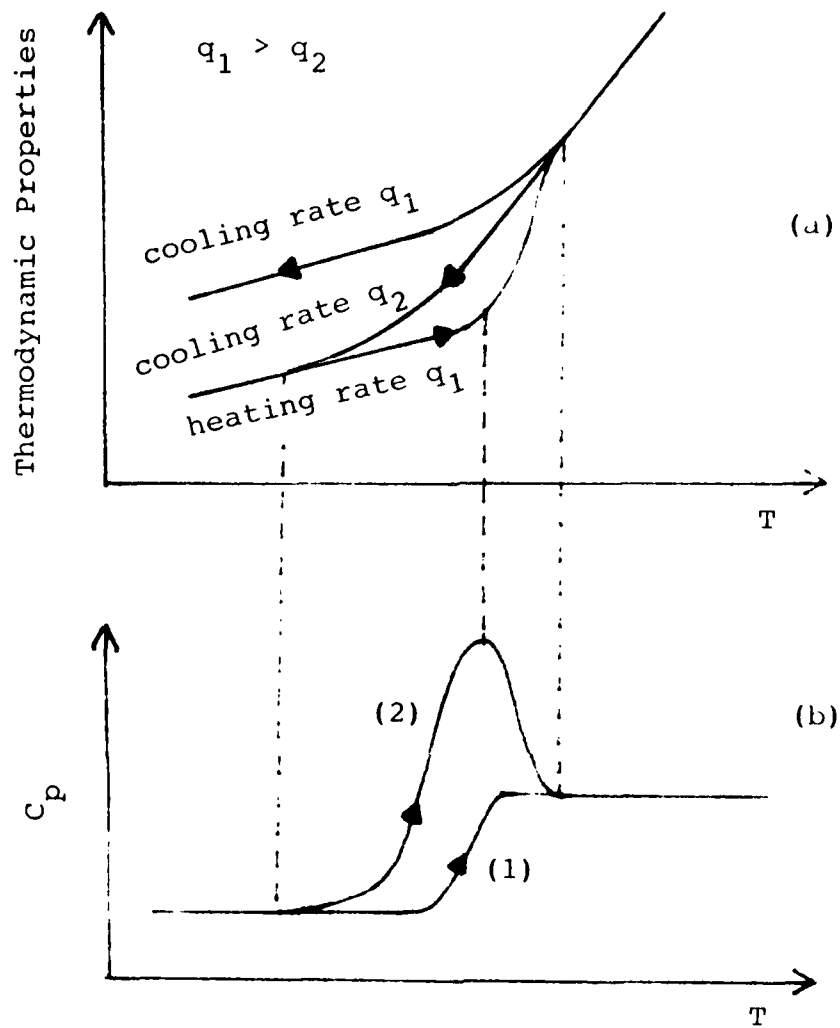


Figure 7. Thermodynamic Properties(a) and Specific Heat(b) of Glasses as a Function of Temperature for Different Cooling Rate [Ref.39].

the structural relaxation becomes so slow that it effectively ceases on the experimental time scale. For practical purposes, however, the glass transition temperature ( $T_g$ ) has been defined as the temperature at the intersection between the curve for the glassy state and that for the supercooled liquid.

Moynihan et al also described the three regions in Figure 7(a) in terms of the relative magnitude between the structural relaxation time ( $\tau$ ) and the instantaneous isothermal holding time at each temperature ( $\Delta t$ ) as; liquid region where  $\Delta t \gg \tau$ , transition region where  $\Delta t \sim \tau$ , and glass region where  $\Delta t \ll \tau$ . In this argument, the transition region has to shift, depending on the cooling or heating rate, in order to satisfy the condition for the appearance of the transition region,  $\Delta t \sim \tau$ . The dependence of  $T_g$  on heating or cooling rate ( $q$ ) may be described by an equation [Ref.39,41-43].

$$\frac{d \ln q}{d(1/T_g)} = - \frac{H_a}{R} \quad (6)$$

where  $H_a$  is the activation enthalpy for structural relaxation. Thus, the dependence of  $T_g$  on heating and cooling rate reveals information about the structural relaxation parameter of the material.

A continuous change in enthalpy in the glass transition region as described so far produces a discontinuous step

change in specific heat as shown in Figure 7(b) curve (1). However, under a certain heating, cooling, or annealing condition of the sample, an endothermic peak along with the step change may appear in the upscan curve as shown in Figure 7(b) curve (2). This peak appears when the prior sample cooling rate  $q_2$  is slower than the heating rate  $q_1$ , or the sample was annealed at a temperature below  $T_g$ . In either case, the material is more stabilized or at a lower free energy state below  $T_g$  and catches up to the higher energy state in a short period of time by absorbing heat from environment. Therefore, the amount of energy absorbed back in the glass transition region, that is the magnitude of the integrated area under the peak in Figure 7(b) curve (1), reflects the enthalpy of the relaxation processes which occur during an isothermal annealing [Ref.19,45, and 46].

The temperature at which the glass transition takes place strongly reflects the atomic bonding strength of the glass network.  $T_g$  is higher for glasses with more rigid structure and stronger bonding.

The rate of change or the temperature derivative of the thermodynamic properties, such as specific heat ( $C_p = \partial H / \partial T$ ) or thermal expansion coefficient ( $\alpha = \partial V / \partial T$ ) for example, are very similar in the glassy state as in the crystalline state.

## II. EXPERIMENT AND DATA ANALYSIS PROCEDURE

### 1. SPECIMEN PREPARATION

#### a. Bulk Specimens

Bulk specimens of  $\text{As}_{2-x}\text{Sb}_x\text{S}_3$  with nominal compositions ranging from  $x = 0.0$  to  $2.0$  were synthesized. All nominal compositions were located on the compositional tie line between  $\text{As}_2\text{S}_3$  and  $\text{Sb}_2\text{S}_3$ . The starting materials were arsenic trisulfide (Servofrax<sup>®</sup> glass), elemental antimony supplied by Cerac (shot, 99.999 percent purity), and elemental sulfur supplied by Cominco America Inc. (lump, 99.95 percent purity). 10 gram batches of the starting mixture were sealed in fused silica ampules under vacuum of around  $10^{-6}$  torr, in order to avoid an excessive internal pressure build-up and oxygen contamination during the melting process. The ampules were wrapped in a wet rag while being sealed, so that the content of the ampules did not evaporate with heat from the hydrogen-oxygen torch. The reaction and homogenization were performed in a rocking furnace, with a moderate rocking speed of  $\sim 17$  RPM and the maximum tilting angle of  $\pm 30^\circ$  from the horizontal position. The mixtures were first heated to  $570^\circ\text{K}$  and held at the temperature for 24 hours to react volatile elemental sulfur in order to reduce internal pressure, before heating to the final reaction temperature of  $940^\circ\text{K}$ . The melts were reacted and homogenized at  $940^\circ\text{K}$  for 48 hours, and they were

as fluid as mercury at this temperature.

For each composition, a quenched specimen and a slow cooled specimen were prepared. A cooling rate of around  $500^{\circ}\text{K}$  per minute was achieved by dropping the sealed melts into liquid nitrogen. Slow cooled specimens were prepared by cooling the melts from  $940^{\circ}\text{K}$  to  $570^{\circ}\text{K}$  at the cooling rate of  $0.1^{\circ}\text{K}$  per minute and holding at  $570^{\circ}\text{K}$  for 140 hours. The slow cooling ampules were placed in copper tubes to compensate for the temperature gradient of the furnace, which tends to cause a compositional segregation.

#### b. Film Specimens

Vapor deposited film specimens were produced by co-evaporation of bulk  $\text{As}_2\text{S}_3$  and  $\text{Sb}_2\text{S}_3$  in a vacuum of  $10^{-6}$  torr. The materials were evaporated from two separate boats, which were resistance heated independently through two sets of high current power supplies and temperature controllers. The boat temperatures were measured with a chromel/alumel thermocouples spot-welded to the boats. Large capacity box type tungsten boats were used. Deposition rate was monitored with a quartz crystal monitor (Veeco Instruments Model QM-300/RI-100). The films were deposited on aluminum foil substrates (5 cm by 5 cm) placed 30 cm above the center of the two boats assembly, which was determined to be the optimum substrate location for a proper vapor mixing according to the previous deposition rate calibrations.

Moderate deposition rates (40 -50 Å/sec total) were used, since this study showed significant deviations in film stoichiometry and properties when higher deposition rates were used (see Appendix B). Since it took about one hour to deposit fairly thick films ( $\sim 15 \mu\text{m}$  thick) at the deposition rate used, it was essential that the deposition rates of both materials stayed reasonably constant at least during that time. The deposition rate was found to vary during a deposition run, even when the measured boat temperature remained constant, mainly because of changes in surface area of the evaporating material, and because of a temperature gradient of the boat. The following precautions helped minimize the variation in deposition rates; (1) using a deep, large capacity box type boat to minimize change in evaporating surface area and to eliminate the necessity of re-charging the boat, (2) melting of the material in the boat to create a flat evaporating surface prior to deposition run, and (3) using a boat without hot spots. The deposition rate calibrations were performed at the beginning of each run. With these precautions, the deposition rate fluctuation for individual material was reduced to less than 10 percent, which led to an overall compositional accuracy and homogeneity that was within  $\pm 5$  percent. The increased compositional accuracy could have been achieved if two separate rate monitors had been used to control the deposition rate of each boat.

## 2. THERMAL ANALYSIS

A Perkin-Elmer Differential Scanning Calorimeter (DSC-2) was used both in the dynamic heating and isothermal experiments. The temperature scale and sensitivity of the instrument were calibrated routinely, using the melting point and enthalpy of fusion of Indium, Tin, and Lead, at 5°K/min heating rate. The temperature scales at other heating rates were corrected by using calibration curves, instead of calibrating the instrument itself at each heating rate. All measurements were referenced to an empty aluminum pan. All samples were hermetically sealed in aluminum pans, because of the volatile nature of sulfide samples at higher temperatures, and because sulfur contamination is detrimental to the platinum components of the calorimeter. The sulfide samples were found to react with both gold and platinum pans near their fusion temperatures. The use of aluminum pans limited the high temperature capability to below 800°K. In addition, as an extra precaution, all experiments were conducted with dry nitrogen gas flowing through a ventilated cell cover to vent out any escaping sulfur in case of a pan leak. The samples were sealed under a flowing nitrogen atmosphere to avoid oxidation of the samples during experiments. The sample weight was typically around 15mg. The sensitivity of the instrument was set at 1 mcal/sec.

#### a. Dynamic Heating Experiments

The dynamic heating data were taken at four different heating rates ( $5^{\circ}\text{K}/\text{min}$ ,  $10^{\circ}\text{K}/\text{min}$ ,  $20^{\circ}\text{K}/\text{min}$ , and  $40^{\circ}\text{K}/\text{min}$ ) for each composition to investigate the glass transition, crystallization, and liquidus temperatures. The base line, taken at each heating rate and stored in a Data Station (Perkin-Elmer), was subtracted from data automatically to maximize the sensitivity and accuracy of the instrument.

It was noted that the difference in sample weight produced a marked difference in the measured characteristic temperatures. The melting temperature of Lead, measured at four different heating rates is shown in Figure 8. The melting peak became broader at faster heating rate, and this effect was more pronounced for heavier samples. As a consequence, if the middle or end point of a reaction is to be accurately determined, account must be taken of the fact that the measured temperature fluctuates depending on the sample weight, whereas the reaction onset temperature is least affected by the difference in sample weight. Therefore, it is preferable to define a reaction temperature by the onset of reaction whenever possible, or if not, by using a small sample and a slow heating rate to minimize this thermal lag caused by the finite sample size and finite heating rate. In this study, the liquidus temperatures (that is the end point of melting) were measured at  $5^{\circ}\text{K}/\text{min}$  heating rate, using small samples weighing less than 10 mg.

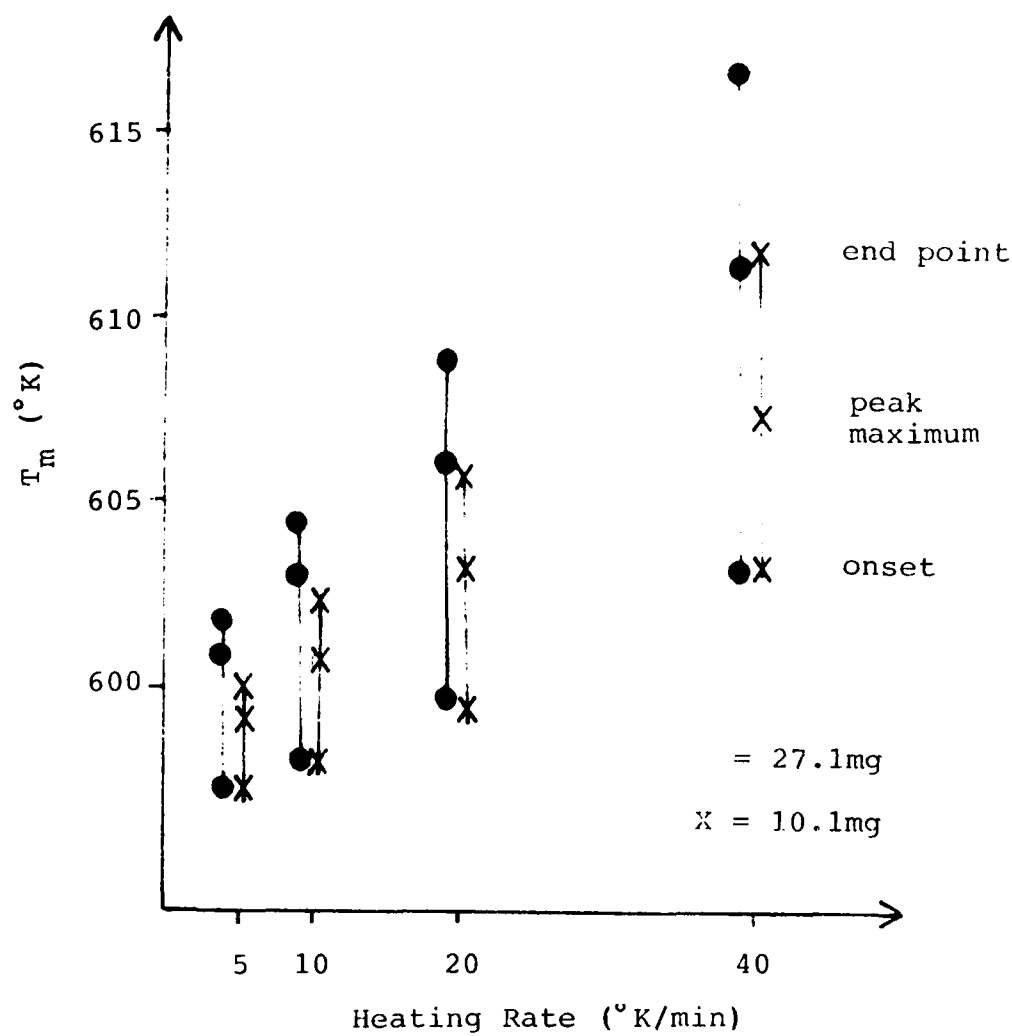


Figure 8. Effect of DSC Sample Weight on Measured Melting Temperature of Lead.

The glass transition temperatures were measured at the transition onset, which was defined as the intercept of two lines; the extrapolated base line below  $T_g$ , and the line drawn tangent to the curve at the maximum slope. The crystallization temperatures were measured at the temperature of the maximum crystallization rate according to the definition of Equation 5, using samples which weighed approximately the same in all experiment for better reproducibility.

It is a common practice to thermally cycle a sample in the DSC instrument during a dynamic heating experiment in order to minimize errors caused by the variations in sample weight. This procedure did not present any problems in the study of the glass transition temperature because it is a reversible process. However, this procedure was not acceptable for the dynamic heating crystallization study, because crystallization was found to appear at different temperatures for each thermal cycling, even when the heating and cooling rates were ensured to be identical (the sample was heated to above its melting point and quenched by taking it out of the DSC cell to simulate the original liquid nitrogen quench condition). The crystallizations on second and subsequent heatings occurred at much higher temperatures compared to that in the initial heating. For this reason, all crystallization data were taken on the initial heatings.

Four dynamic heating runs were conducted under an identical condition and the average values of  $T_g$ ,  $T_c$  and  $T_l$  were reported. These data were also used in the calculations of activation energies and Hruby's parameters. The activation energies of glass transition were calculated using Equation 6 and those of dynamic heating crystallization were calculated by Equation 5. The Hruby's parameters were calculated using Equation 1.

#### b. Isothermal Experiments

Constant temperature experiments were conducted in order to study the isothermal crystallization. A sample was introduced into the DSC cell at 420°K, and heated to the temperature of interest at a heating rate of 320°K/min. An X-Y recorder, used in a time scanning mode, was started as soon as the DSC cell reached the isothermal temperature. Since the first 20 seconds of data were lost while the instrument was being stabilized, a correction was made by simply connecting the origin and the point at  $t=20$ , assuming that no crystallization has taken place before  $t=0$ . In order to determine the partial area crystallized in Equation 3, the trace was marked at  $t = t_1, t_2, \dots, t_6$  as shown in Figure 9, cut out at each  $t$  value and weighed with a microbalance, and compared to the total weight of the trace. This method worked better than the computer integration method in this particular case, because the lost area at the beginning of the trace could be accounted for.

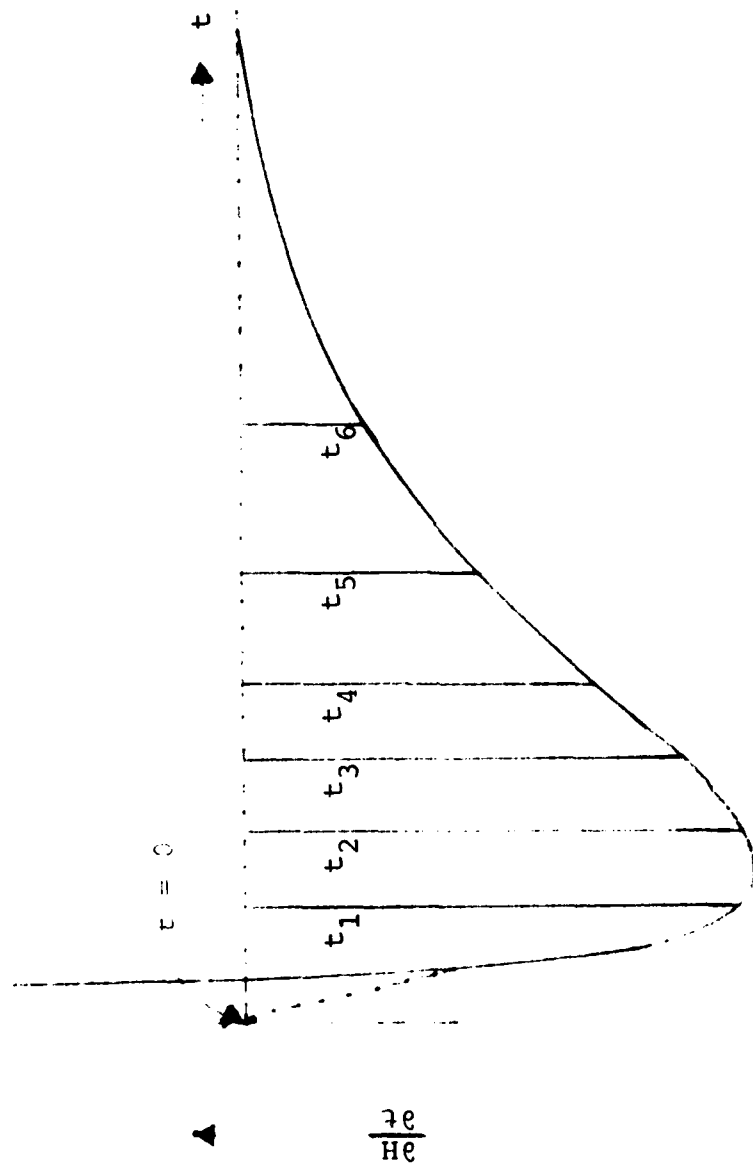


Figure 9. An Example of Isothermal Crystallization Data.

After determining the partial area crystallized,  $x$ , as a function of time, these data were plotted as  $\ln \ln(1/(1-x))$  versus  $\ln t$  (another form of Equation 3) to check the validity of the equation. This relationship and all the assumptions were assumed to be valid if the data points lay on a straight line. The slope of this line is  $n$ , and the intercept is  $\ln K$ . The isothermal data were taken at four different temperatures ( $T_{iso}$ ) and the apparent activation energy of crystallization was determined from the slope of  $\ln K$  vs.  $1/T_{iso}$  plot. Four identical measurements were conducted at each temperature for each specimen to establish the limits of error.

It was found that crystallization occurred before reaching the isothermal temperature if the temperature was too high, yielding poor fit of data and higher  $n$  values. Therefore,  $T_{iso}$ 's were chosen at levels below such temperatures.

The sample weight and surface area were found to strongly affect the kinetic parameters obtained with the isothermal technique. The effect of sample weight on isothermal crystallization is shown in Figure 10, which indicates that the smaller samples crystallized quicker. This did not affect the slope of the line ( $n$  value), but it had a great effect on the intersection of the line at  $\ln t = 0$  ( $K$  value). The effect of sample's surface area on crystallization is shown in Figure 11. Different surface

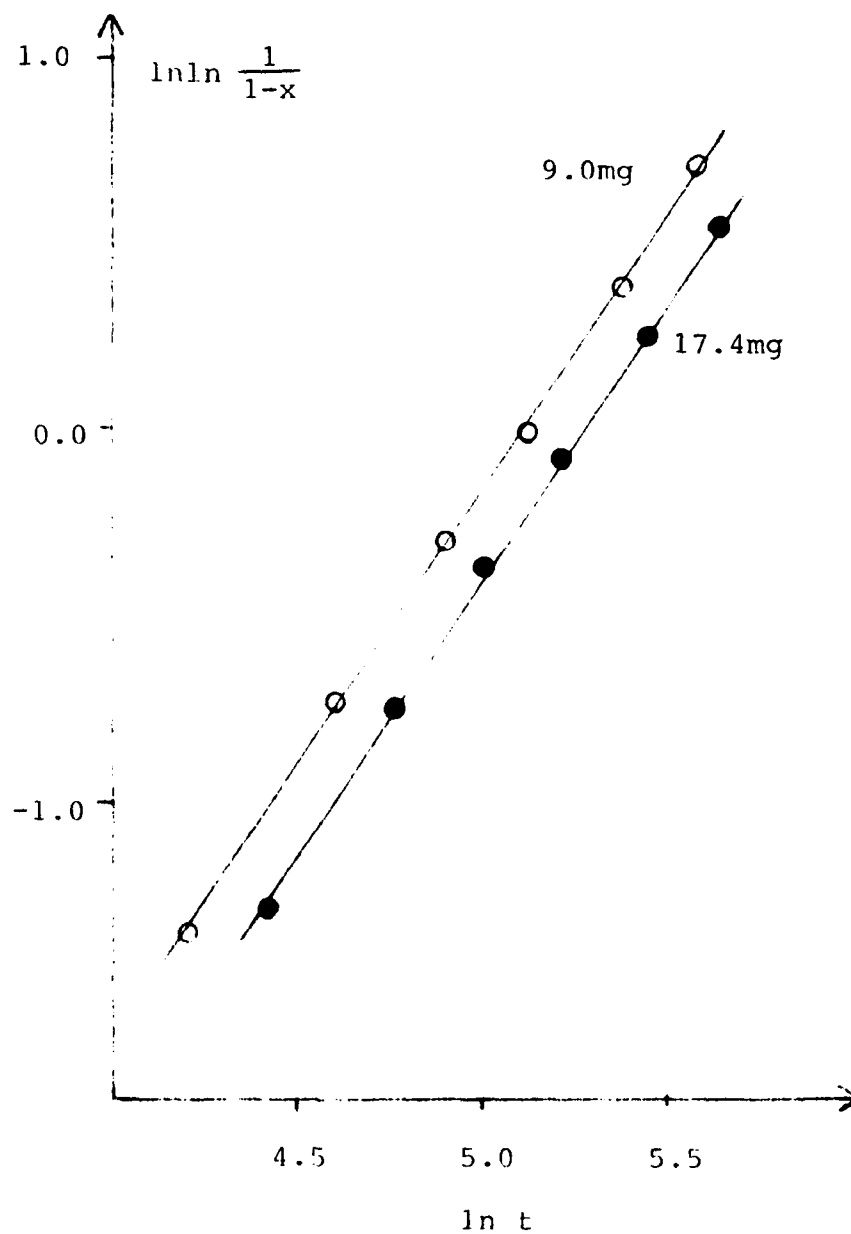


Figure 10. Effect of Sample Weight on Isothermal Crystallization.

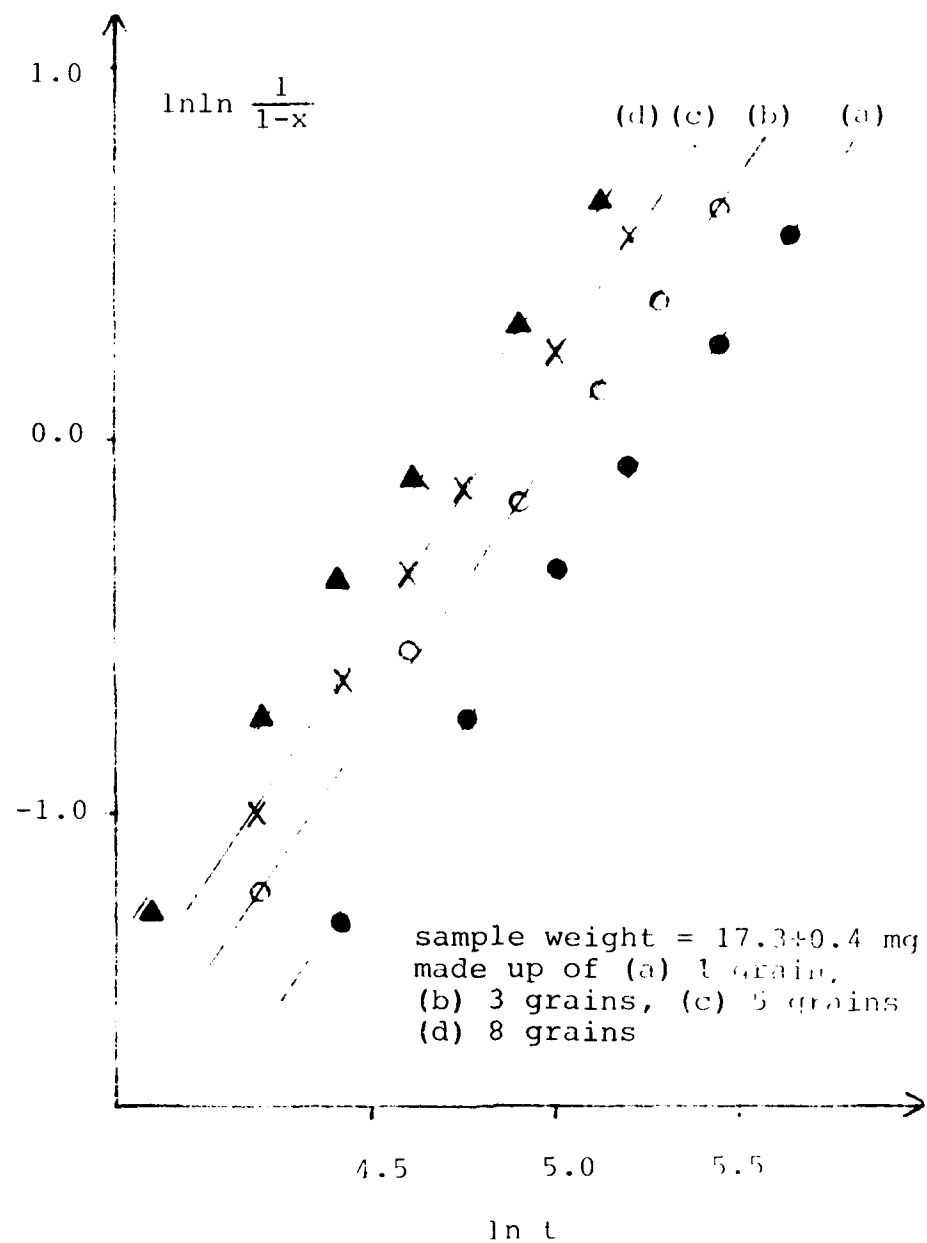


Figure 11. Effect of Sample's Surface Area on Isothermal Crystallization.

areas were created by dividing the samples (weighing approximately the same) into different number of pieces of about the same size. This experiment showed that the samples having larger surface area crystallized quicker, and again the K value was greatly affected. Because of these two findings, extra attention was paid in preparing samples for the isothermal crystallization experiment, to ensure that all samples weighed about the same, and to keep the sample in one piece during the sample sealing operation.

#### c. Error Analysis of Activation Energy Calculations

The errors associated with the activation energy calculations were estimated using a Student's t analysis [Ref.47], since the data could be fitted linearly to the activation energy equations, i.e.,  $\ln K$  vs.  $1/T_{iso}$  for isothermal crystallization,  $\ln (q/T_c)$  vs.  $1/T_c$  for dynamic heating crystallization, and  $\ln q$  vs.  $1/T_g$  for glass transition temperature. The slopes of these lines correspond to the activation energies.

The error for the slope,  $b$ , of a straight line, obtained from the data set  $(X_i, Y_i)$  using a linear regression analysis can be written as;

$$\Delta b = t_{\alpha/2} \text{Se} \sqrt{\frac{N}{S_{xx}}} \quad (7)$$

where

$$S_e^2 = \frac{S_{xx} S_{yy} - (S_{xy})^2}{N(N-2) S_{xx}} \quad (8)$$

$$S_{xx} = N \sum_{i=1}^N X_i^2 - \left( \sum_{i=1}^N X_i \right)^2$$

$$S_{yy} = N \sum_{i=1}^N Y_i^2 - \left( \sum_{i=1}^N Y_i \right)^2$$

$$S_{xy} = N \sum_{i=1}^N X_i Y_i - \left( \sum_{i=1}^N X_i \right) \left( \sum_{i=1}^N Y_i \right)$$

N = number of data points

t = t statistics at confidence level 1- $\alpha$   
and degrees of freedom N-2

It is more convenient to express  $\Delta b$  in terms of the correlation coefficient,  $r$ , which can be calculated using;

$$r = \frac{S_{xy}}{\sqrt{S_{xx} S_{yy}}} \quad (9)$$

Substituting Equation 9 and  $b = S_{xy}/S_{xx}$  into Equation 8, Equation 7 become;

$$\frac{\Delta b}{b} = t_{\alpha/2} \sqrt{\frac{1-r^2}{(N-2) r^2}} \quad (10)$$

The percent errors in activation energies can be easily calculated using Equation 10. In the current analysis, a confidence level of 90 percent was chosen, and the number of degrees of freedom equal to 14 was used because 16 data points were used in each activation energy calculation ( 4 identical runs at each temperature or heating rate, and 4 different temperatures or heating rates).

### 3. OTHER CHARACTERIZATIONS

The sulfur contents of bulk specimens was analyzed using the Schoninger sulfur combustion technique. At least four measurements were taken for each composition to check the homogeneity within the batch.

X-ray analyses were conducted with a Phillip X-ray diffractometer, using a Cu K<sub>α1</sub> monochromator. The angle scanning speed of the goniometer was 1 degree per minute, and the diffracted X-ray intensity was plotted as a function of angle (2θ). The diffraction peak angles were manually read from the chart, and converted to lattice spacing (d), using a conversion equation for Cu K<sub>α1</sub> line (λ = 1.54050Å);

$$d = \lambda / 2 \sin \theta \quad (11)$$

Since most of the bulk specimens were in odd shapes, they were powdered and dusted onto a microscope slide with a thin film of vacuum grease to obtain a fairly smooth and flat sample surface required for good focus of the instrument. The vacuum grease did not affect the X-ray peaks of the specimens. The reproducibility of the measurements were better than  $\pm 0.01^\circ$ . Two major sources of the experimental error were; (1) minor deviation of the specimen plane from the instrument's 2θ = 0 plane, and (2) uncertainty in reading the peak angles from the chart.

Scanning Electron Microscopy (SEM) was performed to study the microstructure and the crystal growth morphology

of bulk specimens. Since these sulfide specimens were found to crack and deform when regular metallographic sample mounting techniques were used, they were cold mounted in epoxy. A small part of each mounted and polished sample was etched with NaOH solution, diluted to 0.1N with distilled water, to reveal the microstructure caused by the differential etching of phases.

### III. RESULTS AND DISCUSSION

#### 1. CHEMICAL COMPOSITIONS

All of the bulk specimens were visually homogeneous, indicating complete reaction and mixing. Sulfur stoichiometry, as determined by the Schoninger sulfur combustion method, are listed in TABLE 1. The reproducibility of measurements was better than  $\pm 0.5$  percent of the total sample weight. Four of the bulk specimens were found to be grossly sulfur deficient. Sulfur probably evaporated during the ampule sealing process in these batches, in spite of the extra precaution taken to keep the ampules cool. Sulfur content of other bulk compositions were found to be within two percent of the nominal stoichiometry. Powdered specimens derived from stoichiometric bulk compositions consistently showed lower sulfur content, probably because of the absorbed water on powder surface. Films also showed lower sulfur stoichiometry apparently for the same reason, and the chemical analyses for these specimens are not listed because they may not be accurate. Several attempts have been made to determine the antimony content, utilizing atomic absorption spectroscopy. However, the accuracy of these measurements were found to be too low ( $\pm 5$  percent of total sample weight) for a useful compositional characterization. Other analyses conducted on the

TABLE 1. LIST OF SAMPLE COMPOSITIONS AND ANALYSIS CONDUCTED ON SAMPLES

Bulk Samples - Liquid Nitrogen Quenched				
Nominal Compositions	Analyzed Sulfur Stoich.	Analysis conducted		
		X-Ray	SEM	DSC
As <sub>2</sub> S <sub>3</sub>	2.99 ± 0.02	X	X	X
As <sub>1.8</sub> Sb <sub>0.2</sub> S <sub>3</sub>	2.98 ± 0.04	X		X
As <sub>1.6</sub> Sb <sub>0.4</sub> S <sub>3</sub>	2.98 ± 0.03	X	X	X
As <sub>1.4</sub> Sb <sub>0.6</sub> S <sub>3</sub>	2.97 ± 0.02	X		X
As <sub>1.2</sub> Sb <sub>0.8</sub> S <sub>3</sub>	2.98 ± 0.03	X	X	X
	2.55 ± 0.03	X	X	X
As <sub>1.0</sub> Sb <sub>1.0</sub> S <sub>3</sub>	2.94 ± 0.02			X
	2.67 ± 0.03	X	X	X
As <sub>0.8</sub> Sb <sub>1.2</sub> S <sub>3</sub>	3.02 ± 0.04	X	X	X
As <sub>0.6</sub> Sb <sub>1.4</sub> S <sub>3</sub>	2.98 ± 0.02	X	X	X
As <sub>0.4</sub> Sb <sub>1.6</sub> S <sub>3</sub>	3.00 ± 0.04	X	X	X
As <sub>0.2</sub> Sb <sub>1.8</sub> S <sub>3</sub>	3.01 ± 0.03	X	X	X
Bulk Samples - Slow Cooled				
As <sub>1.6</sub> Sb <sub>0.4</sub> S <sub>3</sub>	2.90 ± 0.02	X	X	X
As <sub>1.4</sub> Sb <sub>0.6</sub> S <sub>3</sub>	2.95 ± 0.03	X	X	X
As <sub>1.2</sub> Sb <sub>0.8</sub> S <sub>3</sub>	2.58 ± 0.03	X	X	X
As <sub>1.0</sub> Sb <sub>1.0</sub> S <sub>3</sub>	2.94 ± 0.02	X		
	2.66 ± 0.04	X	X	X
As <sub>0.9</sub> Sb <sub>1.1</sub> S <sub>3</sub>	3.03 ± 0.03	X	X	X
As <sub>0.8</sub> Sb <sub>1.2</sub> S <sub>3</sub>	2.95 ± 0.02	X	X	X
As <sub>0.6</sub> Sb <sub>1.4</sub> S <sub>3</sub>	2.98 ± 0.04	X	X	X
As <sub>0.4</sub> Sb <sub>1.6</sub> S <sub>3</sub>	2.96 ± 0.04	X	X	X
As <sub>0.2</sub> Sb <sub>1.8</sub> S <sub>3</sub>	2.92 ± 0.04	X	X	
Sb <sub>2</sub> S <sub>3</sub>	3.01 ± 0.04	X	X	
Film Samples - Vapor Deposited				
As <sub>0.8</sub> Sb <sub>1.2</sub> S <sub>3</sub>		X		X
As <sub>0.4</sub> Sb <sub>1.6</sub> S <sub>3</sub>		X		X
Sb <sub>2</sub> S <sub>3</sub>		X		X

specimens are also listed on TABLE 1.

## 2. X-RAY ANALYSIS

X-ray analysis was conducted to examine the extent of the glass formation and the phases present in crystallized state.

The results of X-ray diffraction analysis are summarized on TABLE 2. Among the specimens with stoichiometric amounts of sulfur,  $\text{As}_{2-x}\text{Sb}_x\text{S}_3$ , the slow cooled specimens were amorphous in the arsenic rich region from  $x=0$  to  $x=1.1$ , while the liquid nitrogen quenched ones were amorphous up to  $x=1.4$ . All vapor deposited films were amorphous, presumably due to the rapid quench rate of the deposition process. The glass forming region as a function of sample cooling conditions is shown in Figure 12. All X-ray peaks for stoichiometric, crystalline samples corresponded closely to those of  $\text{Sb}_2\text{S}_3$ , indicating that only  $\text{Sb}_2\text{S}_3$  contributed to the crystallization of  $\text{As}_{2-x}\text{Sb}_x\text{S}_3$ . The lattice spacings were the same for all compositions within experimental error ( $\pm 0.01\text{\AA}$ ), suggesting an absence of solid solution formation in this system, as in the case of  $\text{As}_{2-x}\text{Sb}_x\text{Se}_3$  system reported in the literature [Ref.8]. This result was expected because two end compositions,  $\text{As}_2\text{S}_3$  and  $\text{Sb}_2\text{S}_3$ , crystallize in different crystal structures.

The slow cooled specimens with sulfur deficiency were crystalline at  $x=0.8$  and  $x=1.0$ , while the stoichiometric specimens were glassy at these compositions, and exhibited

TABLE 2. MEASURED LATTICE SPACING VALUES  
FROM X-RAY ANALYSIS

Hand Book Values for $Sb_2S_3$ [Ref.19]			Measured Lattice Spacings Å		
[hkl]	Relative Peak Int.	Lattice Spacing Å	Slow Cooled $As_{2-x}Sb_xS_3$		
			x=0-1.1	x=1.2	x=1.4
[110]	16	7.990	a m o r p h o u s	8.00	8.00
[020]	36	5.654		5.66	5.66
[120]	57	5.052		5.06	5.05
[220]	28	3.987		3.99	3.99
[101]	29	3.632		-	3.62
[130]	67	3.573		3.57	3.57
[310]	72	3.556		-	-
[111]	25	3.458		-	3.44
[021]	18	3.178		-	3.17
[230]	37	3.128		3.13	3.13
[211]	95	3.053		3.05	3.05
[221]	100	2.764		2.76	2.76
[301]	52	2.680		2.68	2.68
[311]	25	2.609		2.61	2.61
[240]	46	2.525		2.53	2.53
[231]	22	2.426		2.42	2.42
[041]	24	2.277		2.27	2.27
[430]	14	2.252		2.26	2.25
[141]	25	2.233		2.22	2.23
[421]	21	2.101		2.10	2.10
[520]	12	2.088		-	-
[440]	10	1.992		-	1.99
[431]	46	1.946		1.94	1.94
[002/151]	36	1.920		-	1.91
[351]	19	1.729		-	-
[531]	20	1.725		1.72	1.72
[132]	34	1.691		1.68	1.69

TABLE 2. (cont)

Measured Lattice Spacings    Å					
Slow Cooled $\text{As}_{2-x}\text{Sb}_x\text{S}_3$			Quenched $\text{As}_{2-x}\text{Sb}_x\text{S}_3$		
x=1.6	x=1.8	x=2.0	x=0-1.4	x=1.6	x=1.8
8.00	8.00	8.00	a m o r p h o u s e	-	8.00
5.67	5.66	5.66		5.64	5.66
5.06	5.05	5.05		5.05	5.06
3.99	3.98	3.99		3.98	3.99
3.63	3.63	3.63		-	3.63
3.57	3.57	3.57		3.57	3.57
-	-	-		-	-
3.46	3.46	3.46		-	3.45
3.17	3.17	3.18		-	3.17
3.13	3.13	3.13		3.12	3.13
3.05	3.05	3.06		3.04	3.05
2.76	2.76	2.76		2.76	2.76
2.68	2.68	2.68		2.68	2.68
2.61	2.61	2.61		-	2.61
2.53	2.52	2.52		2.52	2.52
2.42	2.42	2.42		-	2.42
2.27	2.27	2.27		-	2.27
2.25	2.25	2.25		-	2.25
2.23	2.23	2.23		-	2.23
2.10	2.10	2.10		-	2.10
-	-	-		-	-
1.99	1.99	1.99		-	1.99
1.94	1.94	1.94		1.94	1.94
1.91	1.92	1.92		-	1.92
1.73	1.73	1.73		-	1.73
-	-	-		-	-
1.69	1.69	1.69		-	1.69

TABLE 2. (cont)

Lattice Spacings Å	
Slow Cooled Sulfur Deficient Samples	
As <sub>1.2</sub> Sb <sub>0.8</sub> S <sub>2.55</sub>	As <sub>1.0</sub> Sb <sub>1.0</sub> S <sub>2.67</sub>
8.00	8.00
6.80	-
5.77	5.79
5.64	5.66
5.03	5.06
4.86	-
4.12	-
3.97	3.99
3.56	3.58
3.44	3.45
3.12	3.13
3.04	3.05
2.99	-
2.93	2.90
2.87	-
2.75	2.76
2.67	2.68
2.60	2.60
2.52	2.53
2.41	2.42
2.27	2.27
2.25	2.25
2.22	2.23
2.10	2.10
1.99	1.99
1.94	1.94
1.91	1.91

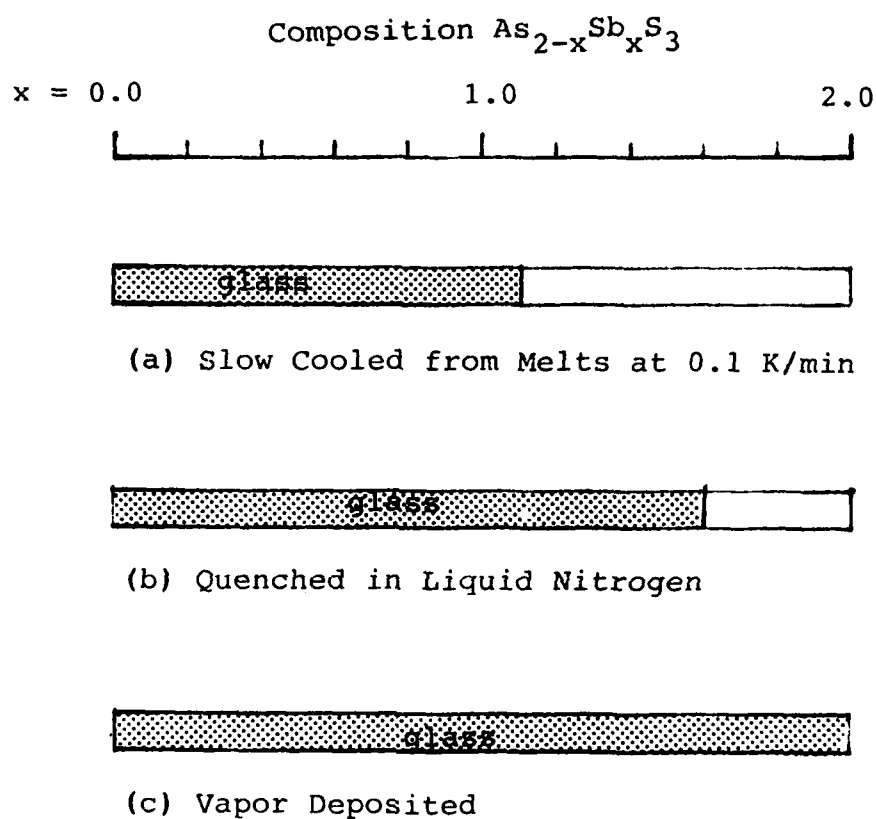


Figure 12. Glass-Forming Region in  $\text{As}_{2-x}\text{Sb}_x\text{S}_3$  for Different Cooling Rate.

extra X-ray peaks superimposed on the  $\text{Sb}_2\text{S}_3$  peaks. These extra peaks correlate to  $\text{AsS}-\beta$  crystals.

### 3. SCANNING ELECTRON MICROSCOPY

Figures 13a through 15f show the microstructures of bulk specimens. Among those, the Figures 13a through 13i are of the stoichiometric slow cooled specimens, Figures 14a through 14e are of the stoichiometric quenched specimens, and Figures 15a through 15f are of the sulfur deficient specimens.

Antimony rich specimens, when slow cooled, exhibited two phase structures with a highly directional acicular crystal phase (lighter color phase) and a matrix phase (darker phase) as seen in Figures 13c, 13d, and 13f. The matrix, which was observed to etch away as seen in Figures 13e and 13g, is believed to be glassy  $\text{As}_2\text{S}_3$ . The acicular crystals were found to be  $\text{Sb}_2\text{S}_3$  by X-ray diffraction analysis, and the diameter of the needle crystal was observed to decrease as more antimony was replaced with arsenic. The diameter was larger than 20  $\mu\text{m}$  for  $\text{Sb}_2\text{S}_3$  (Figure 13a) and  $\text{As}_{0.2}\text{Sb}_{1.8}\text{S}_3$  (Figure 13b), and around 10  $\mu\text{m}$  for  $\text{As}_{0.4}\text{Sb}_{1.6}\text{S}_3$  (Figure 13c). The diameter decreased to 1-5  $\mu\text{m}$  for  $\text{As}_{0.6}\text{Sb}_{1.4}\text{S}_3$  (Figures 13d and 13e) and to 0.5  $\mu\text{m}$  for  $\text{As}_{0.8}\text{Sb}_{1.2}\text{S}_3$  (Figures 13f and 13g). This clearly shows that the glassy  $\text{As}_2\text{S}_3$  phase interferes with the growth of a  $\text{Sb}_2\text{S}_3$  crystal. At the composition  $\text{As}_{0.8}\text{Sb}_{1.2}\text{S}_3$ , the  $\text{Sb}_2\text{S}_3$  crystals could no longer grow in a preferred direction



Figure 13a. Microstructure of Slow Cooled Sb<sub>2</sub>S<sub>3</sub>  
(Unetched).



Figure 13b. Microstructure of Slow Cooled  $\text{As}_{0.2}\text{Sb}_{1.8}\text{S}_3$  (Unetched).



Figure 13c. Microstructure of Slow Cooled  $\text{As}_{0.4}\text{Sb}_{1.6}\text{S}_3$   
(Unetched).

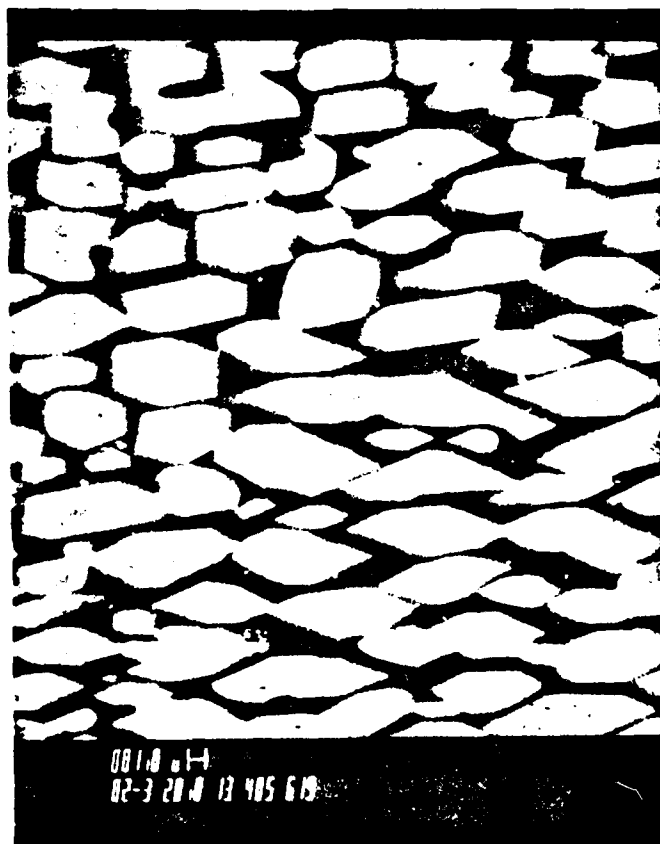


Figure 13d. Microstructure of Slow Cooled  $\text{As}_{0.6}\text{Sb}_{1.4}\text{S}_3$   
(Unetched).



Figure 13e. Microstructure of Slow Cooled  $\text{As}_{0.6}\text{Sb}_{1.4}\text{S}_3$   
(Etched).

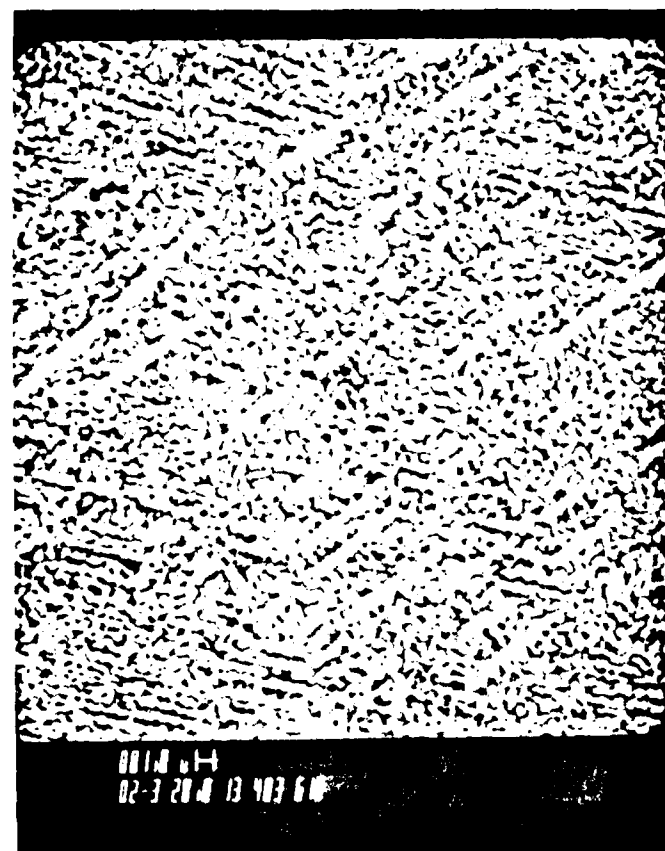


Figure 13f. Microstructure of Slow Cooled  $\text{As}_{0.8}\text{Sb}_{1.2}\text{S}_3$   
(Unetched).



Figure 13g. Microstructure of Slow Cooled  $\text{As}_{0.8}\text{Sb}_{1.2}\text{S}_3$   
(Etched).

because of the interference from the continuous  $\text{As}_2\text{S}_3$  matrix, and thus exhibited an appearance more of isolated crystalites. The presence of the  $\text{As}_2\text{S}_3$  phase inhibits the  $\text{Sb}_2\text{S}_3$  crystal growth, probably because antimony atoms have to diffuse through the viscous matrix phase to reach the growing crystal interface prior to the crystallization.

The specimens with antimony content lower than  $x=1.1$  (which were been found to be totally amorphous by X-ray analysis) showed no features (Figure 13h) until they were etched with a NaOH solution. Etching revealed a random network-like feature with grain size ranging from  $1000\text{\AA}$  to  $3000\text{\AA}$  (Figure 13i). This network-like microstructure seems to exist only in melt quenched glasses and not in vapor deposited films in this study, even though Chen et al. [Ref.52] observed a similar network-like structure (they call it a domain structure) in thin films. A microscopic study of the vapor deposited films, utilizing Transmission Electron Microscopy (TEM), did not identify such structures. The as-deposited films seemed totally amorphous and featureless, whether the film was a thin film directly vapor deposited on a thin film carbon substrate for TEM, or a thick film which was thinned by ion-milling or by microtome technique.

In quenched specimens, the size of crystal grain was found to be smaller, and the crystal diameter of the quenched  $\text{As}_{0.4}\text{Sb}_{1.6}\text{S}_3$  was around  $1\text{ }\mu\text{m}$  (Figures 14b and 14c)

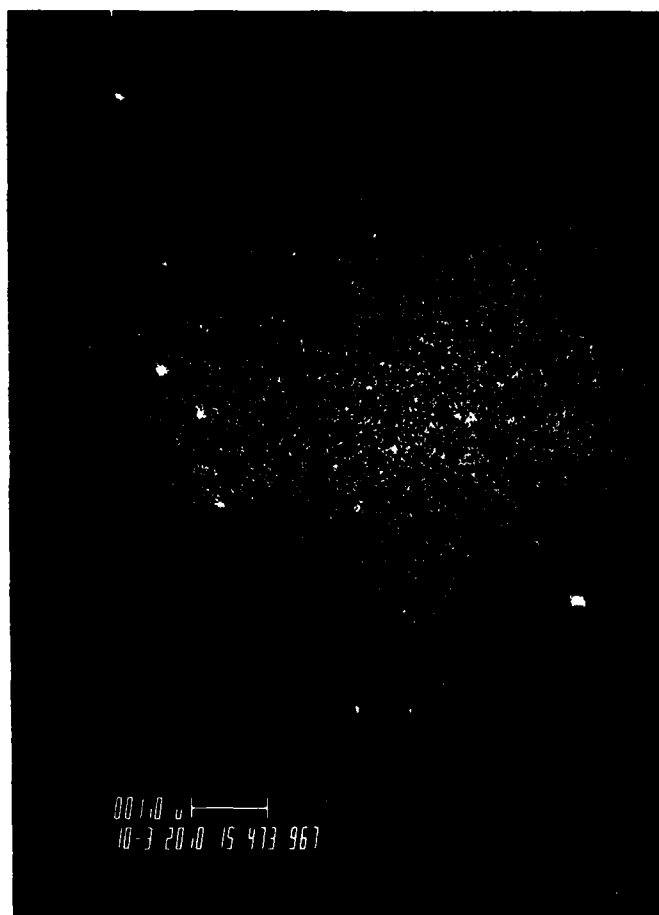


Figure 13h. Microstructure of Slow Cooled  $\text{As}_{2-x}\text{Sb}_x\text{S}_3$   
where  $x < 1.1$  (Unetched).

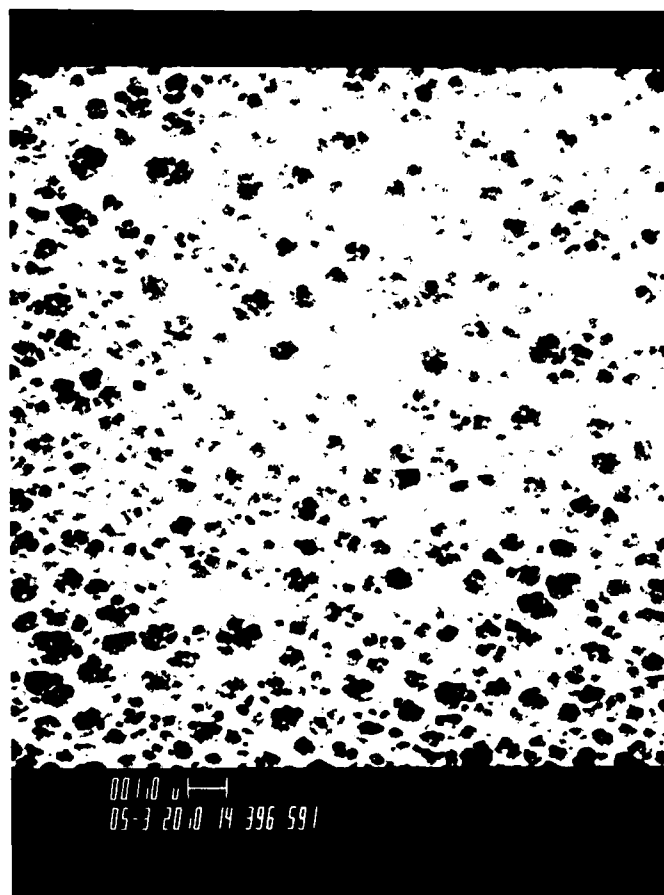


Figure 13i. Microstructure of Slow Cooled  $\text{As}_{2-x}\text{Sb}_x\text{S}_3$   
where  $x < 1.1$  (Etched).

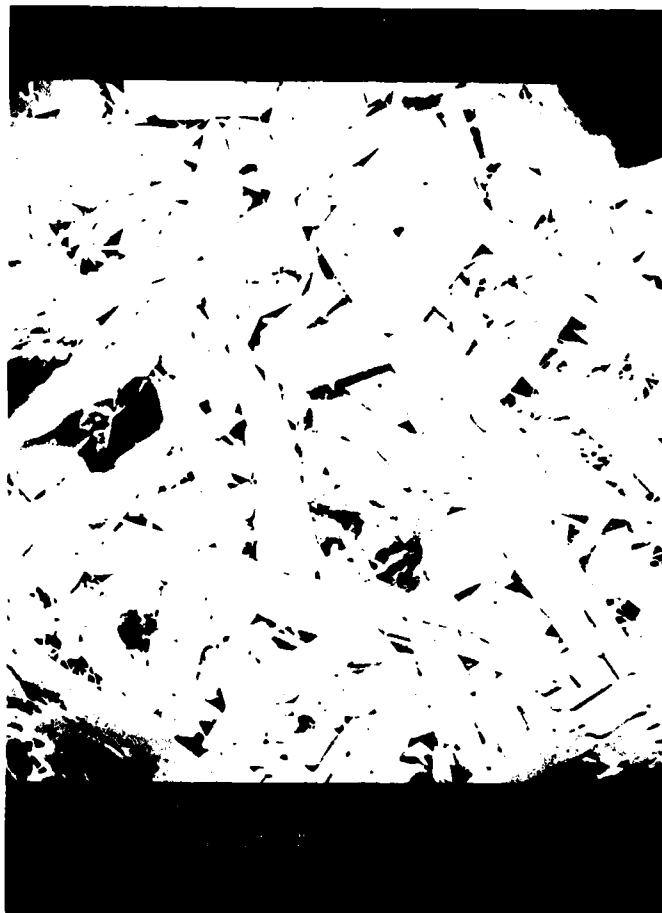


Figure 14a. Microstructure of Quenched  $\text{As}_{0.2}\text{Sb}_{1.8}\text{S}_3$   
(Etched).

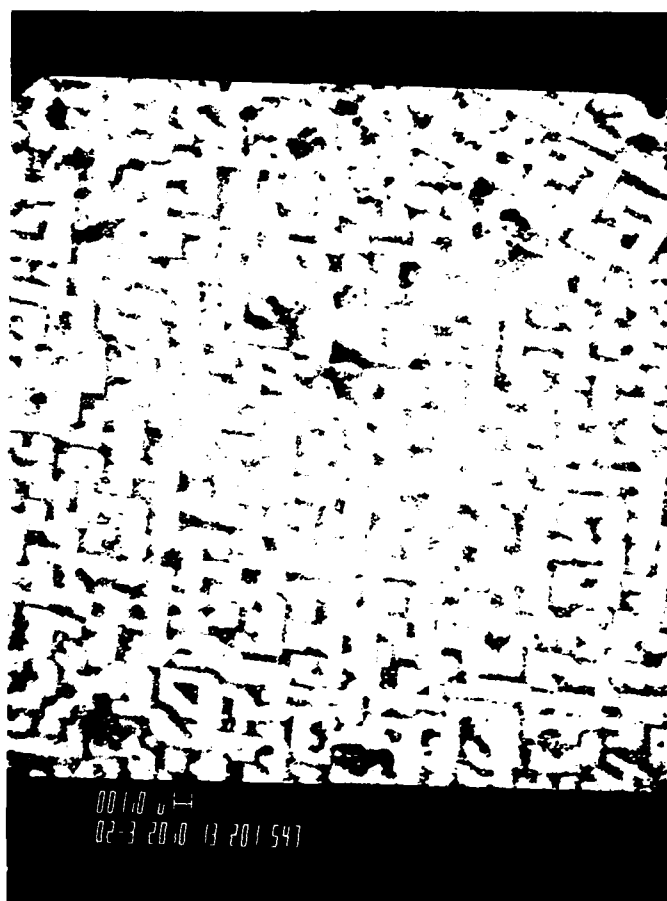


Figure 14b. Microstructure of Quenched  $\text{As}_{0.4}\text{Sb}_{1.6}\text{S}_3$   
(Unetched).

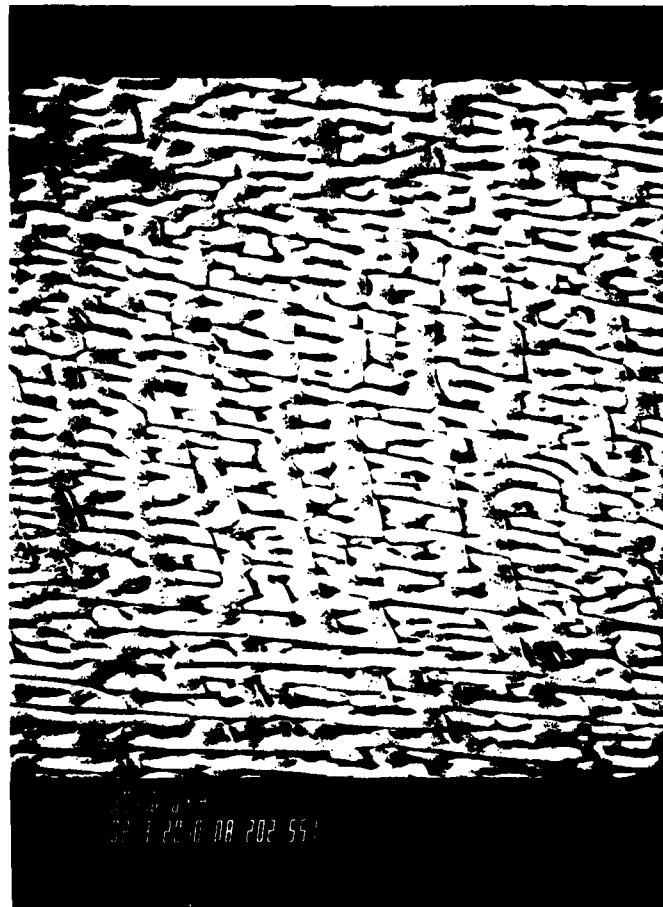


Figure 14c. Microstructure of Quenched  $\text{As}_{0.4}\text{Sb}_{1.6}\text{S}_3$  (Etched).

as compared to 10  $\mu\text{m}$  (Figure 13c) for slow cooled specimens with the same composition. This is probably because glassy  $\text{As}_2\text{S}_3$  matrix rapidly gained viscosity during the quench, and inhibited the diffusion of antimony atoms and subsequent crystallization of the  $\text{Sb}_2\text{S}_3$  phase. The quenched specimens became totally featureless at antimony content lower than  $x=1.4$  (Figure 14d). A random network-like feature similar to the one in Figure 13i (for slow cooled arsenic rich specimens) showed up upon etching these featureless samples (Figure 14e).

Figures 13i and 14e consist of two phases; a darker phase which was etched away and the continuous lighter color phase. This microstructure was found to be the same for different compositions, including the  $\text{As}_2\text{S}_3$  glass without any antimony addition. The grain size and the relative amount of the darker phase to the lighter phase did not change with composition, indicating that this microstructure does not represent a compositional segregation or the two phase glass structure, consisting of  $\text{As}_2\text{S}_3$  and  $\text{Sb}_2\text{S}_3$  phases, as proposed by Kawamoto and Tsuchihashi. It was concluded that this microstructure reflected the cluster or long range order known to exist in glasses [Ref.2 and 16].

The sulfur deficient specimens, even at lower antimony content, were found to crystallize on slow cooling as seen in Figures 15a and 15b. Though an X-ray analysis detected  $\text{AsS-}\beta$  crystal in addition to the  $\text{Sb}_2\text{S}_3$  crystal in these

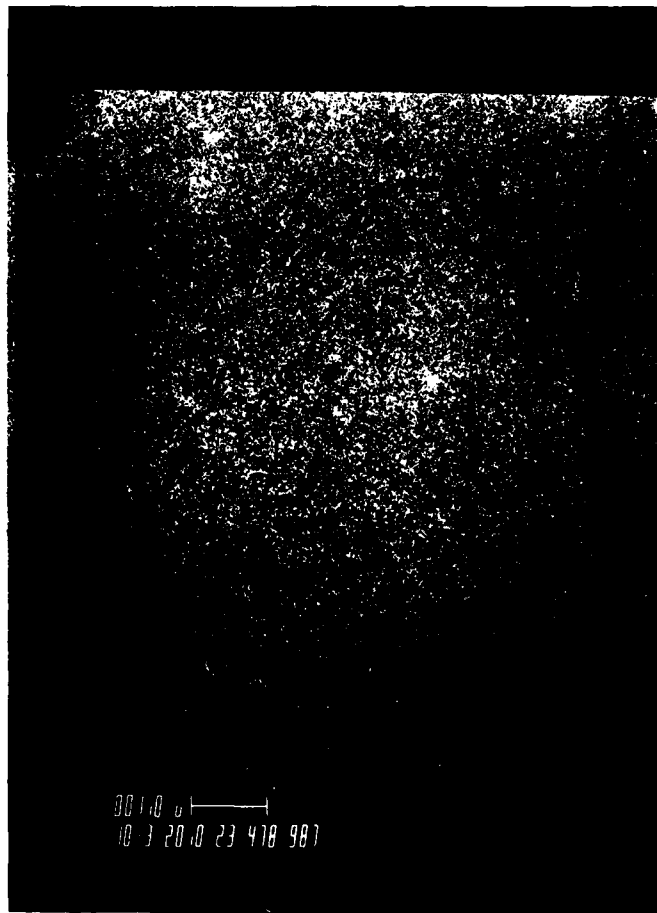


Figure 14d. Microstructure of Quenched  $\text{As}_{2-x}\text{Sb}_x\text{S}_3$  where  $x < 1.4$  (Unetched).

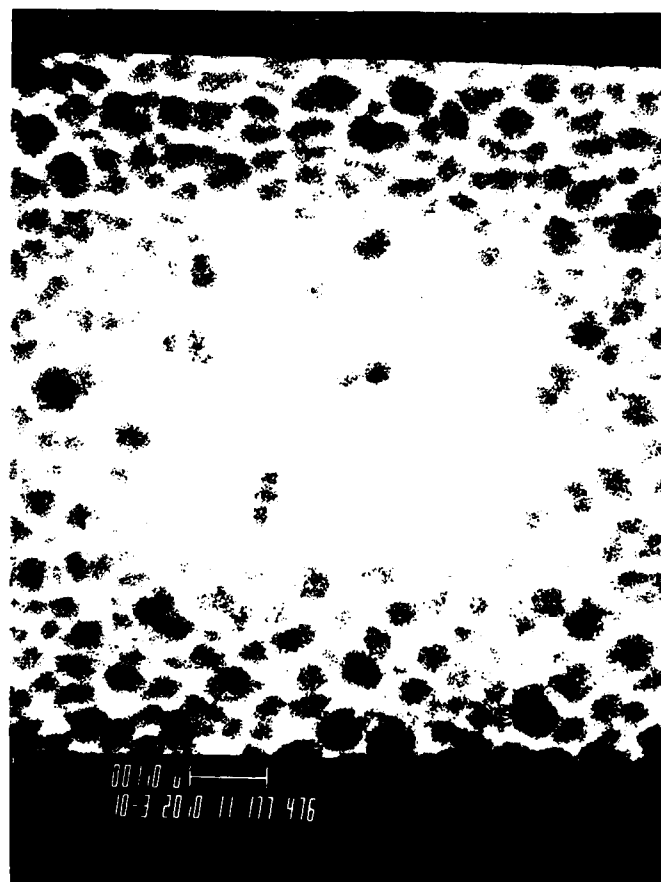


Figure 14e. Microstructure of Quenched  $\text{As}_{2-x}\text{Sb}_x\text{S}_3$  where  $x < 1.4$  (Etched).

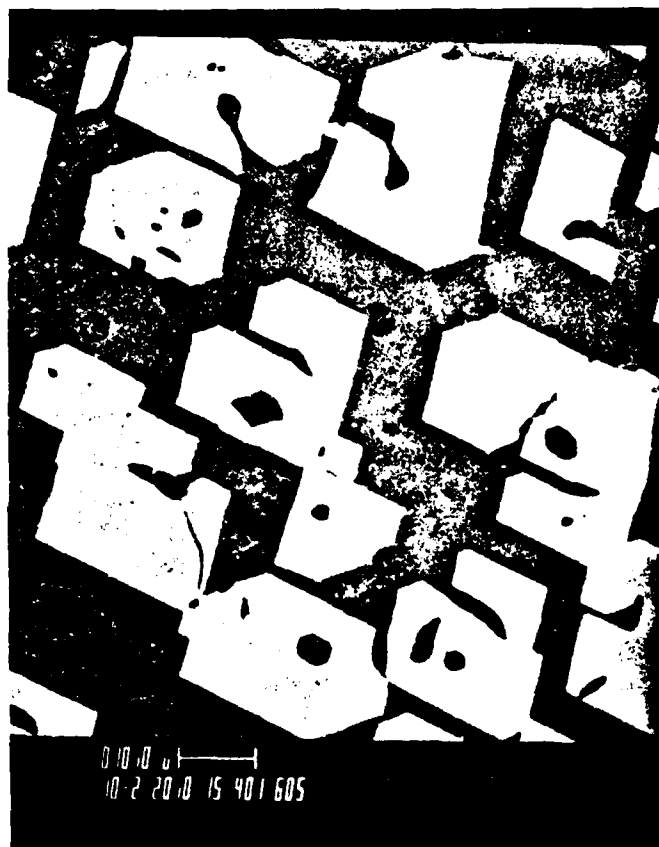


Figure 15a. Microstructure of Slow Cooled Sulfur Deficient  $\text{As}_{1.0}\text{Sb}_{1.0}\text{S}_{2.66}$  (Unetched)



Figure 15b. Microstructure of Slow Cooled Sulfur  
Deficient  $\text{As}_{1.0}\text{Sb}_{1.0}\text{S}_{2.66}$  (Etched).

samples, the existence of such a second crystalline phase was not obvious in Figures 15a and 15b. The quenched sulfur deficient specimens, which were amorphous in X-ray analysis, showed a darker second phase in the featureless matrix phase (Figures 15c and 15e). Upon etching these samples (Figures 15d and 15f), the matrix phase desolved to reveal a spherical second phase corresponding to the darker phase in Figures 15c and 15e. The second phase was identified to be AsS by EDXA. The sizes of this spherical phase were around  $2000\text{\AA}$  for  $\text{As}_{1.0}\text{Sb}_{1.0}\text{S}_{2.67}$  and  $1.5\text{ }\mu\text{m}$  for  $\text{As}_{1.2}\text{Sb}_{0.8}\text{S}_{2.55}$ , which seemed to be highly dependent on the degree of sulfur deficiency.

#### 4. THERMAL ANALYSIS

##### a. Characteristic Temperatures ( $T_g$ , $T_c$ , and $T_l$ )

##### Determined by the Dynamic Heating Method

The DSC traces for quenched stoichiometric specimens are shown in Figure 16. The compositions with antimony content lower than  $x=1.0$  exhibited only the glass transition, which appears as a step change in the DSC trace as seen in the trace(a). This is due to a step increase in specific heat of a glass sample upon heating through the glass transition range as explained in Chapter I. The compositions with antimony content between  $x=1.2$  and  $x=1.6$  showed the glass transition, crystallization peak (exothermic), and fusion peak (endothermic) as seen in the trace (b). The compositions with antimony content higher

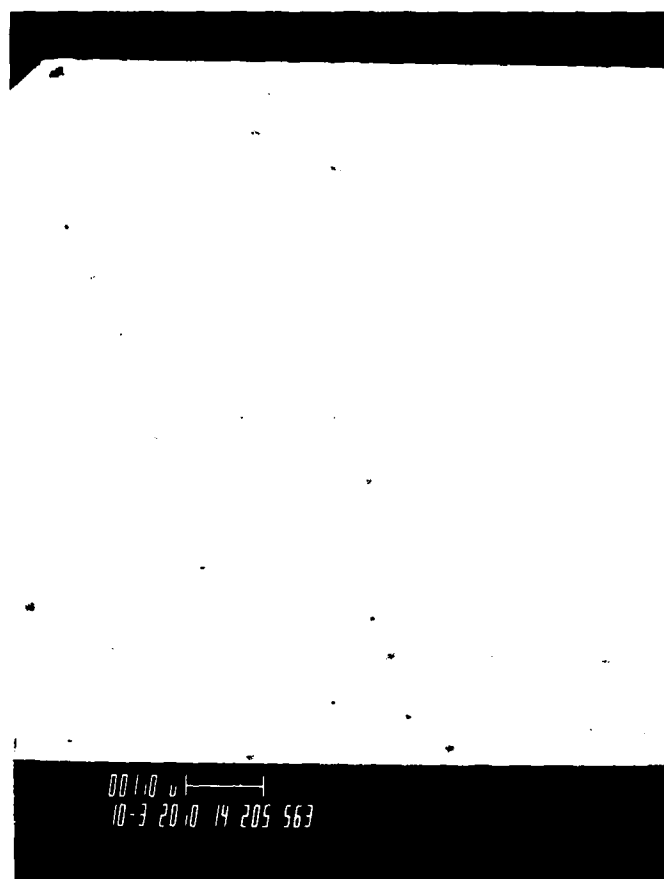


Figure 15c. Microstructure of Quenched Sulfur Deficient  $\text{As}_{1.0}\text{Sb}_{1.0}\text{S}_{2.67}$  (Unetched).

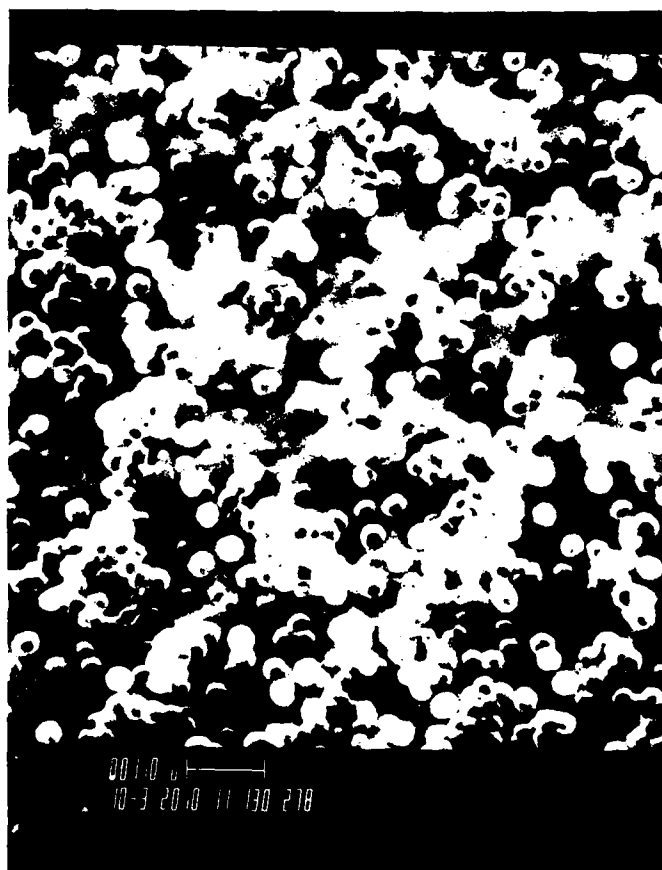


Figure 15d. Microstructure of Quenched Sulfur Deficient  
 $\text{As}_{1.0}\text{Sb}_{1.0}\text{S}_{2.67}$  (Etched).



Figure 15e. Microstructure of Quenched Sulfur Deficient  
 $\text{As}_{1.2}\text{Sb}_{0.8}\text{S}_{2.55}$  (Unetched).



Figure 15f. Microstructure of Quenched Sulfur Deficient  
 $\text{As}_{1.2}\text{Sb}_{0.8}\text{S}_{2.55}$  (Etched).

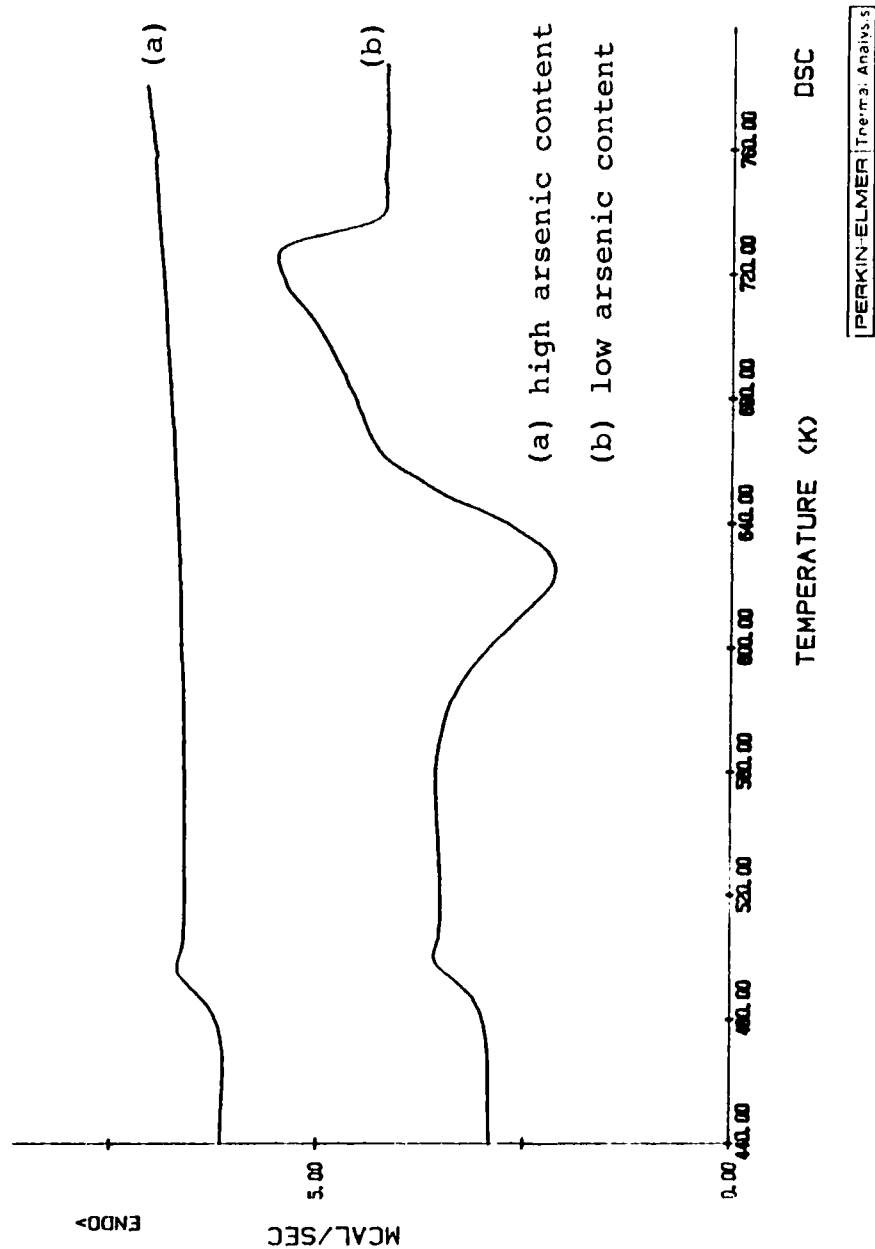


Figure 16. DSC Traces for Quenched Stoichiometric Specimens.

than  $x=1.8$  were already crystallized, and they showed neither glass transition nor crystallization, and their fusion temperatures were above the upper temperature limit of the experimental set up.

The slow cooled stoichiometric specimens did not show further crystallization upon heating in DSC. Their glass transition regions were always associated with endothermic peaks, and this phenomena was especially prominent in compositions with higher arsenic content (Figure 17). Though the X-ray diffraction and SEM data showed that  $\text{As}_{2-x}\text{Sb}_x\text{S}_3$  system is a two phase immiscible system, when crystallized, the eutectic melting peak, characteristic of two phase immiscible systems [Ref.48], was missing in the DSC traces for stoichiometric samples. This is because its eutectic composition is in the glass forming region and does not crystallize within the experimental time scale used in this study.

The sulfur deficient specimens exhibited either two or three endothermic peaks at around  $570^\circ\text{K}$  -  $580^\circ\text{K}$  (Figures 18 and 19). These additional peaks may be due to the meltings of  $\text{As}_2\text{S}_2$  and adjacent compositions in  $\text{As}_2\text{S}_3$ - $\text{As}_2\text{S}_2$  system as seen from Figure 20 [Ref.49] or the eutectic melting in  $\text{Sb}_2\text{S}_3$ - $\text{As}_2\text{S}_2$  system, the phase diagram of which has not been found.

The DSC traces of the vapor deposited films are shown in Figure 21. The trace (a) is for  $\text{Sb}_2\text{S}_3$  film, trace (b) is

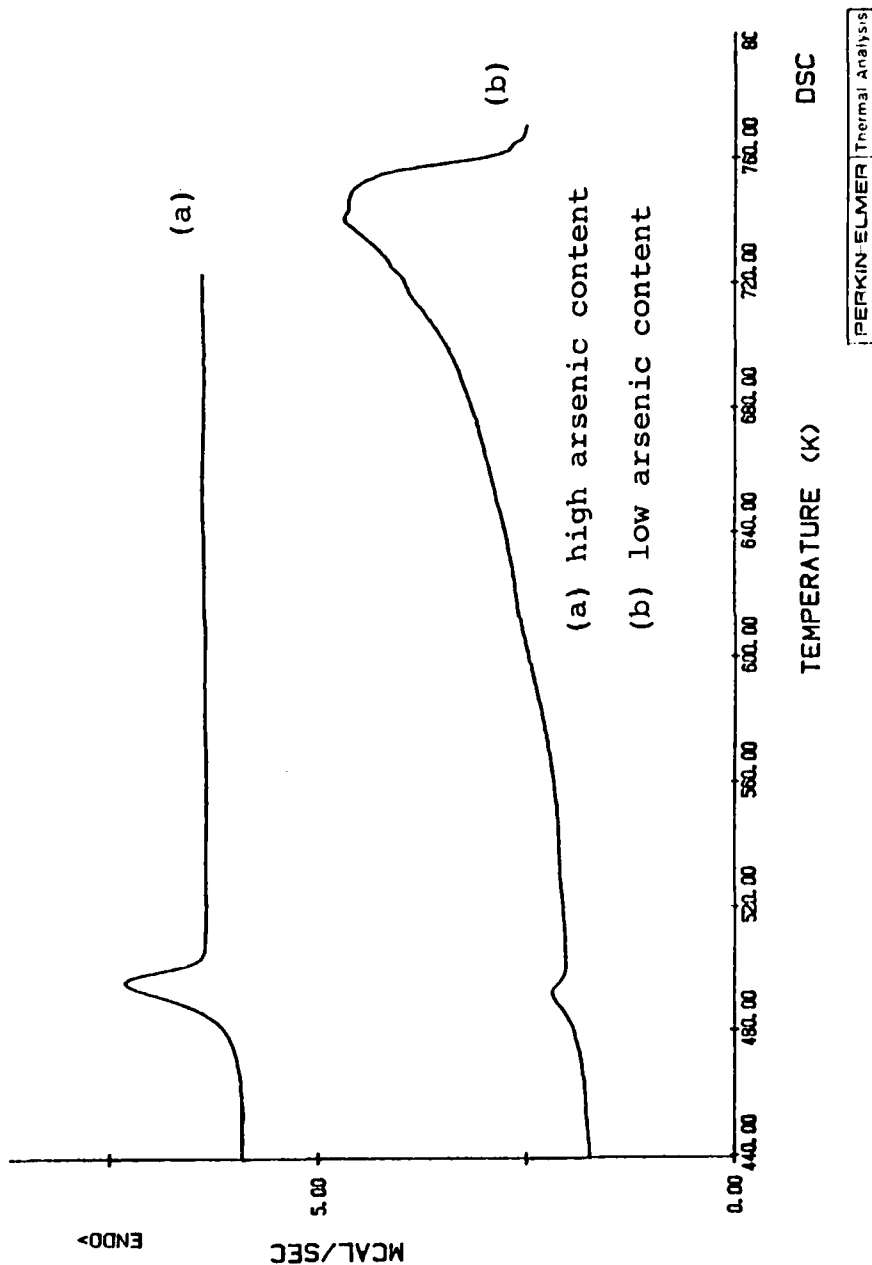


Figure 17. DSC Traces for Slow Cooled Stoichiometric Specimens.

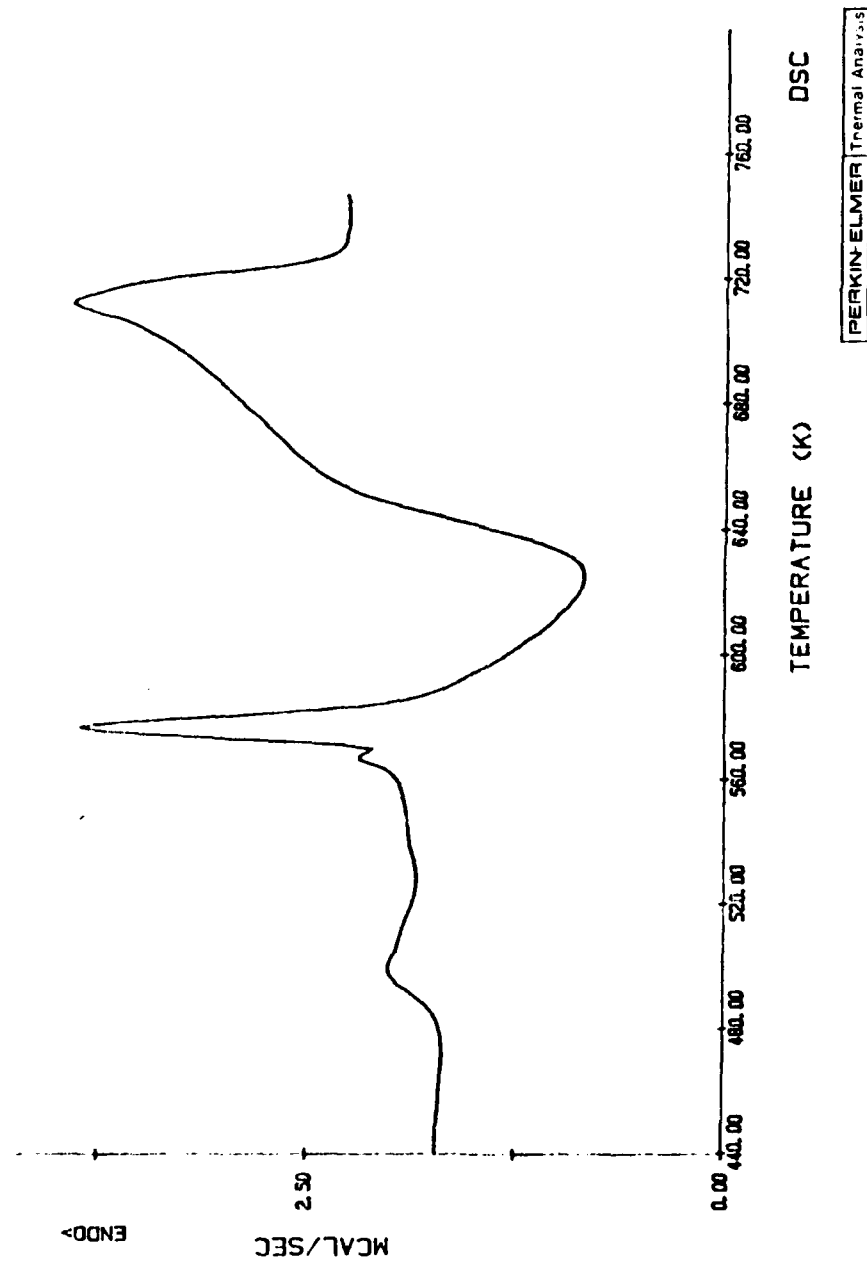


Figure 18. DSC Trace for Quenched Sulfur Deficient Specimen.

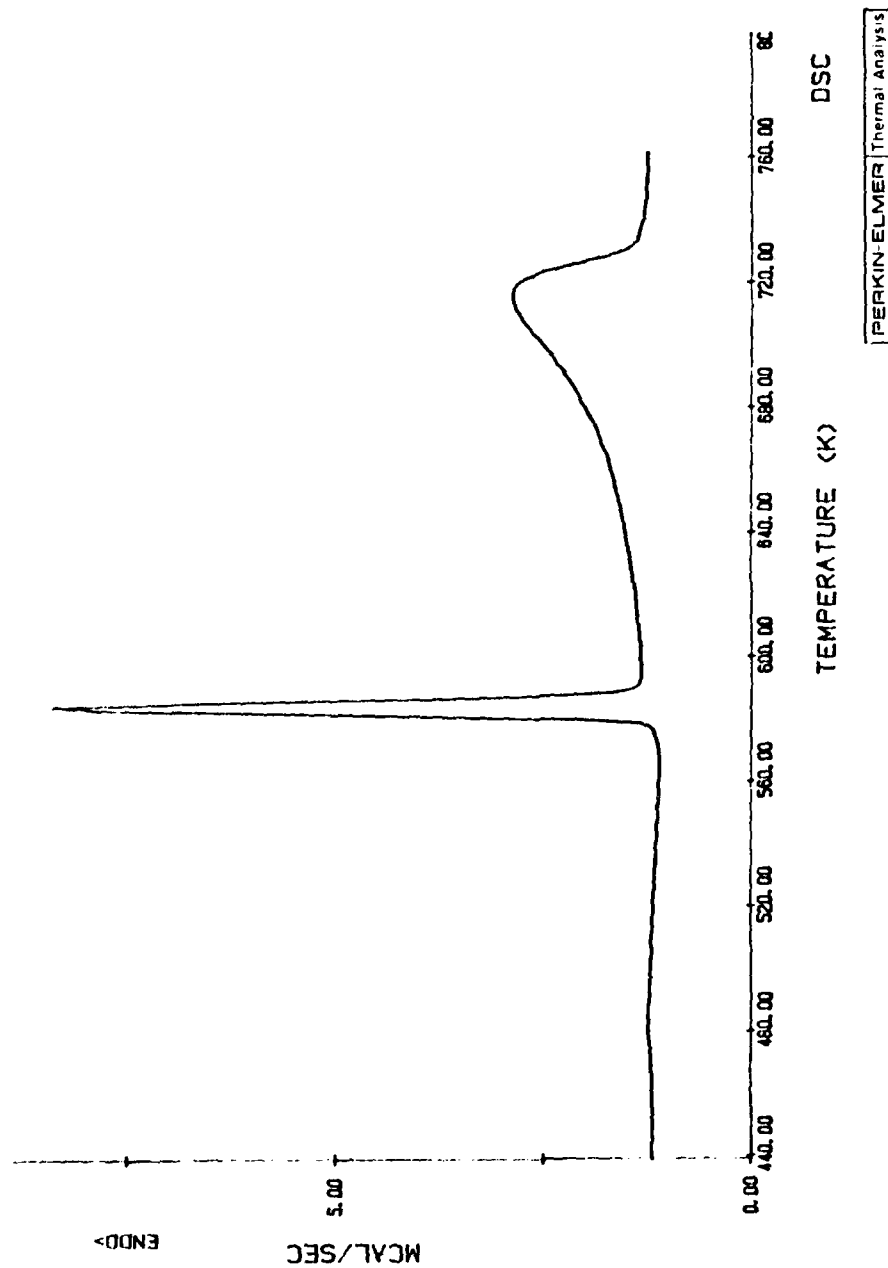


Figure 19. DSC Trace for Slow Cooled Sulfur Deficient Specimen.

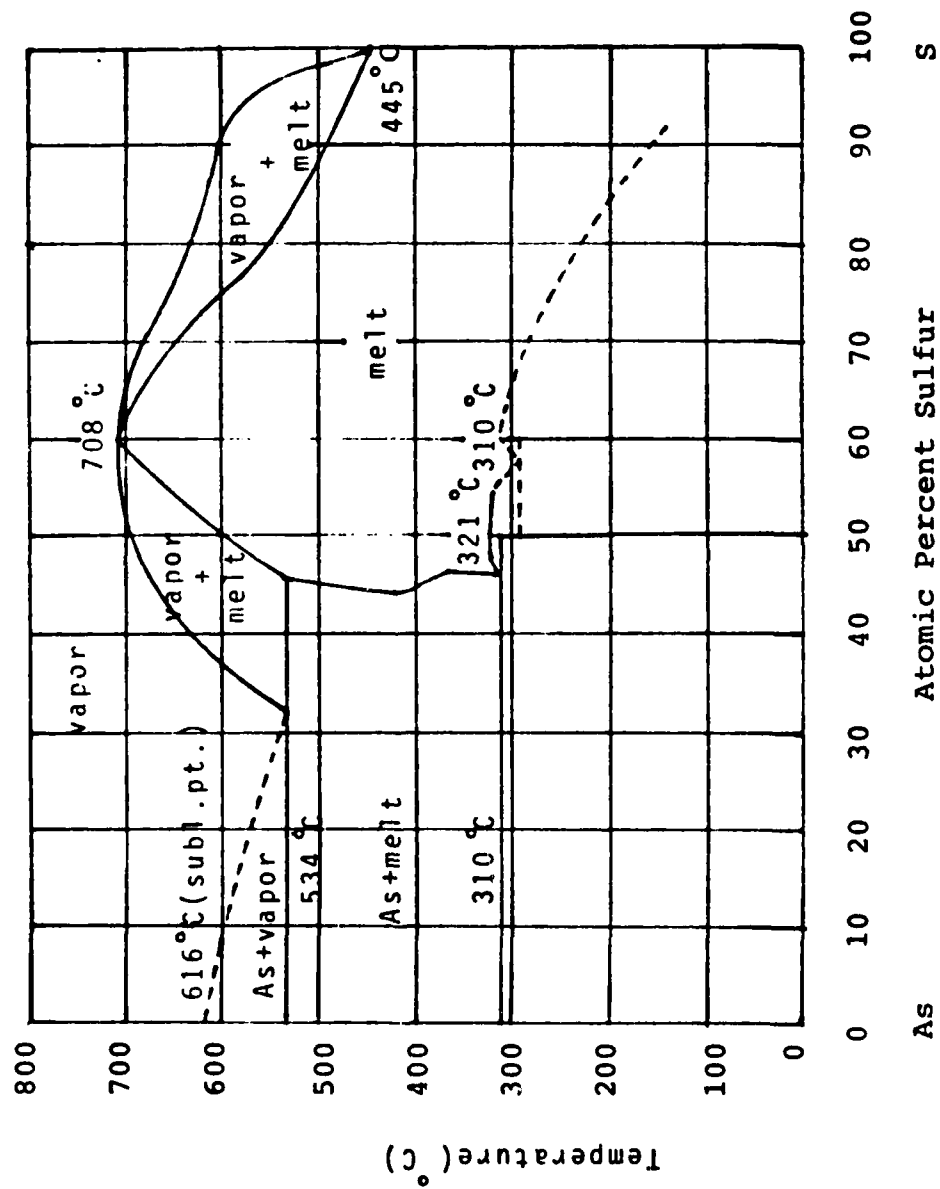


Figure 20. As-S Phase Diagram [Ref.49].

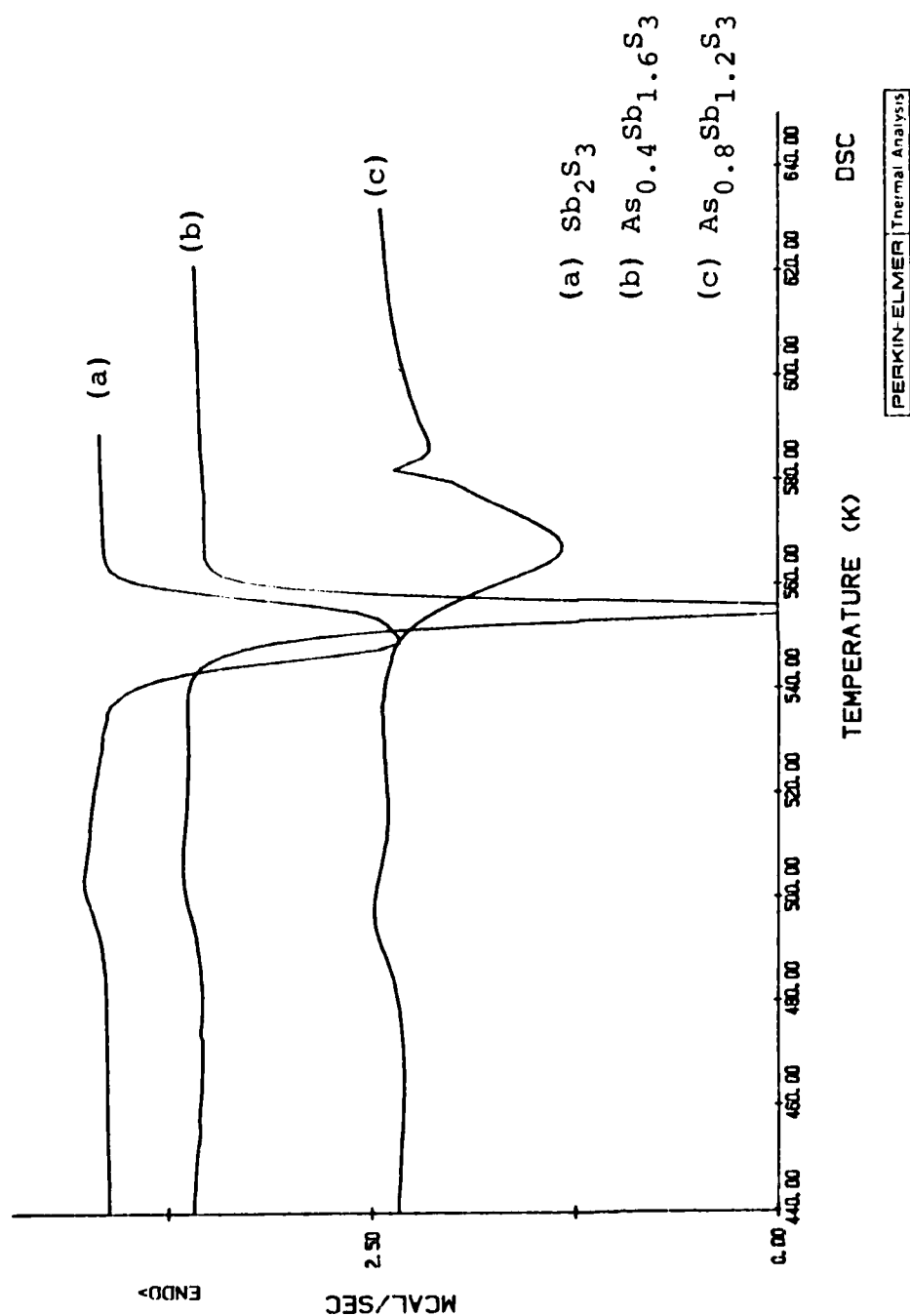


Figure 21. DSC Traces for Vapor Deposited Films.

from  $\text{As}_{0.4}\text{Sb}_{1.6}\text{S}_3$  film, and trace (c) is for  $\text{As}_{0.8}\text{Sb}_{1.2}\text{S}_3$  film. The trace (c) showed an extra endothermic peak around  $570^\circ\text{K}$ , which was characteristic of a sulfur deficient composition. The crystallization peaks were found to occur at lower temperatures and were much sharper as compared to the crystallization peaks for bulk specimens. It was assumed at this time that the difference in crystallization characteristics of films as compared to bulk samples was solely due to the larger surface area associated with films. Electrical resistivity measurements have shown that the crystallization starts at the surface in chalcogenide glasses [Ref.50]. To test this assumption, the bulk samples were ground to a powder to increase their surface area, and their DSC data were compared with those of bulk specimens (Figure 22a). Crystallization occurred abruptly at lower temperatures for these samples, verifying that the crystallization, indeed, starts at the surface, and it is enhanced by an increase in surface area. Later, the surface crystallization was directly observed by a optical microscopy. Figure 22b shows the crystallization starting on the surface of a bulk  $\text{As}_{0.8}\text{Sb}_{1.2}\text{S}_3$  glass specimen, which has been isothermally annealed at the crystallization temperature ( $600^\circ\text{K}$ ) for 3 minutes. Figure 22c is the same microstructure observed at a higher magnification, showing needle-like crystal growth in the grains.

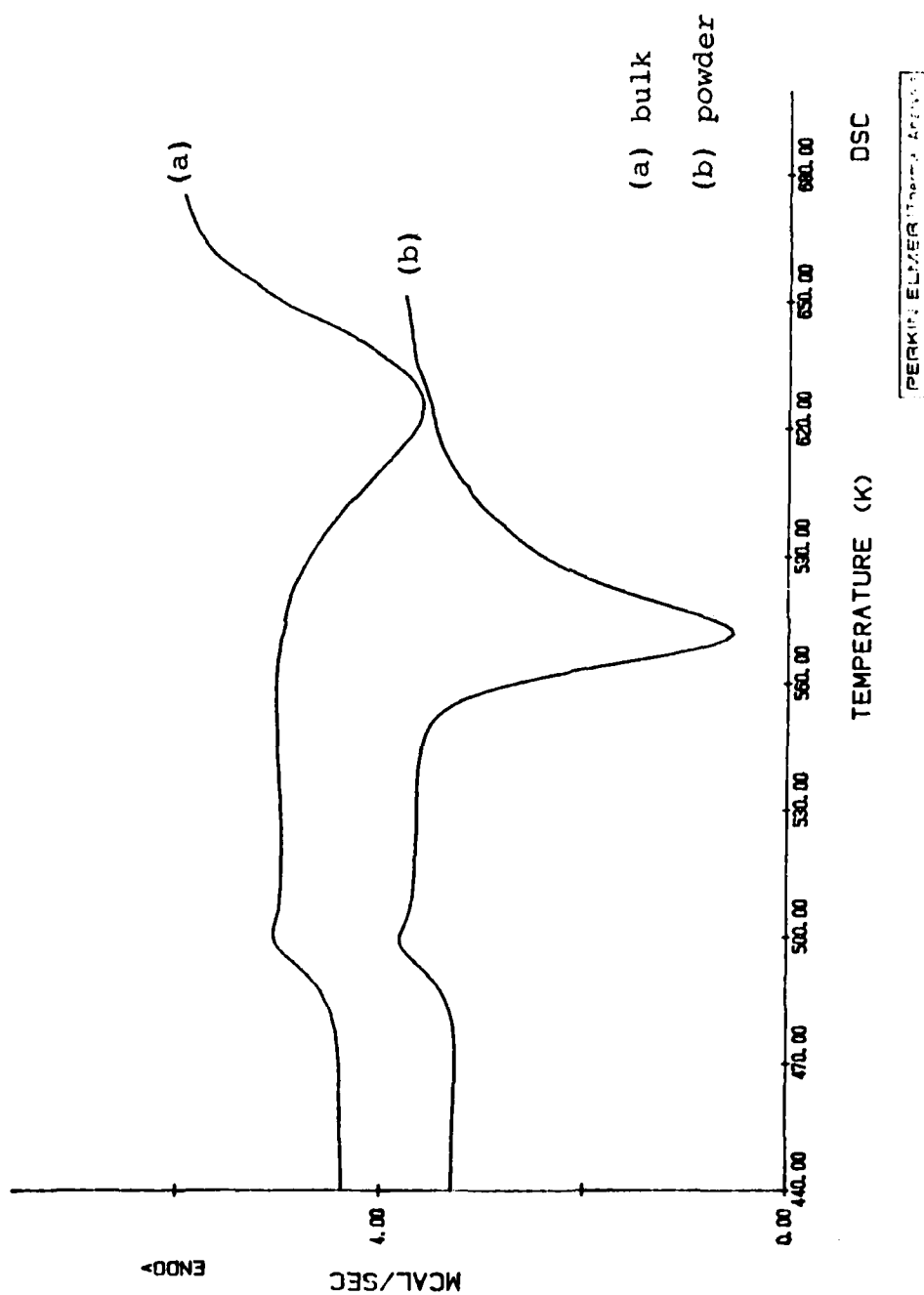


Figure 22a. DSC Traces - Comparison of Bulk Sample and Powdered Sample of the Same Composition.



Figure 22b. Crystallization Starting at the Surface of  $\text{As}_{0.8}\text{Sb}_{1.2}\text{S}_3$  Bulk Specimen.



10um

Figure 22c. Dendritic Growth in the Surface Crystallization  
of  $\text{As}_{0.8}\text{Sb}_{1.2}\text{S}_3$  Bulk Specimen.

All characteristic temperatures ( $T_g$ ,  $T_c$ , and  $T_l$ ) determined from the dynamic heating DSC traces are summarized in Table 3. Figure 23 shows the glass transition temperatures,  $T_g$ , for bulk samples plotted as a function of composition. The average standard deviation in  $T_g$  measurements was  $\pm 0.8^\circ\text{K}$ .  $T_g$  was found to increase with antimony substitutions, however, the variation was less than  $15^\circ\text{K}$  throughout the compositional range. This result is expected in two phase immiscible systems in general, because the bond strength and mechanism do not change significantly with composition, in immiscible systems. In addition for this case, little change is expected since As-S bond energy (61 kcal/mole) is little different from Sb-S bond energy (62 kcal/mole) [Ref.5].

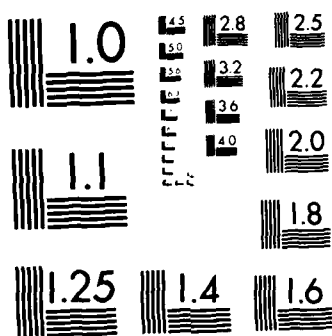
The temperature of maximum crystallization rate,  $T_c$ , for various forms of samples are plotted as a function of composition, for (a) bulk samples, (b) films, and (c) powdered samples, in Figure 24. The average standard deviation in  $T_c$  measurements was  $\pm 3.5^\circ\text{K}$  for the bulk samples and less than  $1^\circ\text{K}$  for the films and the powder samples. The reason for the larger standard deviations for the bulk specimens is most likely due to the difference in total surface area of the DSC samples.  $T_c$  was found to decrease drastically with antimony substitutions above  $x=1.1$ .  $T_c$  of the film with a composition at  $x=1.6$  was between those of the bulk and the powder, as expected from

CHALCOGENIDE GLASSES PART 4 CRYSTALLIZATION AND GLASS  
TRANSITION CHARACTER. (U) AIR FORCE WRIGHT AERONAUTICAL  
LABS WRIGHT-PATTERSON AFB OH. K WHITE ET AL. JUN 86  
AFMNL-TR-86-4075 F/G 1/2

RE

**UNCLASSIFIED**

**F/G 1/2**



MICROCOPY RESOLUTION TEST CHART

TABLE 3. SUMMARY OF DSC DATA -  $T_g$ ,  $T_c$ , and  $T_l$  values  
Measured at Four Different Heating Rates

Bulk Samples - Liquid Nitrogen Quenched					
Compositions	Charac. Temp K <sup>o</sup>	DSC Heating Rates			
		5 <sup>o</sup> K/min	10 <sup>o</sup> K/min	20 <sup>o</sup> K/min	40 <sup>o</sup> K/min
As <sub>2</sub> S <sub>3</sub>	T <sub>g</sub>	473.6	478.4	485.4	492.1
	T <sub>c</sub>	-	-	-	-
	T <sub>l</sub>	-	-	-	-
As <sub>1.8</sub> Sb <sub>0.2</sub> S <sub>3</sub>	T <sub>g</sub>	472.4	476.9	483.2	491.0
	T <sub>c</sub>	-	-	-	-
	T <sub>l</sub>	-	-	-	-
As <sub>1.6</sub> Sb <sub>0.4</sub> S <sub>3</sub>	T <sub>g</sub>	473.7	479.0	484.9	492.6
	T <sub>c</sub>	-	-	-	-
	T <sub>l</sub>	-	-	-	-
As <sub>1.4</sub> Sb <sub>0.6</sub> S <sub>3</sub>	T <sub>g</sub>	475.7	480.1	487.0	494.2
	T <sub>c</sub>	-	-	-	-
	T <sub>l</sub>	-	-	-	-
As <sub>1.2</sub> Sb <sub>0.8</sub> S <sub>3</sub>	T <sub>g</sub>	477.5	481.6	488.1	495.2
	T <sub>c</sub>	-	-	-	-
	T <sub>l</sub>	-	-	-	-
As <sub>1.0</sub> Sb <sub>1.0</sub> S <sub>3</sub>	T <sub>g</sub>	479.1	483.2	489.5	496.9
	T <sub>c</sub>	-	-	-	-
	T <sub>l</sub>	-	-	-	-
As <sub>0.8</sub> Sb <sub>1.2</sub> S <sub>3</sub>	T <sub>g</sub>	480.3	484.6	490.3	498.3
	T <sub>c</sub>	601.5	612.2	626.5	642.0
	T <sub>l</sub>	729.3			
As <sub>0.6</sub> Sb <sub>1.4</sub> S <sub>3</sub>	T <sub>g</sub>	482.3	486.8	492.9	500.3
	T <sub>c</sub>	575.0	583.5	596.6	611.3
	T <sub>l</sub>	758.1			
As <sub>0.4</sub> Sb <sub>1.6</sub> S <sub>3</sub>	T <sub>g</sub>	485.5	490.0	495.0	502.2
	T <sub>c</sub>	552.1	558.3	572.0	580.5
	T <sub>l</sub>	789.5			

TABLE 3. (cont)

Powdered Bulk Samples - Liquid Nitrogen Quenched					
Compositions	Charac. Temp. Ko	DSC Heating Rates			
		5oK/min	10oK/min	20oK/min	40oK/min
As <sub>0.8</sub> Sb <sub>1.2</sub> S <sub>3</sub>	Tg	479.9	484.3	489.3	498.6
	Tc	552.8	561.8	571.3	585.5
	T <sub>1</sub>	729.0			
As <sub>0.6</sub> Sb <sub>1.4</sub> S <sub>3</sub>	Tg	482.7	485.9	491.7	500.3
	Tc	533.0	538.5	545.2	554.4
	T <sub>1</sub>	758.1			
As <sub>0.4</sub> Sb <sub>1.6</sub> S <sub>3</sub>	Tg	485.9	489.6	494.4	502.3
	Tc	526.0	550.3	554.6	557.2
	T <sub>1</sub>	789.5			
Sulfur Deficient Bulk Samples - Liquid Nitrogen Quenched					
As <sub>1.2</sub> Sb <sub>0.8</sub> S <sub>2.55</sub>	Tg	480.2	484.4	490.6	500.3
	Tc	586.	600.6	628.4	648.3
	T <sub>1</sub>	719.1			
As <sub>1.0</sub> Sb <sub>1.0</sub> S <sub>2.67</sub>	Tg	479.5	484.3	490.6	498.6
	Tc	591.3	607.5	623.6	638.3
	T <sub>1</sub>	726.1			
Sulfur Deficient Powdered Samples - Liquid Nitrogen Quenched					
As <sub>1.2</sub> Sb <sub>0.8</sub> S <sub>2.55</sub>	Tg	480.2	484.1	489.9	498.6
	Tc	564.0	570.5	580.0	593.5
	T <sub>1</sub>	719.1			
As <sub>1.0</sub> Sb <sub>1.0</sub> S <sub>2.67</sub>	Tg	480.2	484.1	489.3	497.5
	Tc	560.	565.0	573.2	585.2
	T <sub>1</sub>	726.0			

TABLE 3. (cont)

Vapor Deposited Films					
Compositions	Charac. Temp. K°	DSC Heating Rates			
		5°K/min	10°K/min	20°K/min	40°K/min
$\text{As}_{0.8}\text{Sb}_{1.2}\text{S}_3$	T <sub>g</sub>	479.2	482.8	486.2	493.5
	T <sub>c</sub>	549.6	557.4	567.2	579.7
	T <sub>l</sub>	730.0			
$\text{As}_{0.4}\text{Sb}_{1.6}\text{S}_3$	T <sub>g</sub>	490.1	492.3	497.2	501.7
	T <sub>c</sub>	539.4	547.4	555.2	564.2
	T <sub>l</sub>	790.0			
$\text{Sb}_2\text{S}_3$	T <sub>g</sub>	490.0	492.3	497.0	500.6
	T <sub>c</sub>	536.6	544.1	549.5	558.7
	T <sub>l</sub>	(819)			

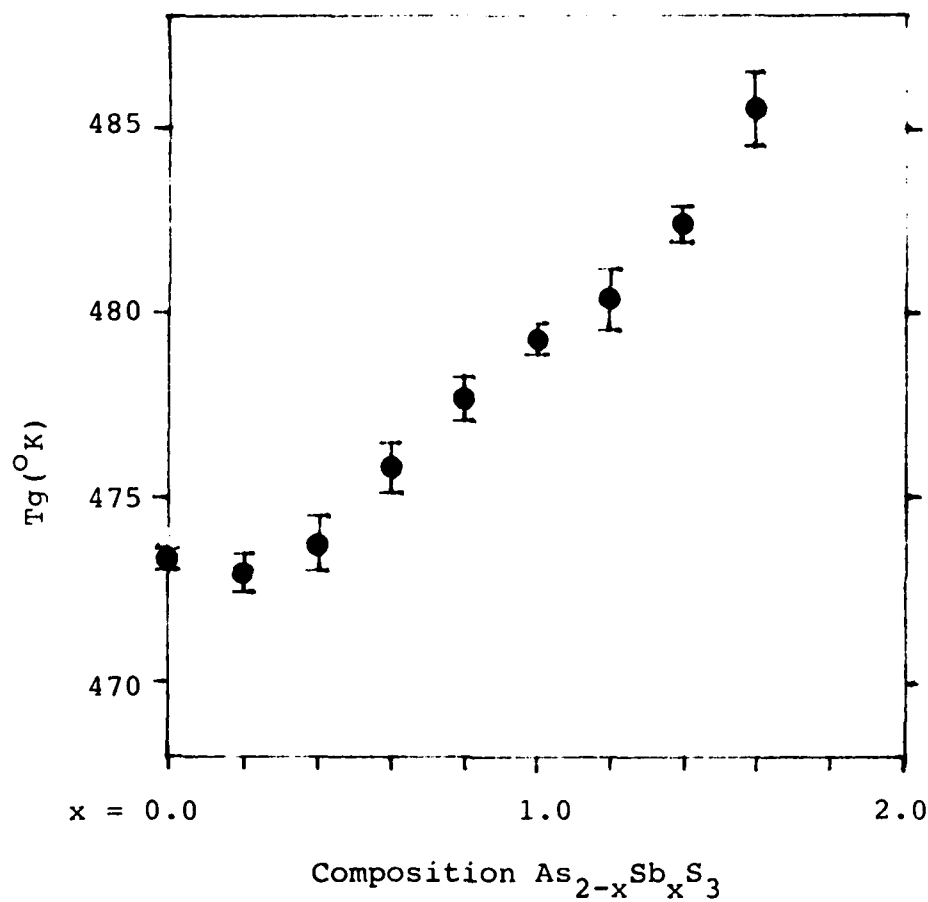


Figure 23. Glass Transition Onset Temperature,  $T_g$ , as a Function of Composition for Bulk Samples.

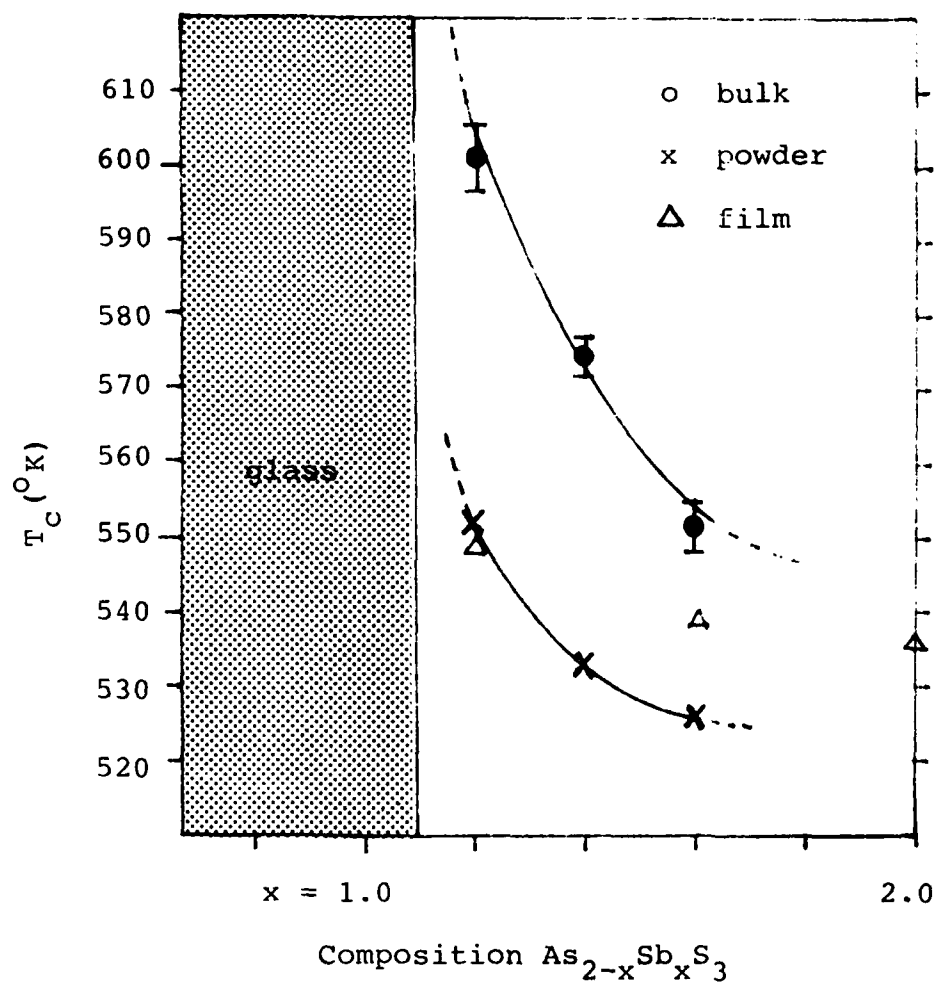


Figure 24. Temperature at the Maximum Crystallization Rate,  $T_c$ , as a Function of Composition for Various Forms of Samples.

the difference in their surface areas. However,  $T_c$  at the composition  $x=1.2$  was about the same for the film and the powder. This was understandable since this free standing film sample possessed the appearance of powder rather than a sheet, after being rubbed off of the aluminum substrate (vigorous rubbing was necessary to remove this film from the substrate because of its strong adhesion). There was only a small difference in the  $T_c$  of films for compositions  $x=1.6$  and  $Sb_2S_3$ .

The liquidus temperatures,  $T_l$ , are plotted as a function of composition in Figure 25. Since the liquidus temperature is defined as the end point of the broad melting peak, which gradually blends into the base line, it was difficult to determine  $T_l$  with an accuracy better than  $\pm 3^\circ K$ . The melting point of  $Sb_2S_3$  was quoted from the literature [Ref.51], since it exceeded the upper temperature limit of this experiment. The shape of liquidus curve seems to be similar to the one shown in Figure 3, for  $As_{2-x}Sb_xSe_3$ . However, it was not possible to determine  $T_l$  of compositions high in arsenic content using the DSC technique because this system has a wide compositional range over which the material is metastable for the experimental times used in this study. There was no difference in  $T_l$ , within an experimental error, between the quenched sample and the slow cooled sample of the same composition.

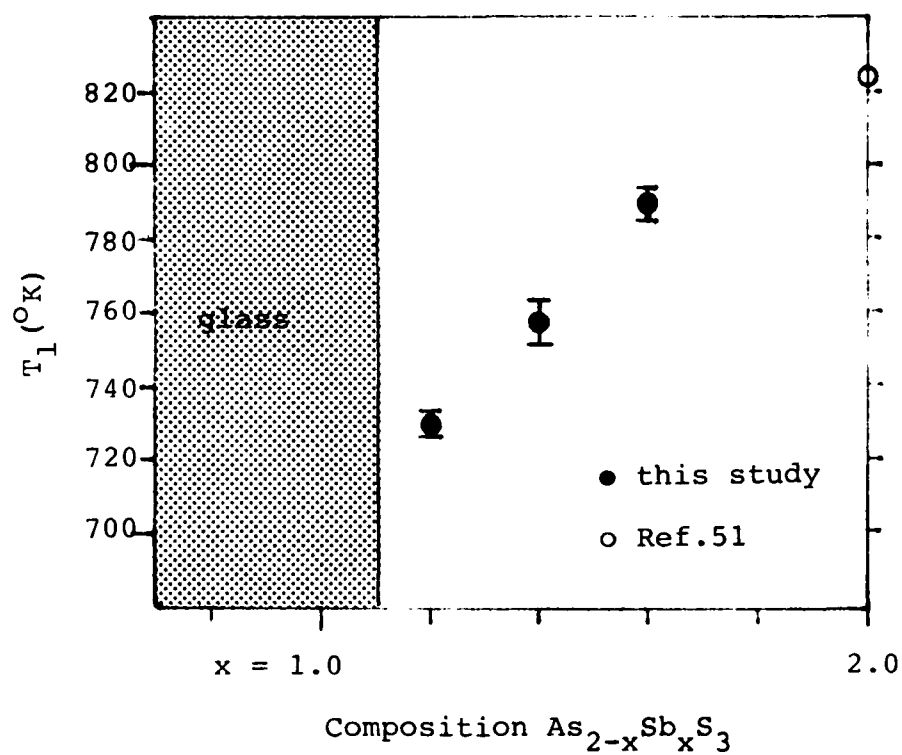


Figure 25. Liquidus Temperature,  $T_L$ , as a Function of Composition.

The Hruby's parameter described in Chapter I is plotted as a function of composition in Figure 26. Because of the rapidly decreasing  $T_c$  and the increasing  $T_1$  with antimony substitutions, the resultant Hruby's parameter, which expresses the glass forming tendency quantitatively, was found to decrease drastically with increasing antimony content. An abrupt change in glass-forming tendency occurred within a narrow compositional range at around  $x=1.1$ . This phenomena can be explained well if the glasses are assumed to consist of  $Sb_2S_3$  phase and  $As_2S_3$  matrix phase, and the crystal grow by interconnection of  $Sb_2S_3$  phase. Because of the slow diffusion of antimony atoms through  $As_2S_3$  phase, the crystallization may practically cease beyond a certain composition where  $Sb_2S_3$  phase becomes isolated from each other.

#### b. Kinetics of Crystallization

The kinetics of crystallization as a function of composition was studied to aid understanding of crystallization process.

The kinetic parameters and activation energy of crystallization, which have been described in Chapter I, were determined utilizing two independent methods; the dynamic heating technique and the isothermal technique.

The temperature of maximum crystallization rate,  $T_c$ , was determined as a function of heating rate ( listed on Table 3), and was used to calculate the dynamic heating

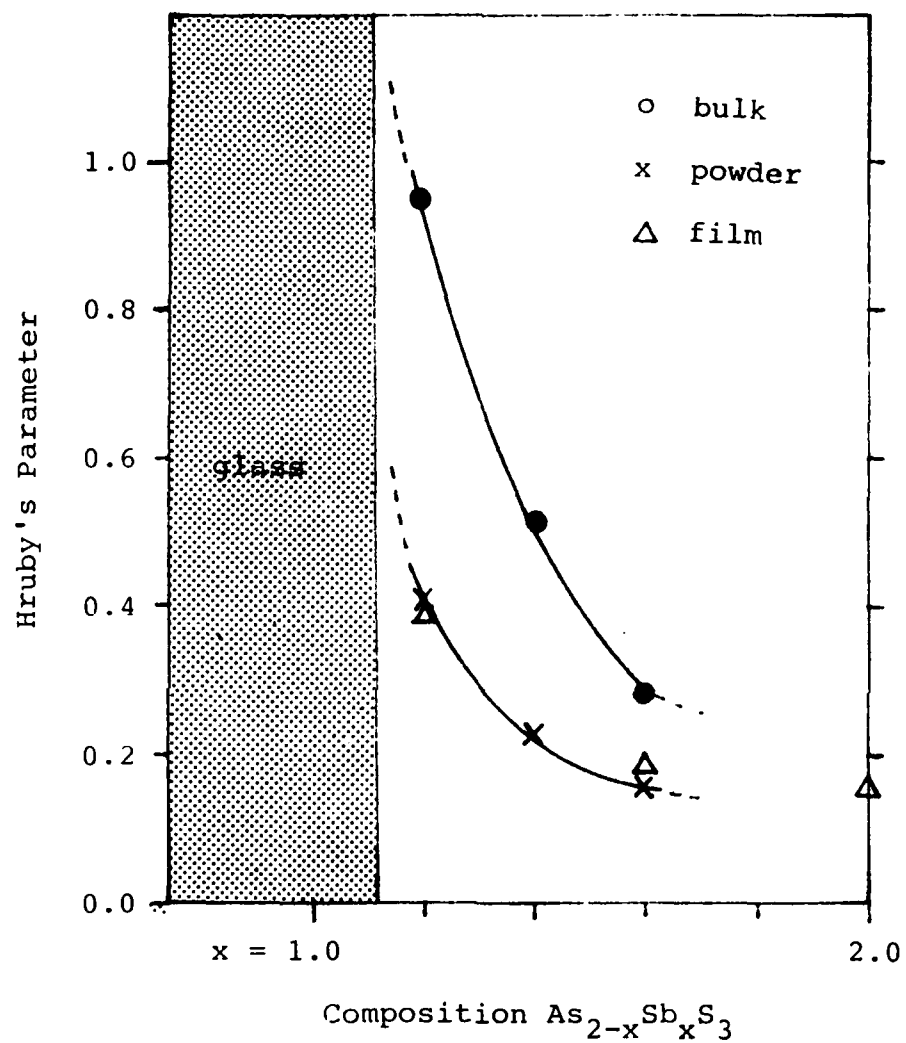


Figure 26. Hruby's Parameter as a Function of Composition for Various Forms of Samples.

crystallization kinetics utilizing the procedure discussed in Chapter II. The plots of  $\ln q/T_c$  as a function of  $1/T_c$ , where  $q$  is a heating rate, are shown in Figures 36a through 36h in Appendix C, for each specimen. The error bars represent the standard deviation of four identical measurements. For the film samples, the error bars were determined only at one heating rate ( $20^\circ\text{K}/\text{min}$ ), because the data were found to be very reproducible (variation in  $T_c$  was within  $\pm 1^\circ\text{K}$ ). The standard deviation in the vertical direction is negligible. The quantity,  $E_a/n$ , of a sample was calculated from the slope of the straight line determined by a linear regression analysis. It was not possible to obtain  $E_a$  and  $n$  values independently with this analysis technique. An uncertainty in the determination of  $E_a/n$  was calculated according to the error analysis technique for linear regression discussed in Chapter II.  $E_a/n$  values and their experimental uncertainties are listed on Table 4.

The isothermal data were analyzed according to the procedure in described in Chapter II. Plots of  $\ln \ln(1/1-x)$  as a function of  $\ln t$  (step I - to determine  $n$  and  $\ln K$  at each isothermal temperature), and plots of  $\ln K$  as a function of  $1/T_{\text{iso}}$  (step II - to determine  $E_a$ ) are shown in Figures 37a through 37p, in Appendix C. In the  $\ln \ln(1/1-x)$  vs.  $\ln t$  plots, the data points lay on straight lines with a correlation coefficient better than 99.8 percent. This

TABLE 4. CALCULATED KINETIC PARAMETERS

Bulk Samples - Liquid Nitrogen Quenched						
Isothermal						Rate Heating
Compositions.	$E_a$ Kcal/mole	n	$K_0$	$E_a/n$ Kcal/mole(eV/Sb <sub>2</sub> S <sub>3</sub> unit)	$E_a/n$ Kcal/mole(eV/Sb <sub>2</sub> S <sub>3</sub> unit)	
As <sub>0.8</sub> Sb <sub>1.2</sub> S <sub>3</sub>	52±2	1.6±0.1	1.3x10 <sup>15</sup>	33±3	(2.4±0.2)	38±1 (2.7±0.1)
As <sub>0.6</sub> Sb <sub>1.4</sub> S <sub>3</sub>	81±6	1.7±0.2	1.5x10 <sup>27</sup>	48±8	(3.0±0.5)	38±2 (2.4±0.1)
As <sub>0.4</sub> Sb <sub>1.6</sub> S <sub>3</sub>	81±9	1.7±0.2	4.6x10 <sup>28</sup>	48±10	(2.6±0.5)	43±3 (2.3±0.1)
Sulfur Deficient Bulk Samples - Liquid Nitrogen Quenched						
As <sub>1.2</sub> Sb <sub>0.8</sub> S <sub>2.55</sub>	35±2	1.6±0.1	6.6x10 <sup>8</sup>	22±2	(2.4±0.2)	23±1 (2.5±0.1)
As <sub>1.0</sub> Sb <sub>1.0</sub> S <sub>2.67</sub>	45±2	1.5±0.1	5.3x10 <sup>12</sup>	30±3	(2.6±0.3)	32±1 (2.8±0.1)
Vapor Deposited Films						
As <sub>0.8</sub> Sb <sub>1.2</sub> S <sub>3</sub>	62±5	1.7±0.2	1.1x10 <sup>21</sup>	37±6	(2.7±0.5)	42±2 (3.1±0.1)
As <sub>0.4</sub> Sb <sub>1.6</sub> S <sub>3</sub>	187±4	3.4±0.4	4.6x10 <sup>68</sup>	55±8	(3.0±0.4)	50±1 (2.7±0.1)
Sb <sub>2</sub> S <sub>3</sub>	122±2	2.2±0.1	3.0x10 <sup>115</sup>	56±5	(2.5±0.2)	56±2 (2.4±0.1)

indicates that the data fit the JMA model very well, and neither  $n$  nor  $\ln K$  change with time during the crystallization of this material. However, these straight lines for four supposedly identical measurements were shifted parallel with respect to each other, yielding a fluctuation in the intercept,  $\ln K$ , while maintaining approximately the same slope,  $n$ . The error bars represent the amount of shift in these lines, and the data points are the average of four measurements. It has been found that the error bars would have been larger, because of the variation in sample surface area, if the specimens had been less carefully split or crushed during the sample sealing operations. Errors still existed, even with careful DSC sample preparation, probably because of internal pores and cracks in the samples where crystallization tended to initiate, as seen in Figure 27. Also, it was found that minor fluctuations in data affected  $n$  values, which in turn affected  $\ln K$  values in larger magnitudes. The errors in  $\ln K$  were amplified because the intercepts were taken by extrapolating the slope to  $\ln t = 0$ , which was far removed from the region where the data were obtained. Since temperature dependence of  $n$  values had not been detected, the average of all  $n$  values (for all temperatures) were used as the  $n$  value for the sample.  $\ln K$  was calculated from this unified slope, in order to minimize the amplification of errors. The calculated values,  $E_a$ ,  $n$ ,  $K$ ,



100um

Figure 27. Micrograph showing the internal structure around the internal

and  $E_a/n$  are listed on Table 4. The errors in determining  $E_a/n$  were calculated as before.  $n$  values appear to be about the same for all bulk samples ( $n = 1.6 \pm 0.1$ ). However, they were considerably higher for two films which were in a form of thin sheet. These high  $n$  values in films correlated with a incubation time prior to isothermal crystallization as shown in Figure 28. The following reasons have been considered to explain this phenomena; (1) the geometrical constraint in the diffusion process, (2) a delay in thermal response due to the poor thermal contact between sheets, and (3) a difference in the way arsenic and antimony atoms are arranged in films as compared to bulks. The first reasoning could be excluded since the films, which were used in this study, might be too thick ( $\sim 15\mu\text{m}$ ) to interfere with the diffusion. The third reasoning is an exciting possibility, which is correlated to the explanation that the films may be totally amorphous, while the bulk samples are most likely heterogeneous.

$E_a/n$  values obtained through two separate methods generally agreed within experimental errors. The experimental errors for the isothermal method were found to be much higher than those in the dynamic heating method, mostly because of the following reasons; (1) in the isothermal technique, data at the beginning are lost due to instrument's stabilization time, (2) the isothermal data analysis requires a two step operation, while only one

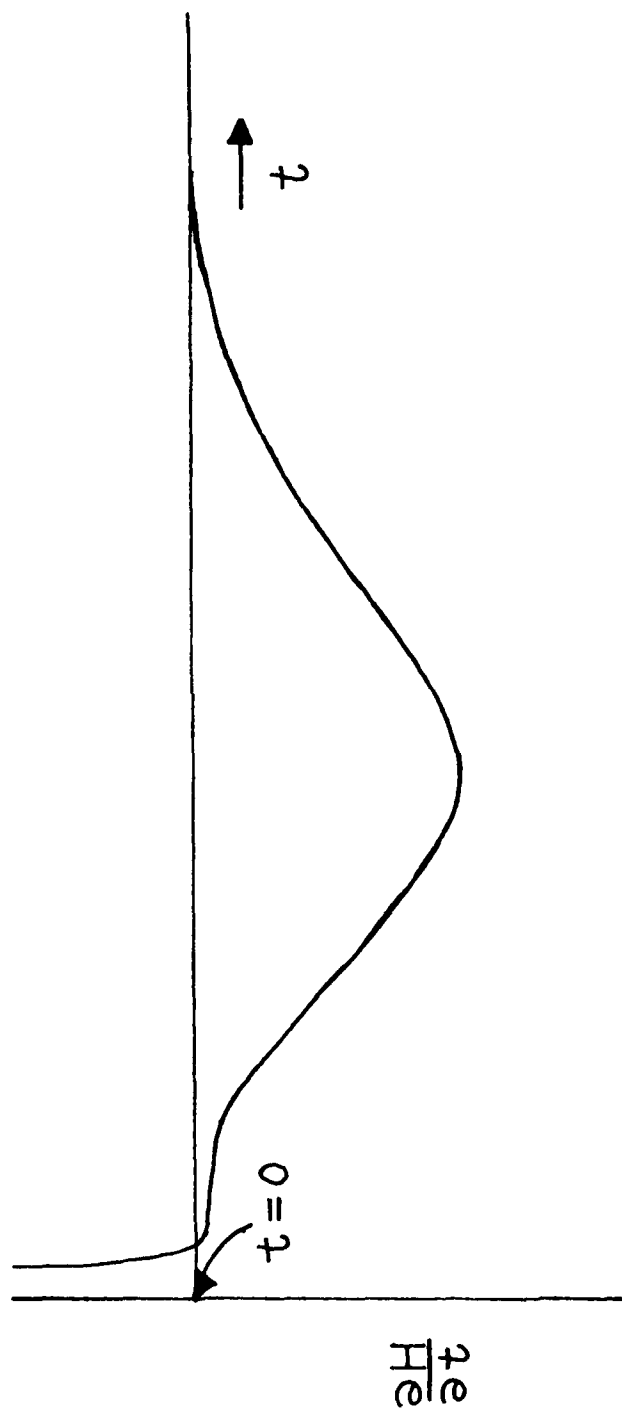


Figure 28. Isothermal Trace for Films.

calculation is needed for the dynamic heating data analysis, (3) the first calculation step for the isothermal data analysis involves an extrapolation of data which tends to exaggerate the fluctuation in data, and in addition (4) errors in  $E_a/n$  from the isothermal data are additions of errors in  $E_a$  and  $n$ .

$E_a/n$  values, obtained with either method, were found to increase in general with increasing antimony content, as the concentration of  $Sb_2S_3$  per mole of glass which contribute to the crystallization increases (See Table 4). Since  $As_2S_3$  does not contribute to the crystallization process, the  $E_a/n$  values were normalized by the corresponding mole percent of  $Sb_2S_3$  in the samples to obtain  $E_a/n$  values in units of eV per  $Sb_2S_3$  unit (shown in parenthesis). The energy required for one  $Sb_2S_3$  unit to crystallize seems to increase with increasing  $As_2S_3$  concentration in the stoichiometric specimens. Even though  $As_2S_3$  itself does not crystallize, its presence seems to increase the apparent activation energy barrier of crystallization. This is probably because antimony atoms have to diffuse through the viscous  $As_2S_3$  glass to reach the crystallizing surface prior to their crystallization, which may add the activation energy of diffusion to the total process.

The pre-exponential factors (or frequency factors),  $K_0$ , were found to increase by orders of magnitude with

increasing antimony content in bulk samples, which may correlate to an increase in the number of crystallization site per unit surface area of glass.

$E_a/n$  values for the films were about the same or slightly higher as compared to those of bulks. The most outstanding feature of the films was that the pre-exponential factors,  $K_0$ , were much higher. This may be related to the larger number of nucleation sites for the films.

### c. Activation Energy of Glass Transition

Activation energy of glass transition ( $H_a$ ) was calculated using Equation 6. The dynamic heating data for the glass transition, used in this calculation, are listed on Table 3. The calculated activation energies (in Kcal/mole) are plotted as a function of composition for various forms of samples in Figure 29.

For bulk samples, there was no significant differences in the  $H_a$  values between stoichiometric and sulfur deficient samples, and the powdered samples also showed about the same values. The activation energy increased slightly with antimony content but the variation was very small.

There was a large difference in  $H_a$  values between bulks and films. Films had much higher activation energies, indicating that they require much higher energies for the transition reactions to occur, although the glass transition temperatures were not much different between bulks and

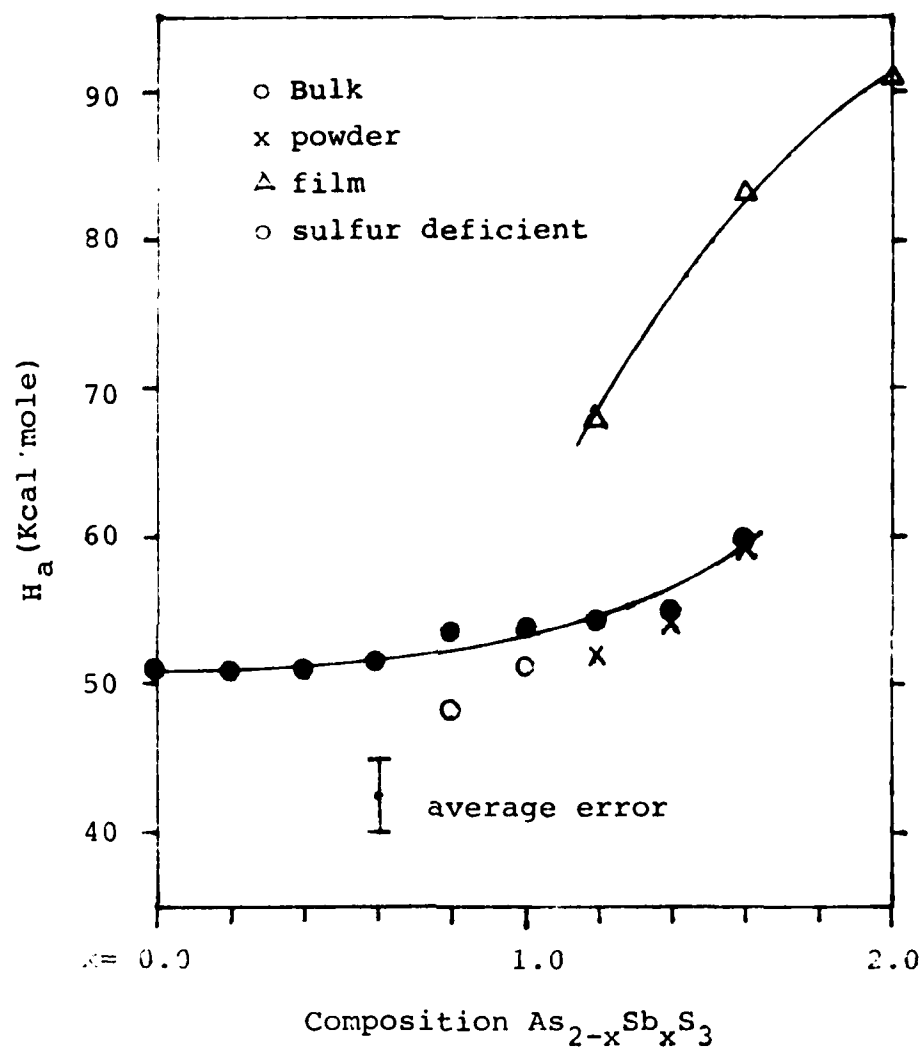


Figure 29. Activation Energy of Glass Transition,  $H_a$ , as a Function of Composition for Various Forms of Samples.

films. The activation energies for the films showed a compositional dependence which was absent in the bulk samples. This data may support the explanation that the films are totally amorphous in the as-deposited state, while the bulk samples are most likely heterogeneous.

Errors in the activation energy calculations were determined by the method discussed in Chapter II. Since the errors were about the same for all data points, only one error bar is shown in Figure 29.

#### d. Effect of Annealing on Glass Transition

This experiment was conducted to examine the possible existence of interaction between  $\text{As}_2\text{S}_3$  and  $\text{Sb}_2\text{S}_3$  in the glasses.

When a glass is annealed at temperatures below the glass transition range, the glass stabilizes in a lower energy state. Upon re-heating the glass through the glass transition temperature region in a DSC instrument, the glass transition appears as a step change associated with an endothermic peak. This is because the glass, while undergoing the glass transition, absorbs back the heat it has given up during annealing (enthalpy of relaxation), which may be assumed to be equal to the area under the endothermic peak ( $Q$  cal/mole).  $Q$  were measured as a function of annealing time ( $t$  hours), and the results were plotted in Figure 30. Curve (a) in Figure 30 represent  $\text{As}_2\text{S}_3$ , (b) is for  $\text{As}_{1.8}\text{Sb}_{0.2}\text{S}_3$ , (c) is for  $\text{As}_{1.6}\text{Sb}_{0.4}\text{S}_3$ , and

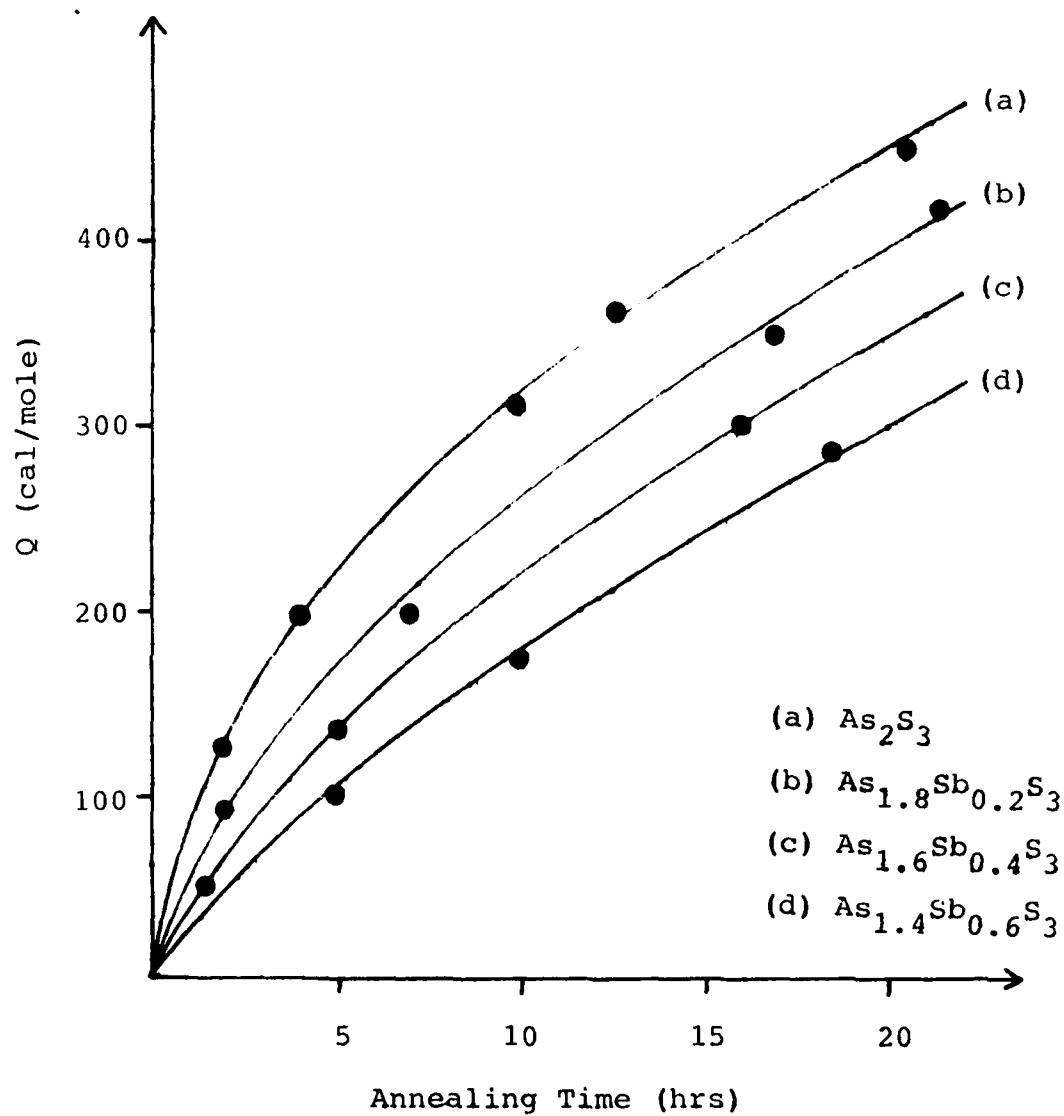


Figure 30. Area Under Tg Peak,  $Q$ , as a Function of Annealing Time for Different Compositions [Bulk Samples].

(d) is for  $\text{As}_{1.4}\text{Sb}_{0.6}\text{S}_3$ . These data showed that the energy release during annealing process (relaxation) decreased with increasing concentration of antimony in the glass. These curves were found to fit well (with correlation coefficients better than 99.7 percent) to an equation of the form;  $Q = A t^m$ . The curves could be approximated by  $Q =$ ; (a)  $87.6 t^{0.5506}$ , (b)  $59.4 t^{0.6289}$ , (c)  $36.1 t^{0.7764}$ , and (d)  $28.4 t^{0.7893}$ .

The calculation of  $Q$  for different compositions with the same annealing time, using the equations listed above, suggested that only  $\text{As}_2\text{S}_3$  relaxed, and the addition of antimony somewhat suppressed the relaxation of  $\text{As}_2\text{S}_3$ . This interpretation is consistent with the structural model of the glasses proposed by Kawamoto et al., in which the glasses consist of  $\text{As}_2\text{S}_3$  and  $\text{Sb}_2\text{S}_3$  phases, and the phases are connected with As-S-Sb bonds. According to this model, increasing amount of  $\text{Sb}_2\text{S}_3$  phase increases the number of interfacial As-S-Sb bonds which do not participate in the relaxation process.

#### e. A Self-Consistent Model of Crystallization Mechanism

The development of a model for the crystallization mechanism of the bulk  $\text{As}_{2-x}\text{Sb}_x\text{S}_3$  glasses must take into account the following; (1) An abrupt change in glass forming tendency occurred within a narrow compositional range at around  $x=1.1$ , (2) Both the glass transition temperature and activation energy of glass transition did not change

significantly with composition, (3) the enthalpy of relaxation abnormally decreased with increasing antimony concentration in the glasses, (4) only  $\text{Sb}_2\text{S}_3$  crystallized and  $\text{As}_2\text{S}_3$  remained glassy upon thermal treatment of the glasses, and no solid solution formation was detected, (5) the crystal growth started at the surface, (6) the diameter of  $\text{Sb}_2\text{S}_3$  crystals grown from melts decreased with increasing arsenic content and with faster cooling rate, and (7) the apparent activation energy to crystallize one mole of  $\text{Sb}_2\text{S}_3$  decreased with antimony addition.

These observations led to the development of a model for the crystallization mechanism, which is described as the following; (1) the glasses exhibit two phase heterogeneity consisting of  $\text{Sb}_2\text{S}_3$  phase and  $\text{As}_2\text{S}_3$  matrix phase, and there exist As-S-Sb bonds at the interface as proposed by Kawamoto et al. [Ref.5 and 6], (2) the nucleation sites are at the surface of the bulk in the  $\text{Sb}_2\text{S}_3$  phase, and (3)  $\text{Sb}_2\text{S}_3$  crystals grow in the glassy  $\text{As}_2\text{S}_3$  matrix by diffusion of antimony atoms through  $\text{As}_2\text{S}_3$  phase, and subsequent interconnection of  $\text{Sb}_2\text{S}_3$  phase.

According to this model, antimony rich compositions crystallized easily because very little antimony diffusion through the matrix phase was required for the growth of  $\text{Sb}_2\text{S}_3$  phase. The crystallization which had been nucleated at the surface proceeded inward as shown in Figure 31(a). On the contrary, arsenic rich compositions did not

crystallize even with a prolonged thermal treatment, because  $\text{Sb}_2\text{S}_3$  phase was isolated from each other and antimony atoms had to diffuse for considerable distances between them in order for the  $\text{Sb}_2\text{S}_3$  phase to grow. Therefore, the crystallization, which had been nucleated at the surface, could not easily propagate inward, as shown in Figure 31(b).

This model also explains the observation by Platakis et al. [Ref.11 and 12] for  $\text{As}_{2-x}\text{Sb}_x\text{Se}_3$  system, in which both  $\text{As}_2\text{Se}_3$  and  $\text{Sb}_2\text{Se}_3$  crystallizes, that the compositions with high arsenic content crystallized in monoclinic structure, antimony rich compositions crystallized in orthorhombic structure, and intermediate compositions exhibited both structures.

The aspect of diffusion limited crystal growth was further supported by the observations (6) and (7). The surface nucleation was directly observed by microscopy, and also examined by comparing the difference in crystallization kinetics of samples with different surface areas. The existence of As-S-Sb bonds at the interface of  $\text{As}_2\text{S}_3$  and  $\text{Sb}_2\text{S}_3$  phases was consistent with the observation (3). The abnormal decrease in the enthalpy of relaxation with antimony addition may be conveniently explained if both the glassy  $\text{Sb}_2\text{S}_3$  phase and the interfacial As-S-Sb bonds do not relax with annealing.

The as-deposited glassy state in the films most likely does not exhibit two phase structure, and the

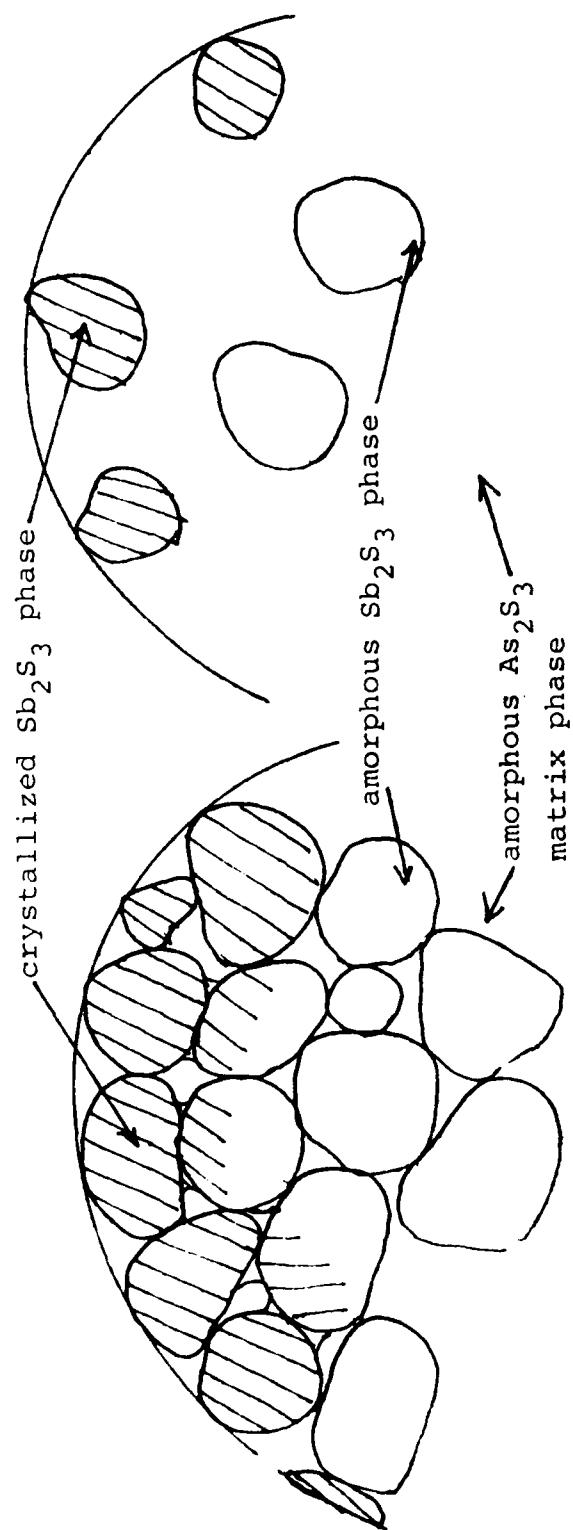


Figure 31a. Model of Crystallization Mechanism, Antimony Rich Compositions

Figure 31b. Model of Crystallization Mechanism, Arsenic Rich Compositions

crystallization mechanism of the films is probably different from this proposed model, because of the following observation; (1) the direct examination of the films with TEM showed that the films were totally amorphous and featureless, (2) the activation energy of glass transition showed a compositional dependence, (3) and the order parameter and activation energy of crystallization were much higher in the films as compared to the bulks.

#### IV. SUMMARY

The crystallization mechanism of  $\text{As}_{2-x}\text{Sb}_x\text{S}_3$  glasses in a melt quenched bulk form and a thin film form was examined and a self-consistent model of the crystallization mechanism was developed. The summary of experimental results and interpretations which aided the understanding of the mechanism were as the following.

##### GLASSY STATE

The direct observations of the bulk glasses using SEM revealed a network-like two phase submicrostructure caused by a differential etching. This structure and the relative amount of phases present were found to be independent of composition, indicating that the submicro-structure did not support the two phase glass structure consisting of  $\text{As}_2\text{S}_3$  and  $\text{Sb}_2\text{S}_3$  regions as proposed by Kawamoto et al. [Ref.5 and 6]. It was concluded, instead, that this structure reflected the cluster or long range order known to exist in glasses.

The microscopic study of the vapor deposited films, using TEM, did not identify any features. The as-deposited films seemed totally amorphous and featureless, whether the film was a thin film which was directly vapor deposited on a thin carbon film substrate, or a thick film which was thinned by ion-milling or by microtome technique.

The activation energy of glass transition for bulk glasses exhibited little dependence on composition. This, in general, indicates that the glass consists of two phases, and the compositional variation does not affect the nature of the atomic bondings. On the contrary, the activation energy for the film samples showed a strong compositional dependence, suggesting the absence of such two phase structure in films.

An abrupt change in glass forming tendency occurred within a narrow compositional range at around  $x=1.1$  for the bulk  $\text{As}_{2-x}\text{Sb}_x\text{S}_3$  samples. The antimony rich compositions readily crystallized during the DSC experiments, while the arsenic rich compositions did not crystallized even with a prolonged thermal treatment. This phenomena was successfully explained by the model of crystallization mechanism, describing the diffusion limited crystal growth in the two phase glass structure.

#### CRYSTALLIZED STATE

X-ray diffraction analysis showed that only the  $\text{Sb}_2\text{S}_3$  phase crystallized in the glassy  $\text{As}_2\text{S}_3$  matrix phase. No solid solution formation between  $\text{Sb}_2\text{S}_3$  and  $\text{As}_2\text{S}_3$  was detected within the experimental error. The phase diagram of  $\text{As}_2\text{S}_3$ - $\text{Sb}_2\text{S}_3$  system in the antimony rich region was confirmed to be totally immiscible. The phase diagram of the arsenic rich region could not be obtained because the compositions did not stabilize within the experimental time

scale of this study.

#### CRYSTALLIZATION PROCESS

The optical micrographs of the partially crystallized bulk glass specimens revealed that the crystallization initiated at the outer surface and around the internal pores in the glass. The number of nucleation site, represented by the frequency factor ( $K_0$ ), increased with antimony content because a large number of  $Sb_2S_3$  phase was exposed on the surface.

It was suggested that the crystallization process was diffusion limited because the diameter of the melts grown  $Sb_2S_3$  crystal decreased with the antimony content, and also with the faster cooling rate. Another observation supporting this proposal was that the apparent activation energy, which was a combination of the diffusion energy and the crystallization activation energy, increased with arsenic content.

#### OTHER RESULTS

The difference in crystallization kinetics between the film and the bulk was found to be caused by the difference in their surface area. The films crystallized faster because of their larger surface area. This result correlated with the  $K_0$  values, which were orders of magnitude higher in films. In addition, the film samples exhibited an incubation time prior to isothermal

crystallization, which correlated with the larger order parameter( $n$ ) and apparent activation energy of crystallization( $E_a$ ). This result may suggest that the crystallization mechanism is somewhat different in the films because the initial glassy state is totally amorphous with no heterogeneity.

The sulfur deficient specimens crystallized readily, even in the compositional range where the stoichiometric bulk samples did not crystallize. Though the frequency factor ( $K_0$ ), which reflects the number of crystallization site on the surface, decreased with arsenic content, the composition crystallized faster because of the lowered apparent activation energy. The examination of the glassy specimens with EDXA and X-ray diffraction technique identified a large amorphous AsS phase (size of the phase seemed to depend on the degree of sulfur deficiency). The lowered apparent activation energy may reflect the crystallization of AsS, which aid the crystallization of  $Sb_2S_3$  phase.

## V. FUTURE WORK

Continuation of the TEM study on the bulk  $\text{As}_{2-x}\text{Sb}_x\text{S}_3$  glasses is recommended for a future work. Preliminary calculation on the differential scattered electron intensity have shown that the glasses, if they consist of the  $\text{Sb}_2\text{S}_3$  and  $\text{As}_2\text{S}_3$  phases as proposed, should produce a detectable image contrast in the TEM photograph. Among the available techniques, microtome was found to be the most promising in preparing the chalcogenide glasses for the TEM examination, and this technique should be further refined in future to yield more reproducible results.

## APPENDIX A

### THERMAL ANALYSIS

Changes in physical and chemical state of a material are generally accompanied by either a heat absorption from environment (endothermic reaction) or a heat generation (exothermic reaction). Such changes may be induced by heating or cooling of the material. Among the physical changes, the first order phase transitions involve breaking of atomic bonds, while the second order phase transitions involve mere atomic realignments. Melting and polymorphic transformations are the first order phase transitions and are endothermic upon heating and exothermic upon cooling, because the material reversibly changes between a lower energy state at lower temperature and a more disordered higher energy state at higher temperature. On the other hand, crystallization, which is also a first order transition, is always irreversibly exothermic either upon heating from the glassy state or cooling from the super cooled liquid state because the crystalline state has the ~~lowest~~ energy. A glass transition is the second order transformation in amorphous materials involving a reversible transition between the glassy state at lower temperature and the super cooled liquid state at higher temperature.

The differential Thermal Analyzer (DTA) and the Differential Scanning Calorimeter (DSC) are thermal analysis

instruments to detect minute changes in thermodynamical variables with various physical and chemical transformations of materials. In these instruments, a sample and an inert reference material are heated in an identical thermal environment, and their difference in thermal response is recorded as a function of time. In DTA instruments, the sample and the reference are heated together with a single heater, and their temperature difference is measured; while in DSC instruments, the sample and the reference are each provided with individual heaters, and the differential heat input ( $dH/dt$ ) required to maintain their temperatures identical is recorded as a vertical axis of the data output. Therefore, the areas under endothermic or exothermic peaks are directly equal to enthalpy of the phase transformation.

From a thermodynamical relation;  $H = m \cdot C_p \cdot T$ , the vertical axis in the DSC data ( $dH/dt$ ) is directly proportional to the specific heat of the sample material ( $C_p$ ), in case of the dynamic heating experiment, as;

$$\frac{dH}{dt} = m \cdot C_p \cdot \frac{dT}{dt} \quad (A1)$$

where  $m$  is the sample weight and  $dT/dt$  is equal to the heating rate.

The same instrument may be used under the isothermal condition at temperature,  $T_{iso}$ , in which case the area under the DSC trace is also directly equal to  $H$  as ;

$$\frac{dH}{dt} = m \cdot C_p \cdot T_{iso} \quad (A2)$$

## APPENDIX B

### EFFECT OF DEPOSITION RATE ON PHYSICAL AND STRUCTURAL PROPERTIES OF $\text{As}_2\text{S}_3$ FILM

In general, the physical and structural properties of vapor deposited films are greatly different from those of the corresponding bulks and are affected by the deposition conditions such as the deposition rate, the residual gas pressure, the type and temperature of substrates, and the angle and velocity of incident vapor [Ref.53-58]. However, in spite of the emerging interest in thin film  $\text{As}_2\text{S}_3$ , most of the studies on arsenic sulfide glasses have been concerned with the bulk properties, and relatively little is known about the physical and structural properties of these glasses in a thin film form.

Apling and Leadbetter et al. [Ref.59-61] investigated the structural dissimilarity between bulk and thin film of  $\text{As}_2\text{S}_3$  and  $\text{As}_2\text{Se}_3$ , using a hot stage X-ray diffraction technique. The first diffraction peaks for both compounds were found to be sharper and more intense in as-deposited films, reflecting an enhanced longer range order, and their intensities decreased and approached that of the bulk upon annealing. This was explained by a possible existence of As-As bonds and sheet-like open structure in as-deposited films. This speculation was supported by an arsenic rich stoichiometry in their films, and a considerable

fragmentation of  $\text{As}_2\text{S}_3$  into  $\text{S}_2$  and  $\text{As}_4\text{S}_4$  during the evaporation process as detected by a mass spectroscopic technique [Ref.60 and 62]. Nemanich et al. [Ref.63 and 64] from their EXAFS and Raman spectroscopic results, and Tohge et al. [Ref.65] through an IR spectroscopy suggested that all of the As-As bonds may be incorporated as  $\text{S}_2\text{As-AsS}_2$  units like in  $\text{As}_4\text{S}_4$  molecules reflecting the structure of the dominant vapor species during the deposition process, and that As-As and S-S bonds were converted to As-S bonds upon annealing. A neutron diffraction study [Ref.66] likewise has shown that a  $\text{As}_4\text{S}_4$  (realgar type) molecule and sulfur dominate in as-deposited films.

In all studies on arsenic chalcogenide films described above, however, the investigators have deposited their films at fairly high deposition rates ranging from  $300\text{\AA}/\text{sec}$  up to  $1700\text{\AA}/\text{sec}$ . The literature describing the properties and structure of the films deposited at lower deposition rates or systematic studies on the effect of deposition rate have not been found for arsenic chalcogenide films. Since  $\text{As}_2\text{S}_3$  is reported to fractionate into  $\text{As}_4\text{S}_4$  and sulfur during the deposition process, the deposition rate, if it is varied by changing the source temperature, may affect the relative amount of the fractionated species, which may in turn affect the film properties. Therefore, a study was conducted to elucidate the effect of deposition rate on physical and structural properties of  $\text{As}_2\text{S}_3$  glass films.

The effect of deposition rate (in the range of  $15\text{\AA}/\text{sec}$  to  $300\text{\AA}/\text{sec}$ ) on the film stoichiometry, X-ray diffraction pattern, and DSC trace was studied.

The glass films were synthesized by evaporating arsenic trisulfide (Servofrax<sup>®</sup> glass) from a resistance heated tungsten boat as described in Chapter II. The deposition rates ranged from  $15\text{\AA}/\text{sec}$  to  $300\text{\AA}/\text{sec}$ , and they were varied by changing the boat (source) temperature. Figure 32 shows the deposition rate as a function of source temperature, though this calibration curve is valid only for this particular set of study while the experimental condition was kept the same.

The sulfur stoichiometry of the films was examined by energy dispersive X-ray analysis (EDXA), and was found to decrease (up to 5 percent) with increasing deposition rate, as shown in Figure 33. This may be because only a portion of  $\text{As}_2\text{S}_3$  fractionates to  $\text{As}_2\text{S}_2$  and sulfur, and the amount of fractionation increases with increase in source temperature. Some of the molecules never reach the substrate, which is situated above the boat and the vacuum pumping port, and are pumped out of the vacuum chamber since they lose their upward momentum through collisions with each other near the evaporating surface. More free sulfur would be pumped out because of its lighter weight, causing a sulfur deficiency of the films.

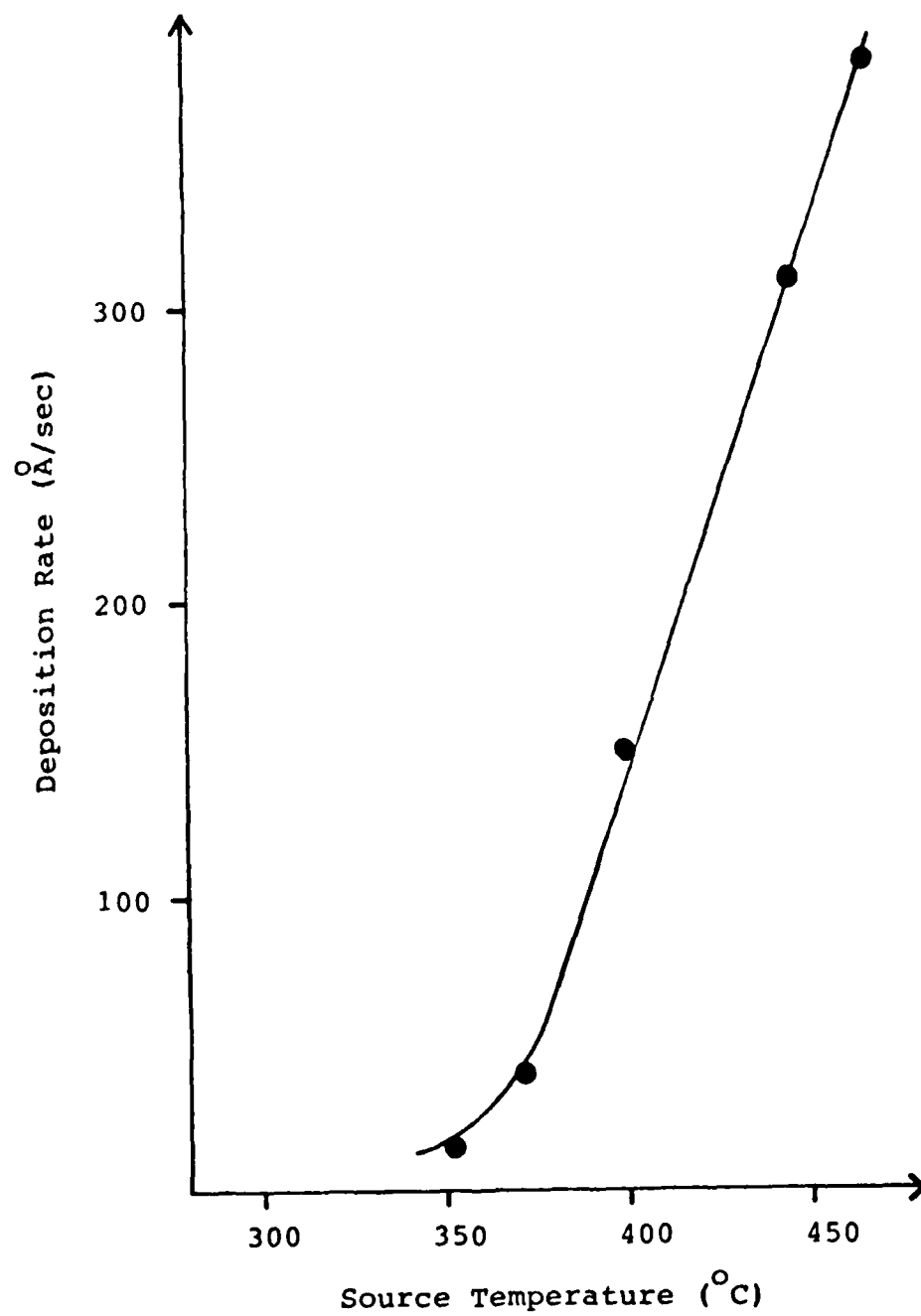


Figure 32. Deposition Rate as a Function of Source Temperature.

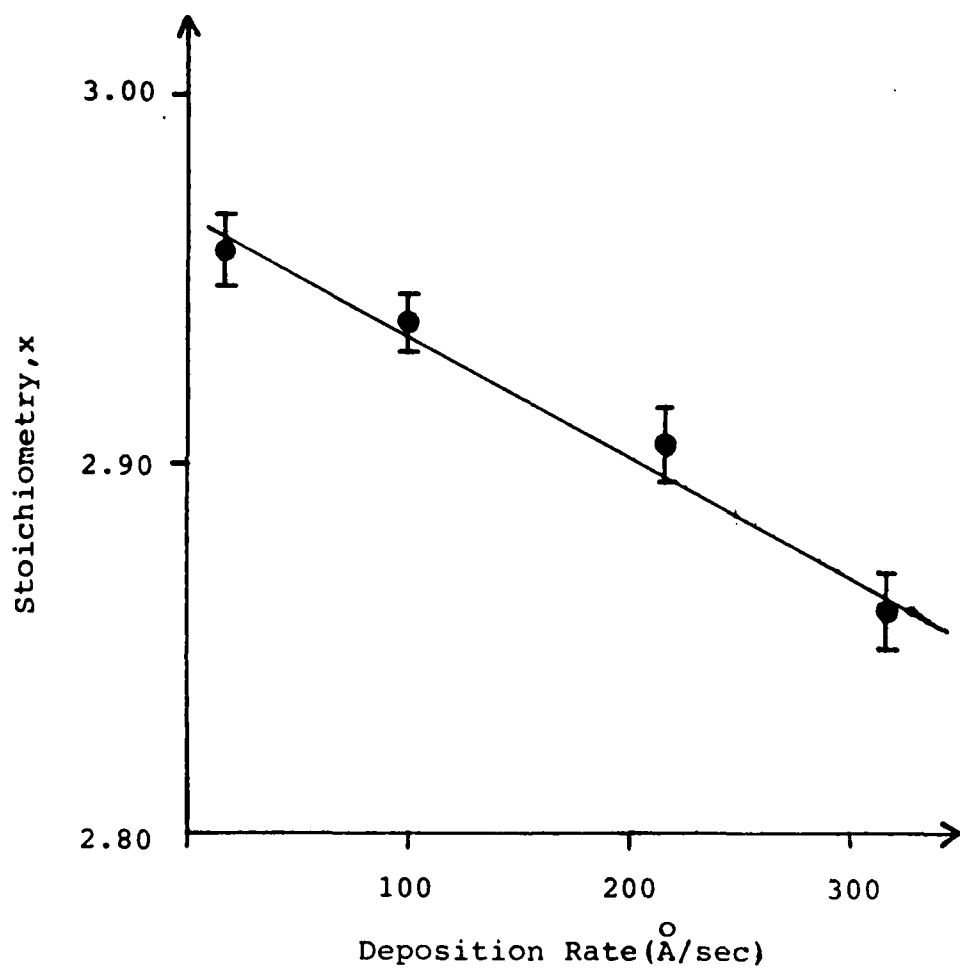


Figure 33. Sulfur Stoichiometry,  $x$ , as a Function of Film Deposition Rate in  $\text{As}_2\text{S}_x$  Films [Ref.67].

Figure 34 shows the DSC traces of films deposited at different deposition rates; trace(a) is for  $310\text{\AA}/\text{sec}$ , trace(b) is for  $200\text{\AA}/\text{sec}$ , and trace(c) is for  $15\text{\AA}/\text{sec}$ , and trace(d) for a bulk Servofrax<sup>®</sup> glass is also shown for a comparison. The DSC traces for higher deposition rates exhibited endothermic peaks at around  $580^\circ\text{K}$ , which are quite similar to the ones for sulfur deficient bulk specimens, shown in Figures 18 and 19. These peaks are probably due to the meltings of  $\text{As}_2\text{S}_2$  and adjacent compositions in  $\text{As}_2\text{S}_3$ - $\text{As}_2\text{S}_2$  system as seen from Figure 20 [Ref.49]. These peaks in the DSC trace were not present either in a slowly deposited film or in a stoichiometric bulk specimen. This indicates that only a insignificant amount of  $\text{As}_2\text{S}_2$  is present in crystalline form in a slowly deposited film.

Figure 35 shows the X-ray diffraction patterns for films deposited at different deposition rates; spectrum(a) is for an as-deposited film deposited at  $310\text{\AA}/\text{sec}$ , spectrum(b) is for the same film after being annealed at  $423^\circ\text{K}$  for 7.5 hours, and spectrum(c) is for  $15\text{\AA}/\text{sec}$ . Spectrum(d) for a Servofrax<sup>®</sup> glass is also shown for a comparison. The film deposited at a high rate showed small peaks corresponding to lattice spacings of  $5.8\text{\AA}$ ,  $3.0\text{\AA}$ , and  $2.9\text{\AA}$  ( $\text{AsS}-\beta$  high temperature phase in crystalline form) which were absent both in a slowly deposited film and in a bulk specimen. The centers of diffuse peaks for vapor deposited films were at  $5.4\text{\AA}$  and  $3.1\text{\AA}$ , correlating closely

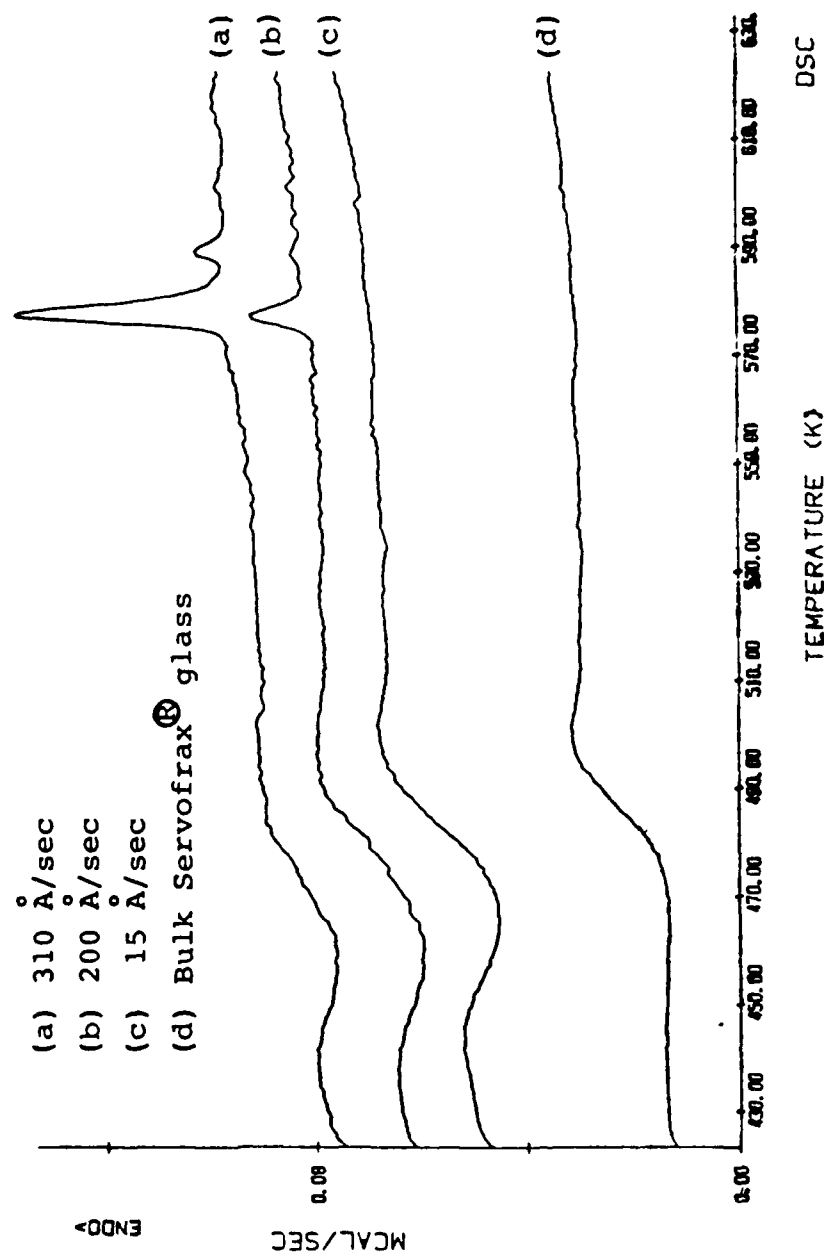


Figure 34. DSC Traces for Films and a Bulk Arsenic Sulfide.

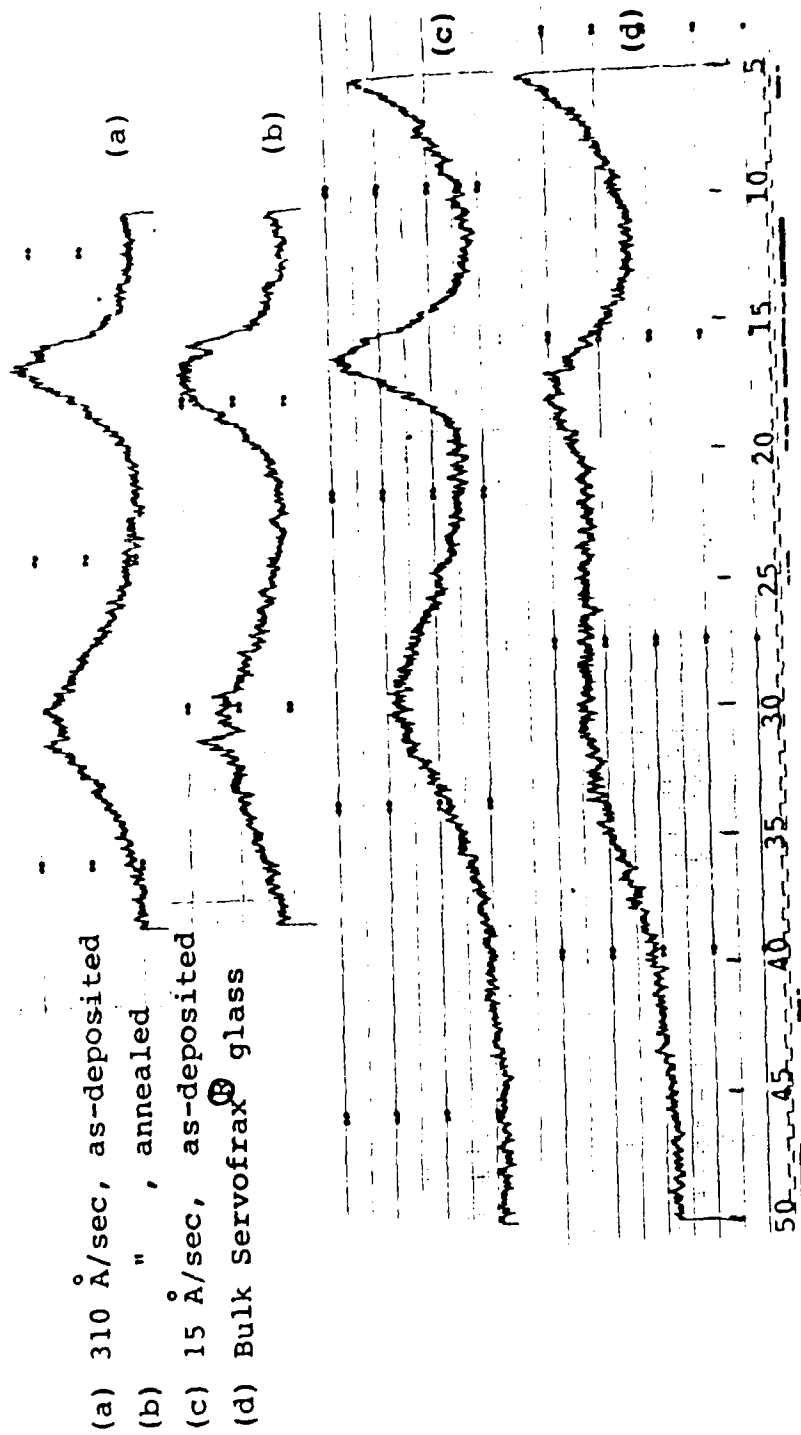


Figure 35. X-Ray Diffraction Patterns for Films and a Bulk Arsenic Sulfide.

to AsS- $\alpha$  crystalline peaks, while the first peak was centered at  $5.1\overset{\circ}{\text{\AA}}$  for the bulk sample. The peaks were much sharper and more intense in as-deposited films compared to the bulk. It is possible that the more intense peaks corresponding to AsS- $\alpha$  is superimposed on the less intense As<sub>2</sub>S<sub>3</sub> peaks. The first peak was observed to broaden and shifted toward shorter bond length upon annealing, as has been reported by Applling et al.

As a summary of this study; (1) sulfur stoichiometry of the films was found to decrease as the deposition rate increases, (2) vapor deposited films have a large population of amorphous AsS- $\alpha$ , most likely in addition to amorphous As<sub>2</sub>S<sub>3</sub>, and (3) at the high deposition rate, the films incorporate also the high temperature modification AsS- $\beta$  in crystalline form.

APPENDIX C  
CRYSTALLIZATION KINETICS DATA

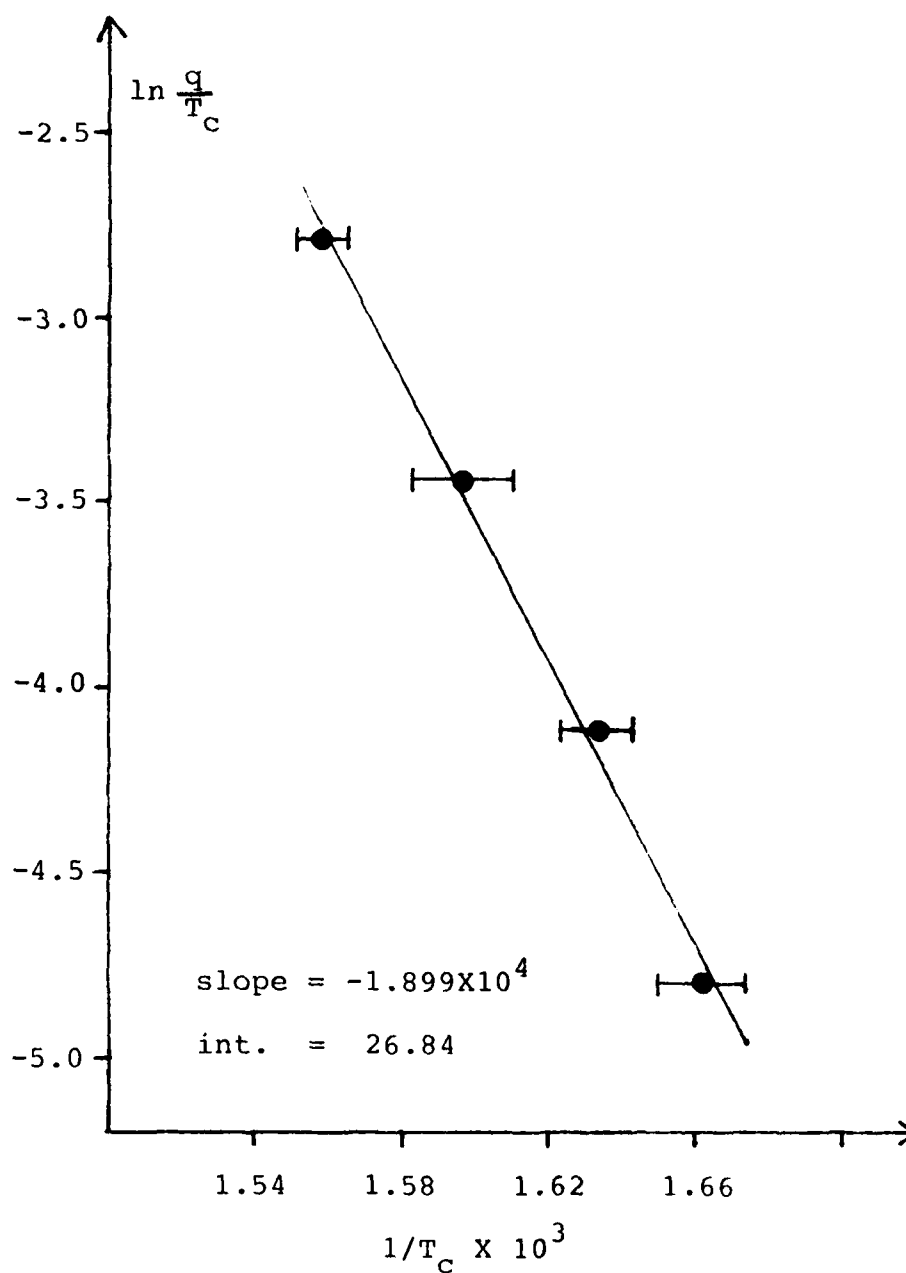


Figure 36a. Dynamic Heating Crystallization Data for Activation Energy Calculation ( $\text{As}_{0.8}\text{Sb}_{1.2}\text{S}_3$  Bulk).

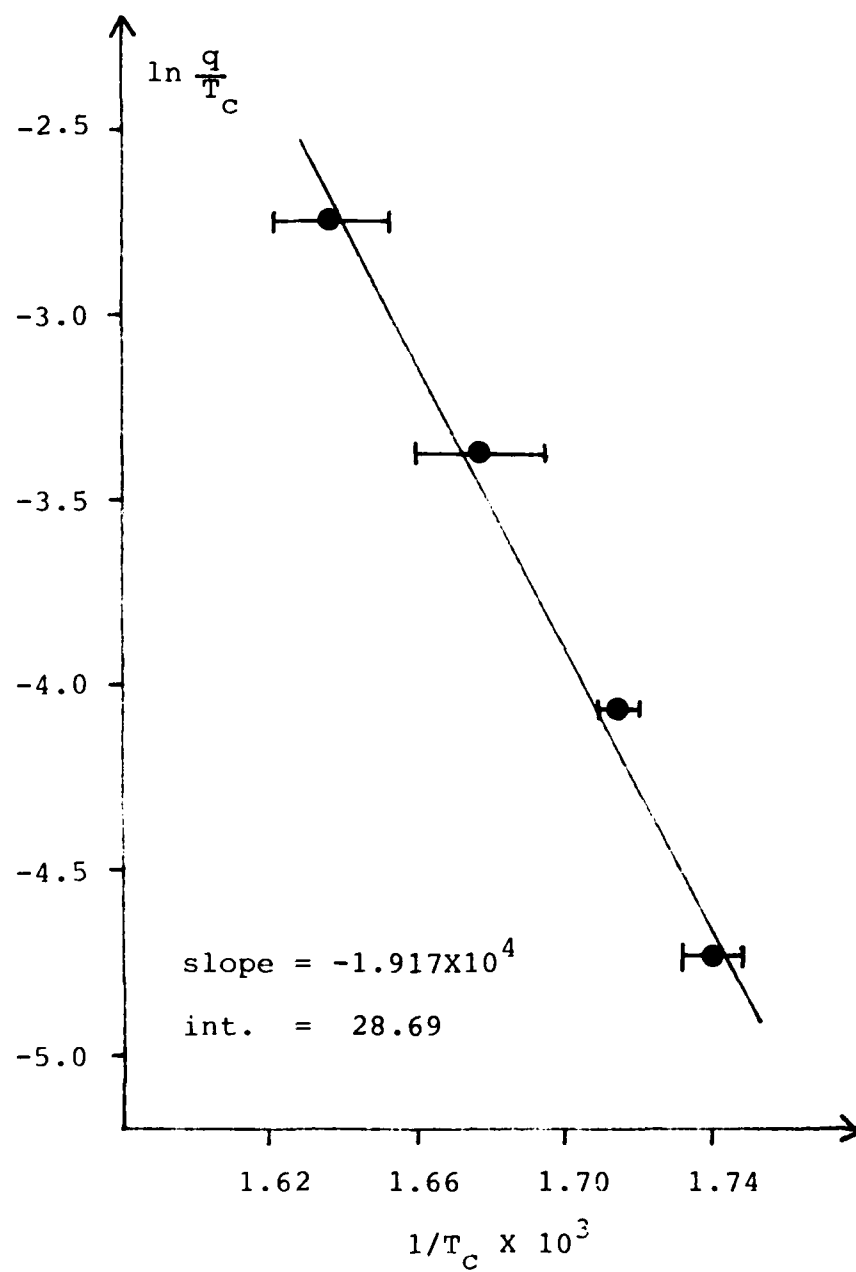


Figure 36b. Dynamic Heating Crystallization Data for Activation Energy Calculation ( $\text{As}_{0.6}\text{Sb}_{1.4}\text{S}_3$  Bulk).

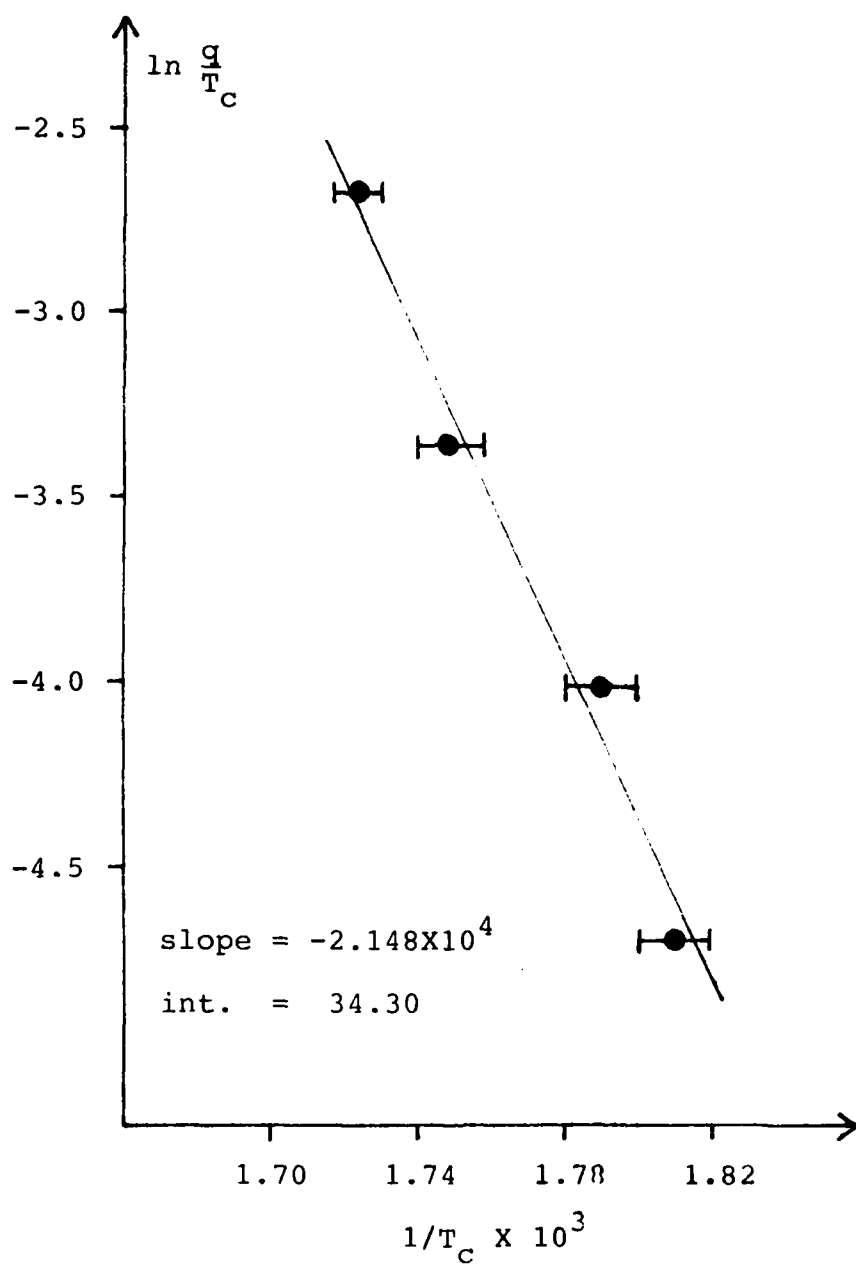


Figure 36c. Dynamic Heating Crystallization Data for Activation Energy Calculation ( $\text{As}_{0.4}\text{Sb}_{1.6}\text{S}_3$  Bulk).

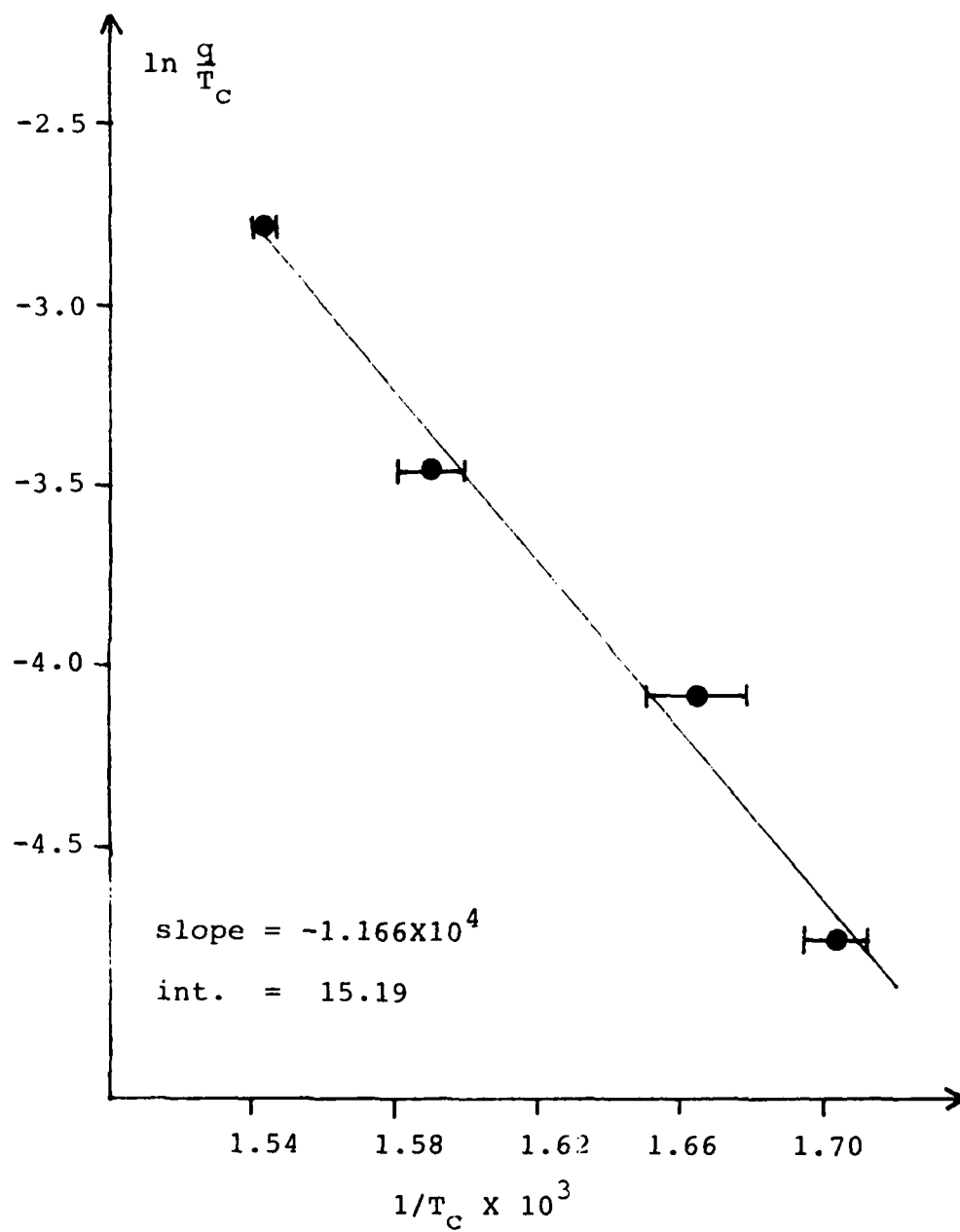


Figure 36d. Dynamic Heating Crystallization Data for Activation Energy Calculation ( $\text{As}_{1.2}\text{Sb}_{0.8}\text{S}_{2.55}$  Bulk).

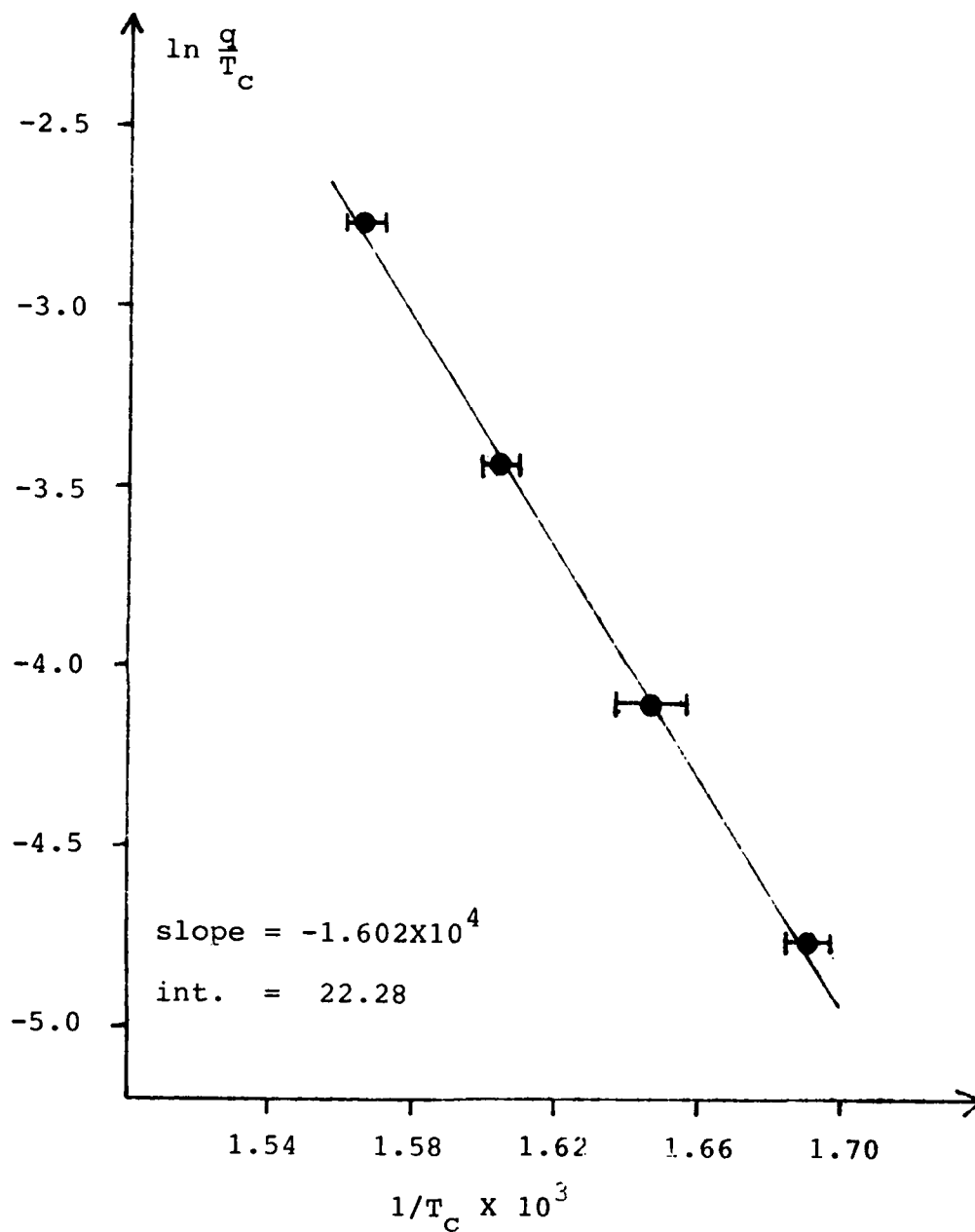


Figure 36e. Dynamic Heating Crystallization Data for Activation Energy Calculation ( $\text{As}_{1.0}\text{Sb}_{1.0}\text{S}_{2.67}$  Bulk).

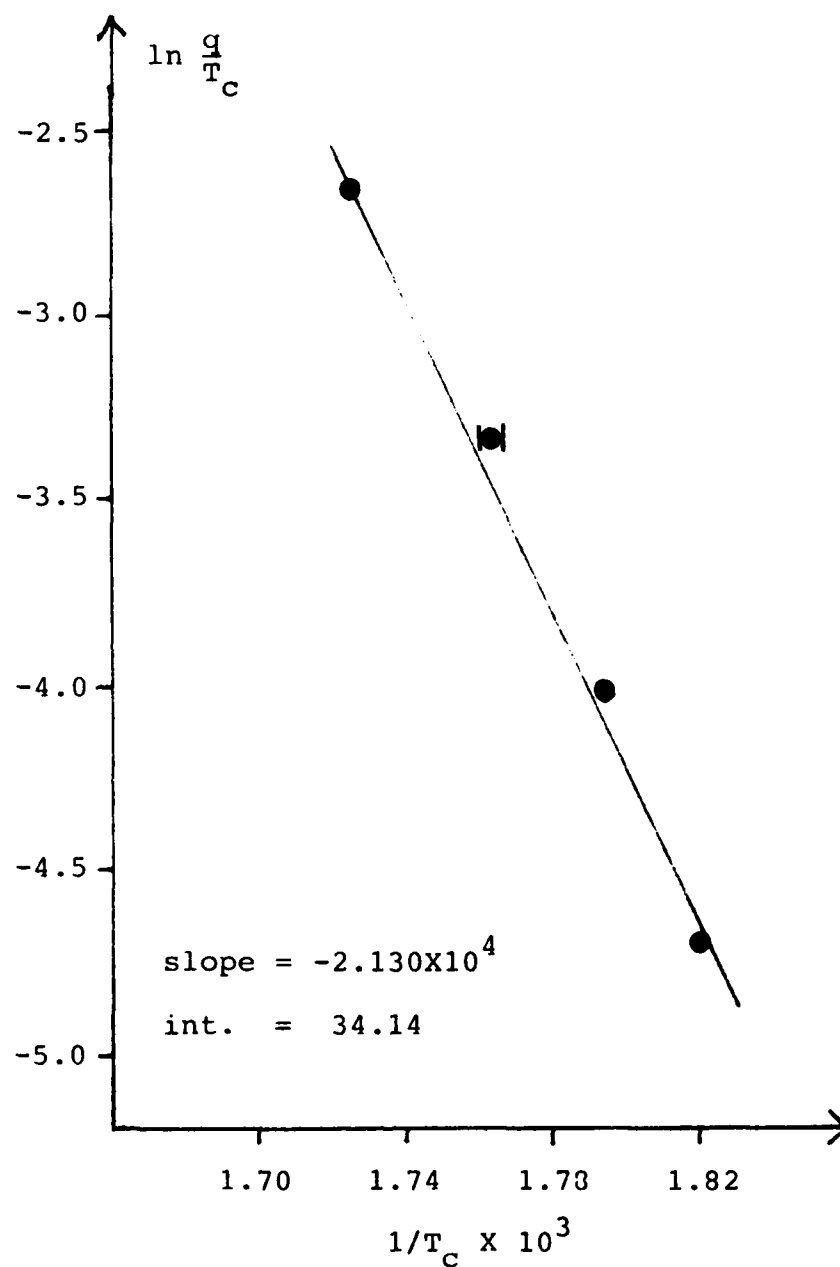


Figure 36f. Dynamic Heating Crystallization Data for Activation Energy Calculation ( $\text{As}_{0.8}\text{Sb}_{1.2}\text{S}_3$  Film).

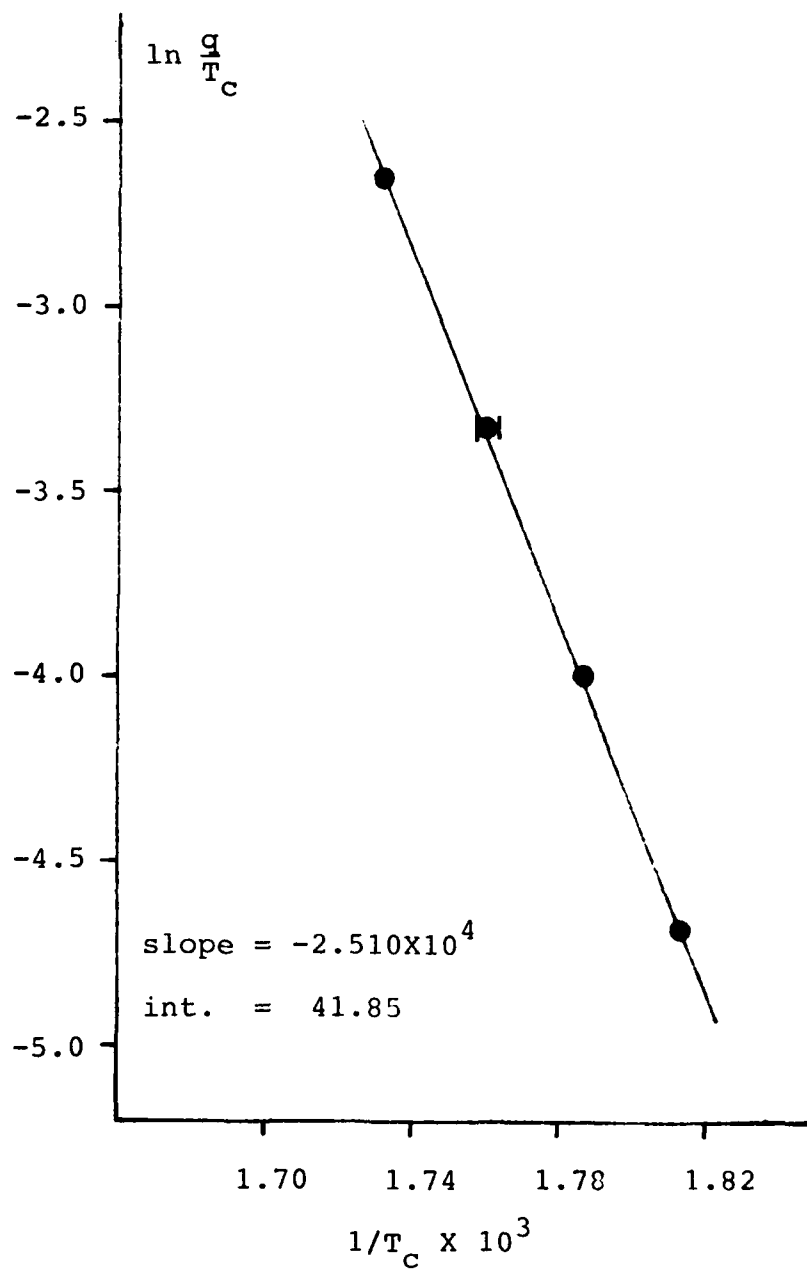


Figure 36g. Dynamic Heating Crystallization Data for Activation Energy Calculation ( $\text{As}_{0.4}\text{Sb}_{1.6}\text{S}_3$  Film).

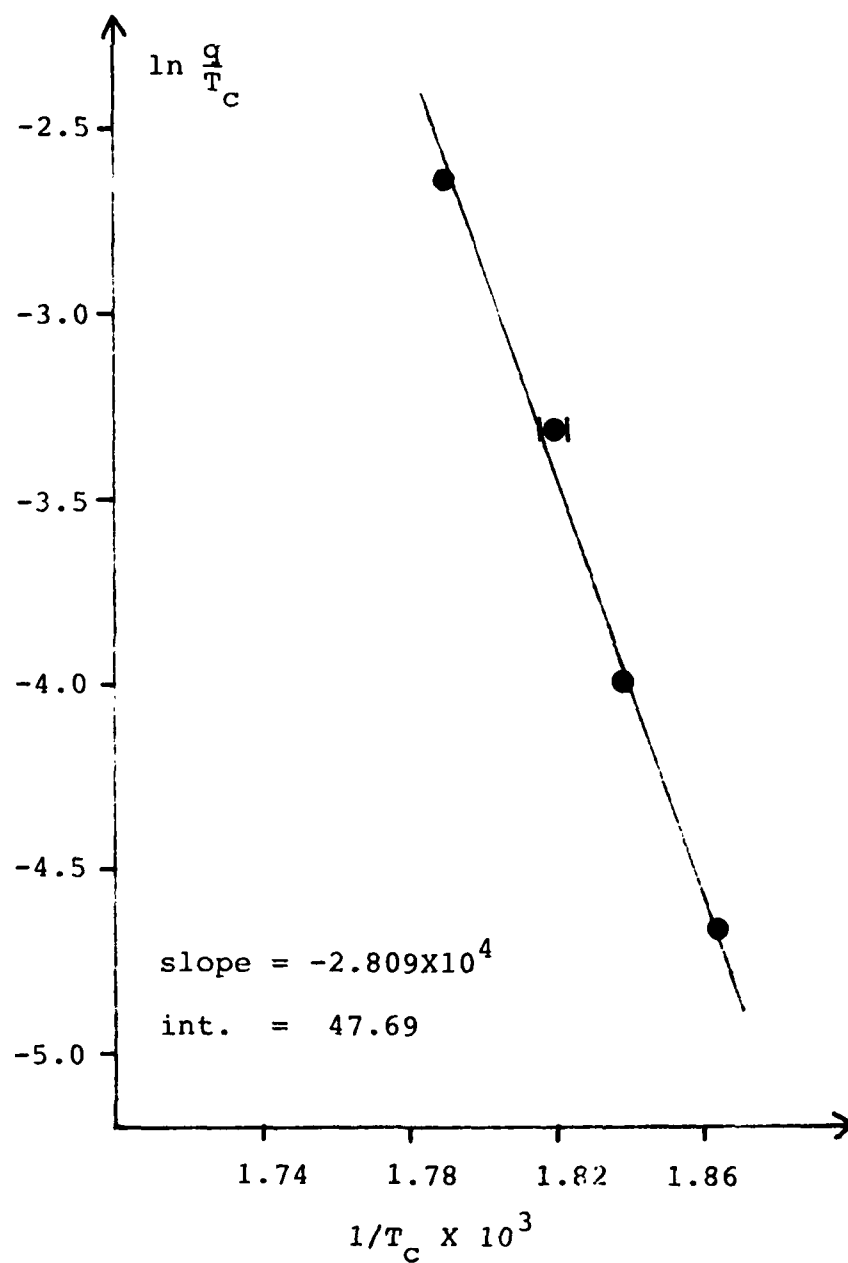


Figure 36h. Dynamic Heating Crystallization Data for Activation Energy Calculation ( $\text{Sb}_2\text{S}_3$  Film).

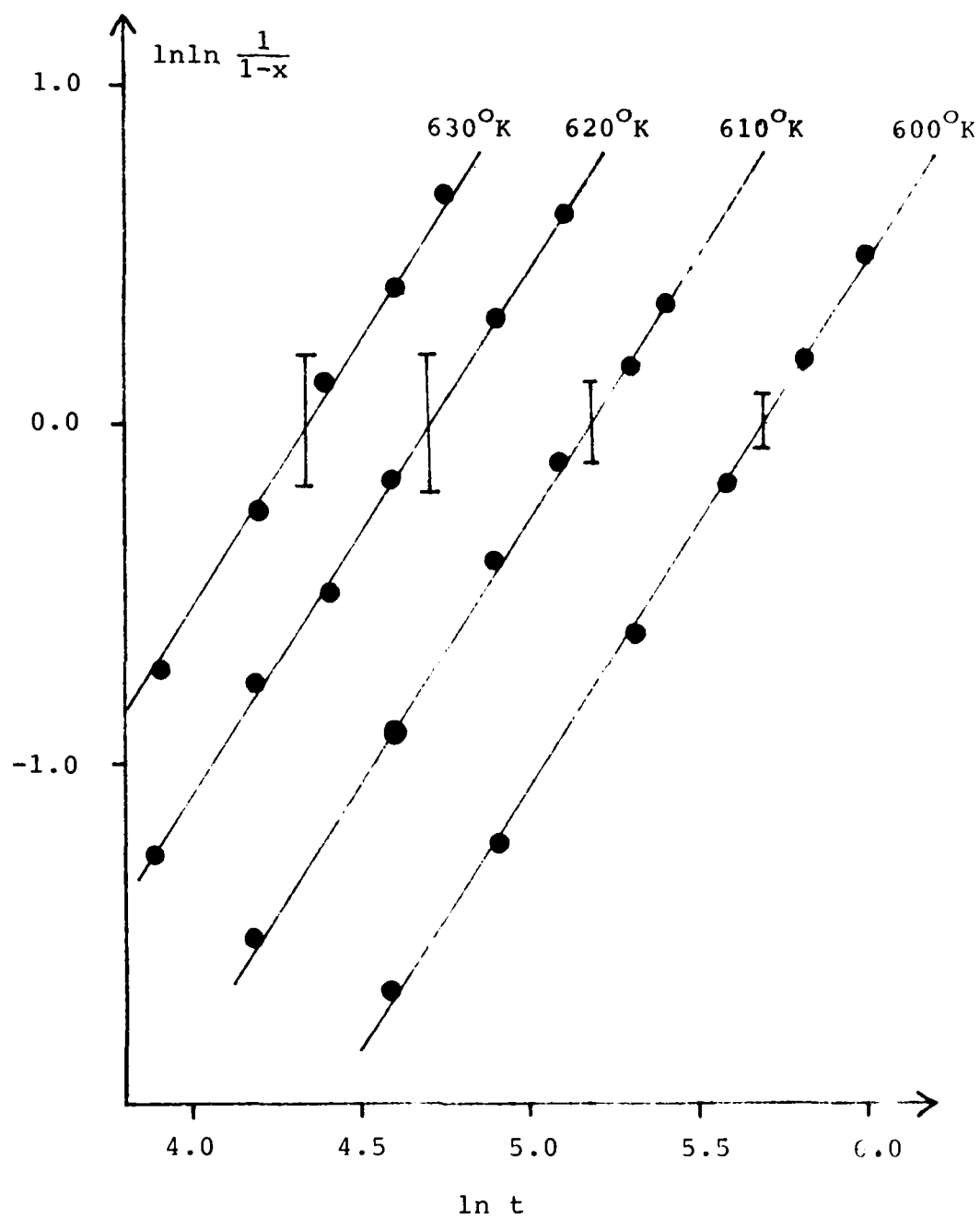


Figure 37a. Isothermal Crystallization Data for Activation Energy Calculation Step I ( $\text{As}_{0.8}\text{Sb}_{1.2}\text{S}_3$  Bulk).

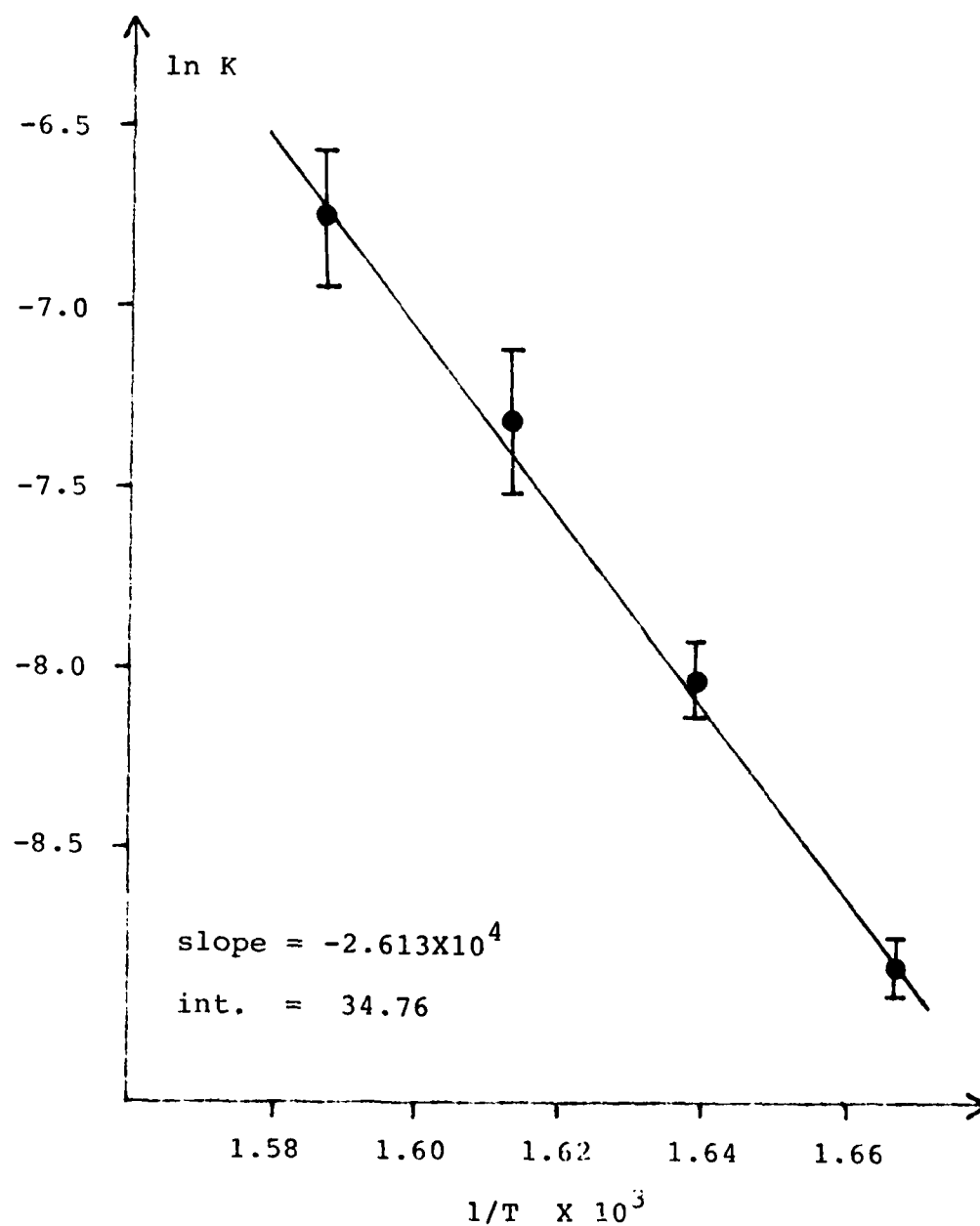


Figure 37b. Isothermal Crystallization Data for Activation Energy Calculation Step II ( $\text{As}_{0.8}\text{Sb}_{1.2}\text{S}_3$  Bulk).

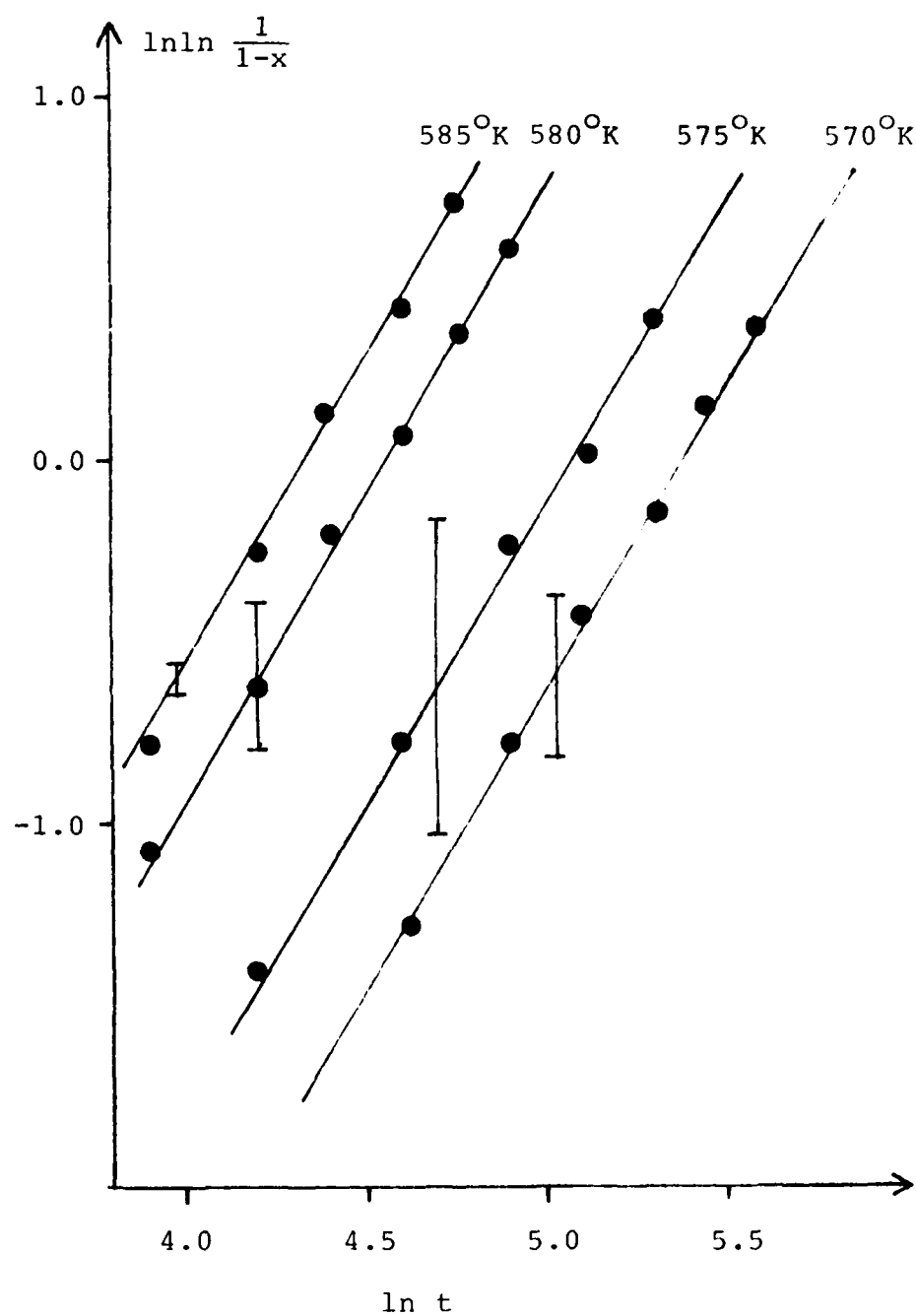


Figure 37c. Isothermal Crystallization Data for Activation Energy Calculation Step I ( $\text{As}_{0.6}\text{Sb}_{1.4}\text{S}_3$  Bulk).

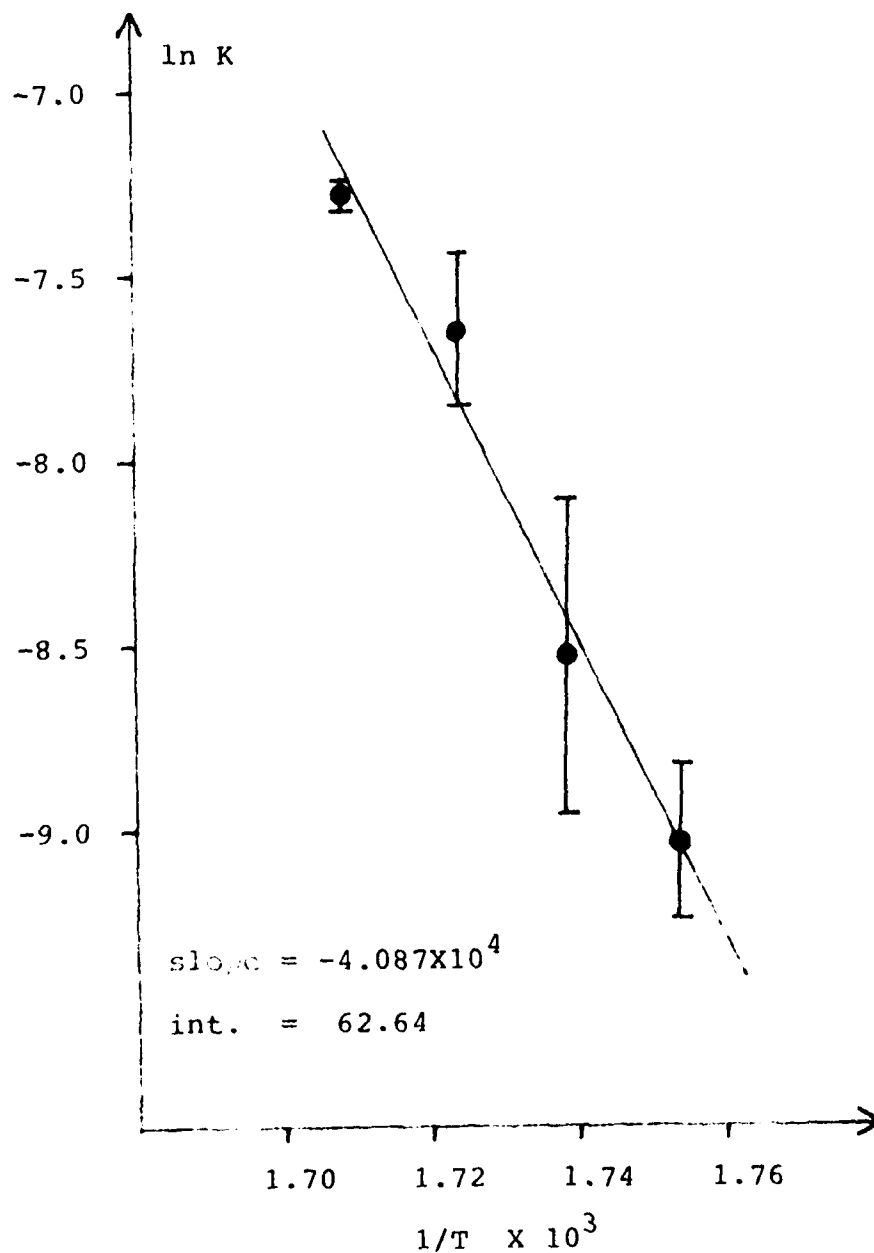


Figure 37d. Isothermal Crystallization Data for Activation Energy Calculation Step II ( $\text{As}_{0.6}\text{Sb}_{1.4}\text{S}_3$  Bulk).

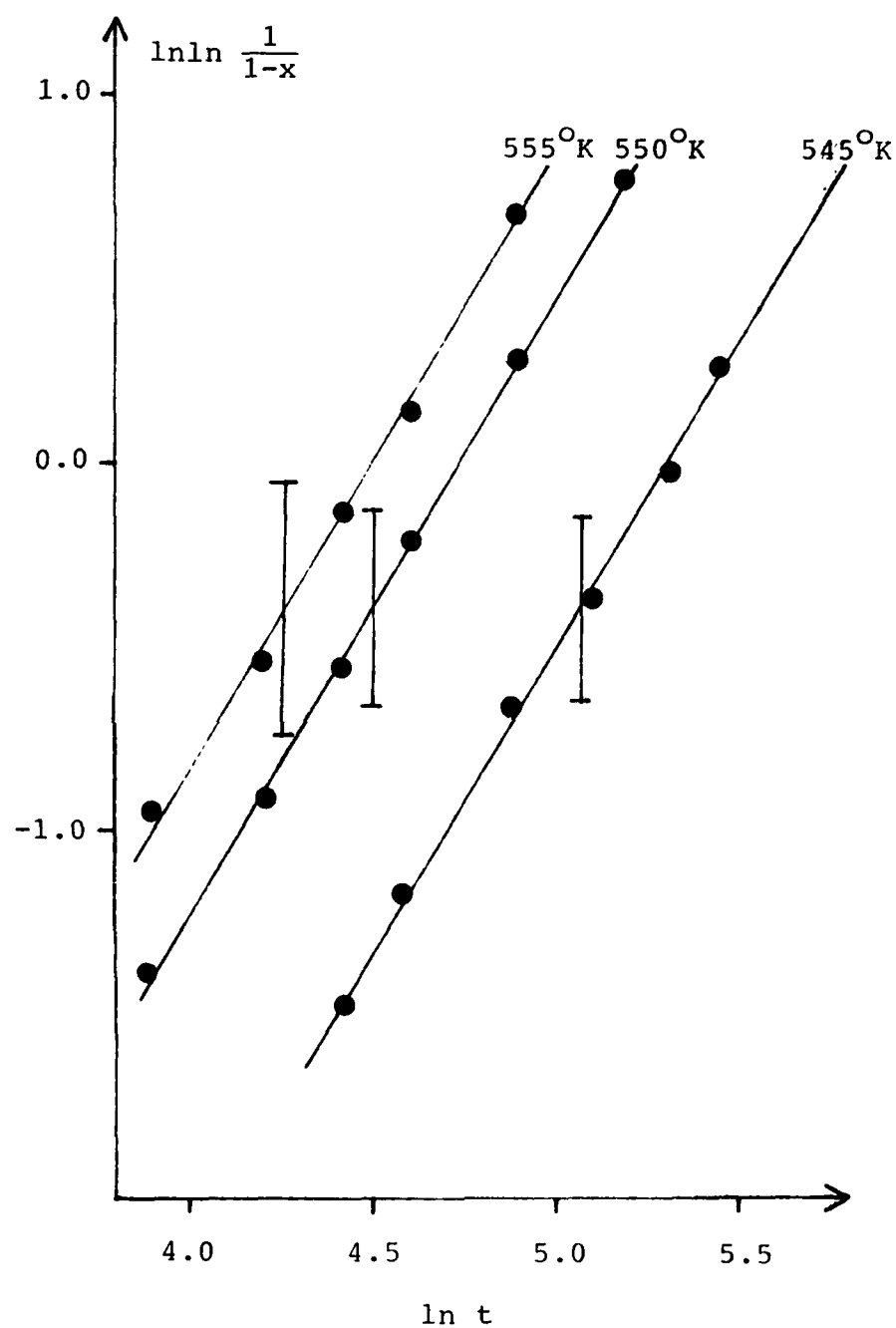


Figure 37e. Isothermal Crystallization Data for Activation Energy Calculation Step I ( $\text{As}_{0.4}\text{Sb}_{1.6}\text{S}_3$  Bulk).

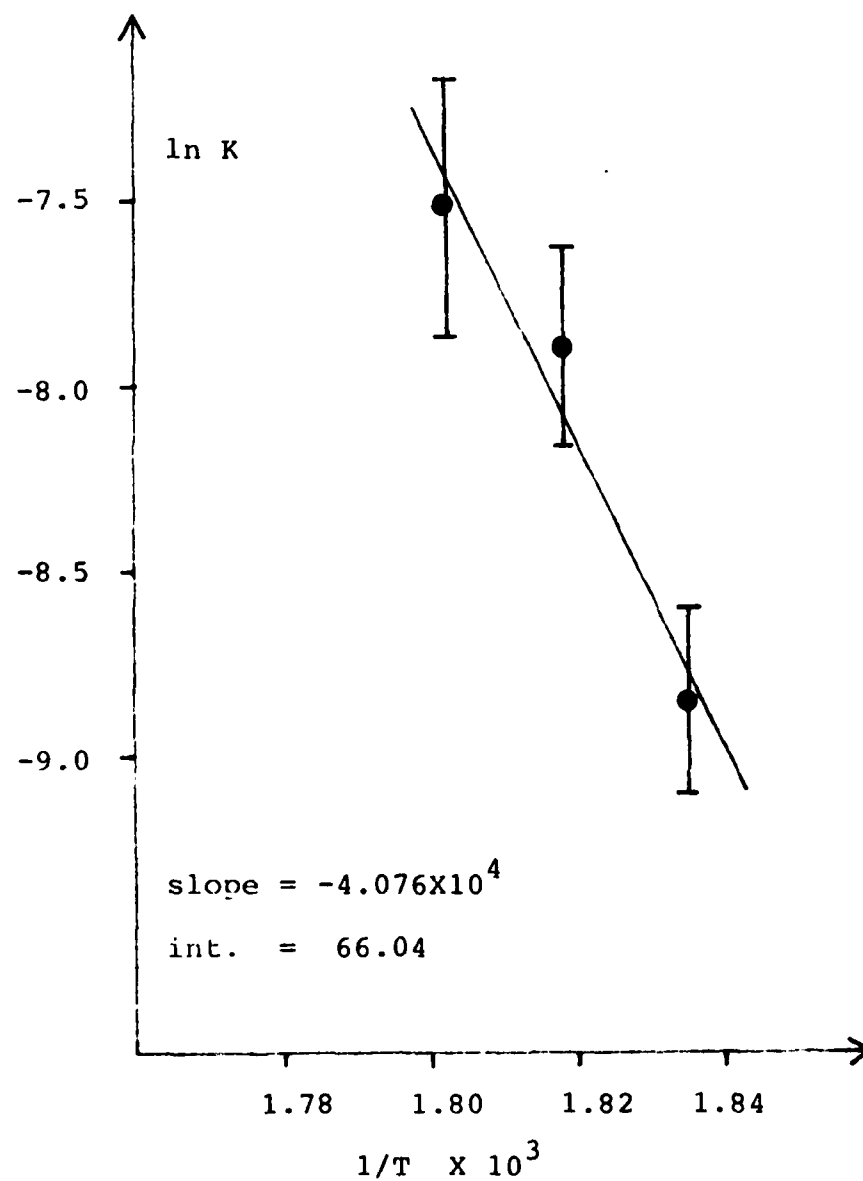


Figure 37f. Isothermal Crystallization Data for Activation Energy Calculation Step II ( $\text{As}_{0.4}\text{Sb}_{1.6}\text{S}_3$  Bulk).

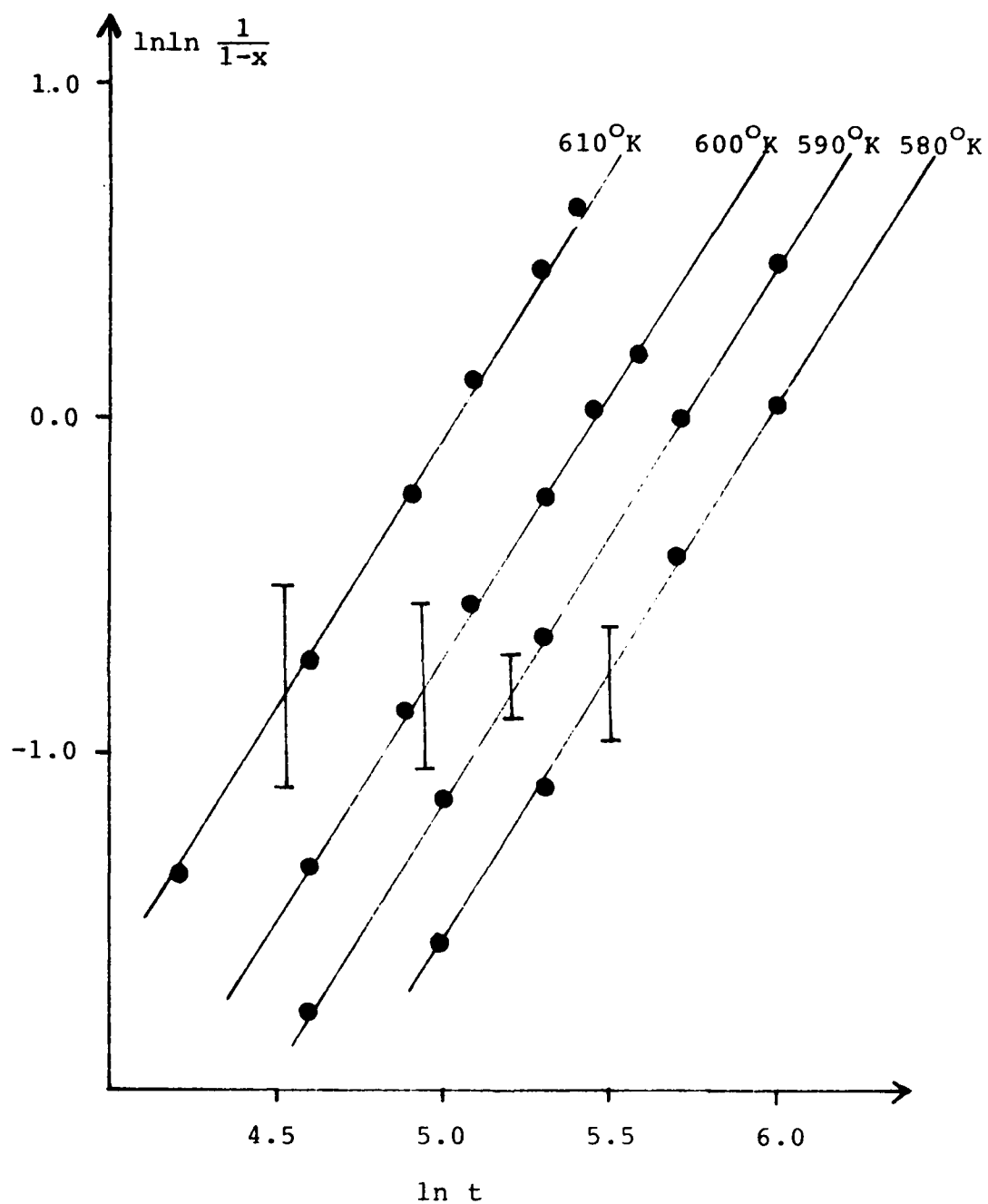


Figure 37g. Isothermal Crystallization Data for Activation Energy Calculation Step I ( $\text{As}_{1.2}\text{Sb}_{0.8}\text{S}_{2.55}^{\text{Bulk}}$ ).

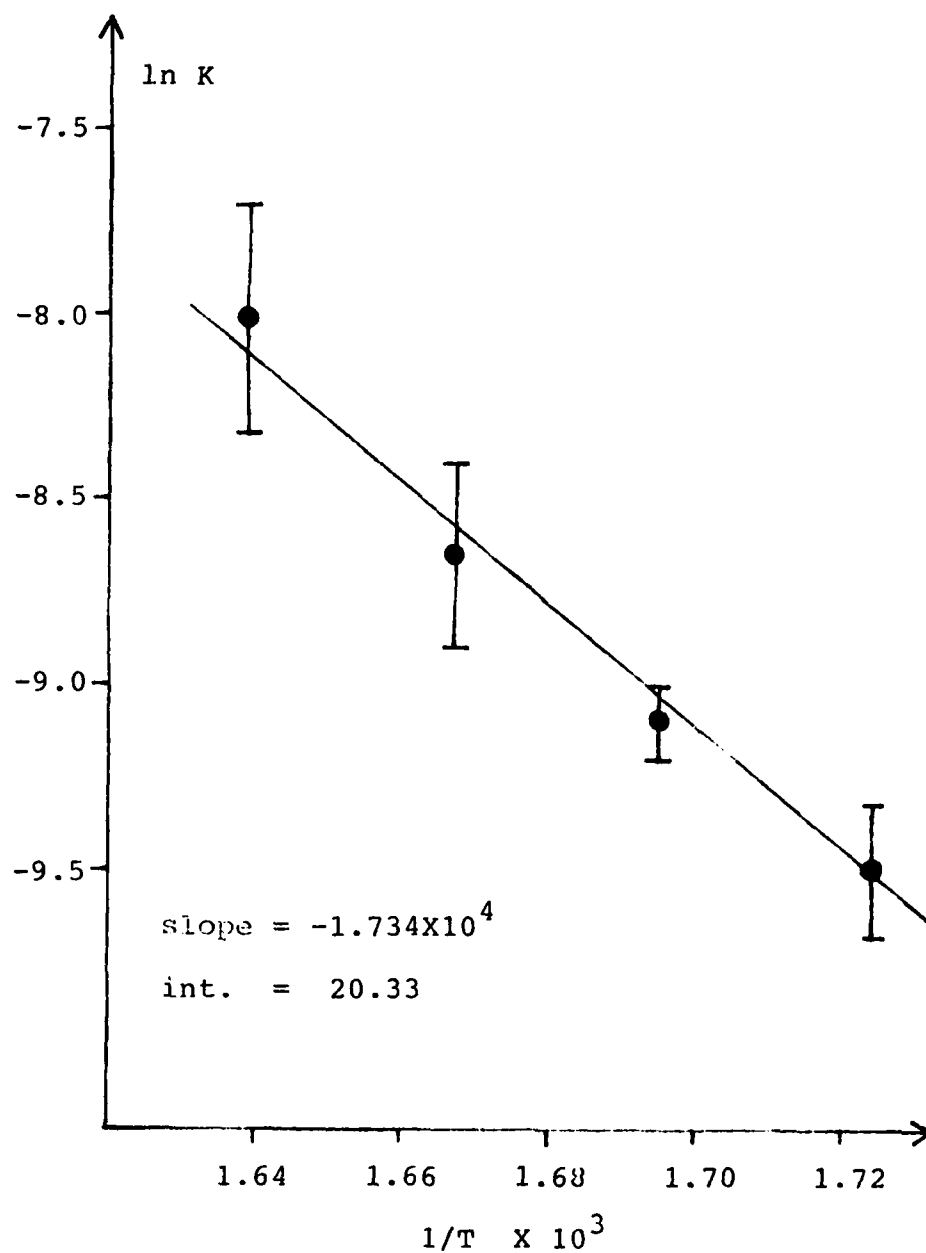


Figure 37h. Isothermal Crystallization Data for Activation Energy Calculation Step II ( $\text{As}_{1.2}\text{Sb}_{0.8}\text{S}_{2.55}$  Bulk).

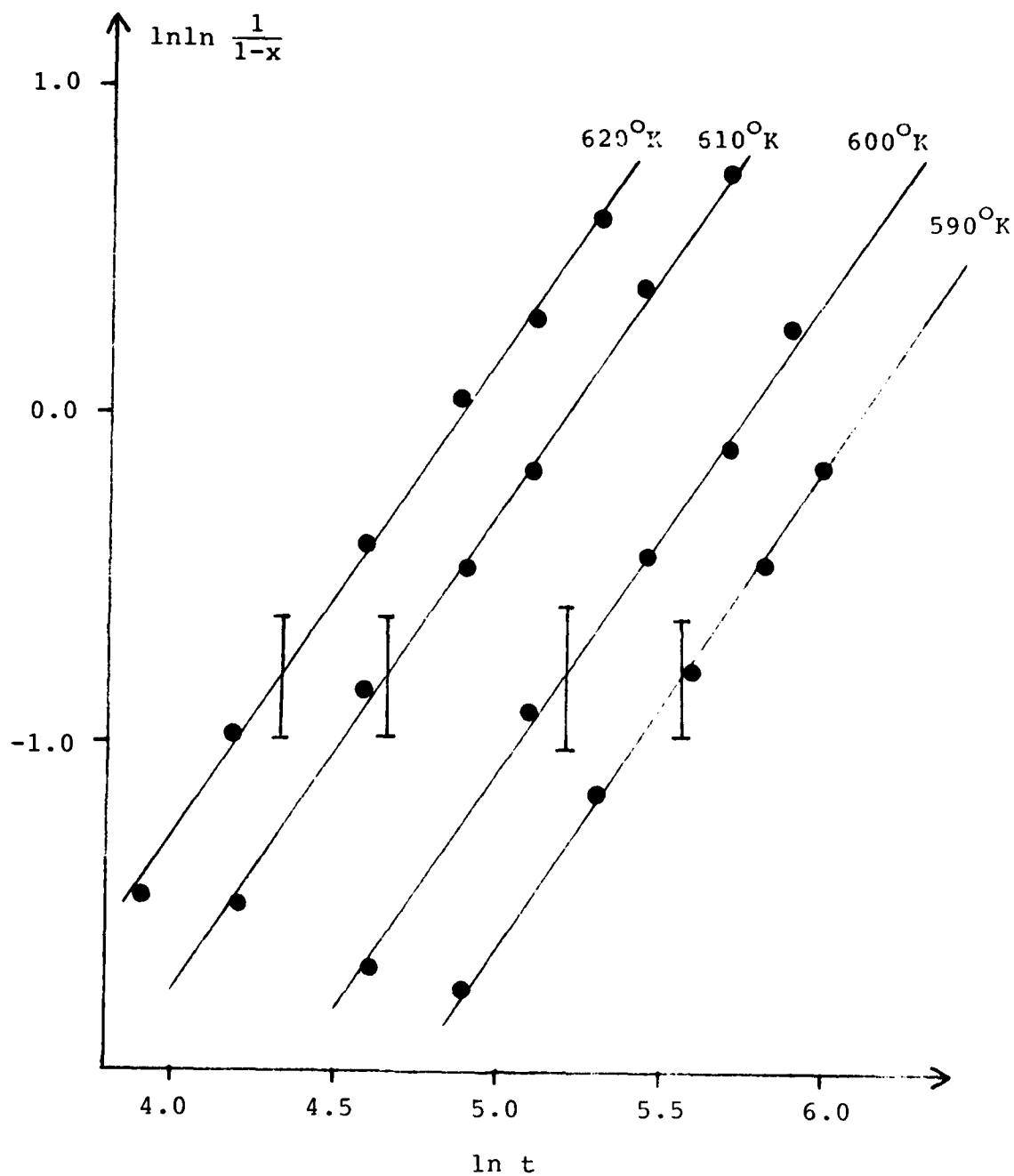


Figure 37i. Isothermal Crystallization Data for Activation Energy Calculation Step I ( $\text{As}_{1.0}\text{Sb}_{1.0}\text{S}_{2.67}^{\text{Bulk}}$ ).

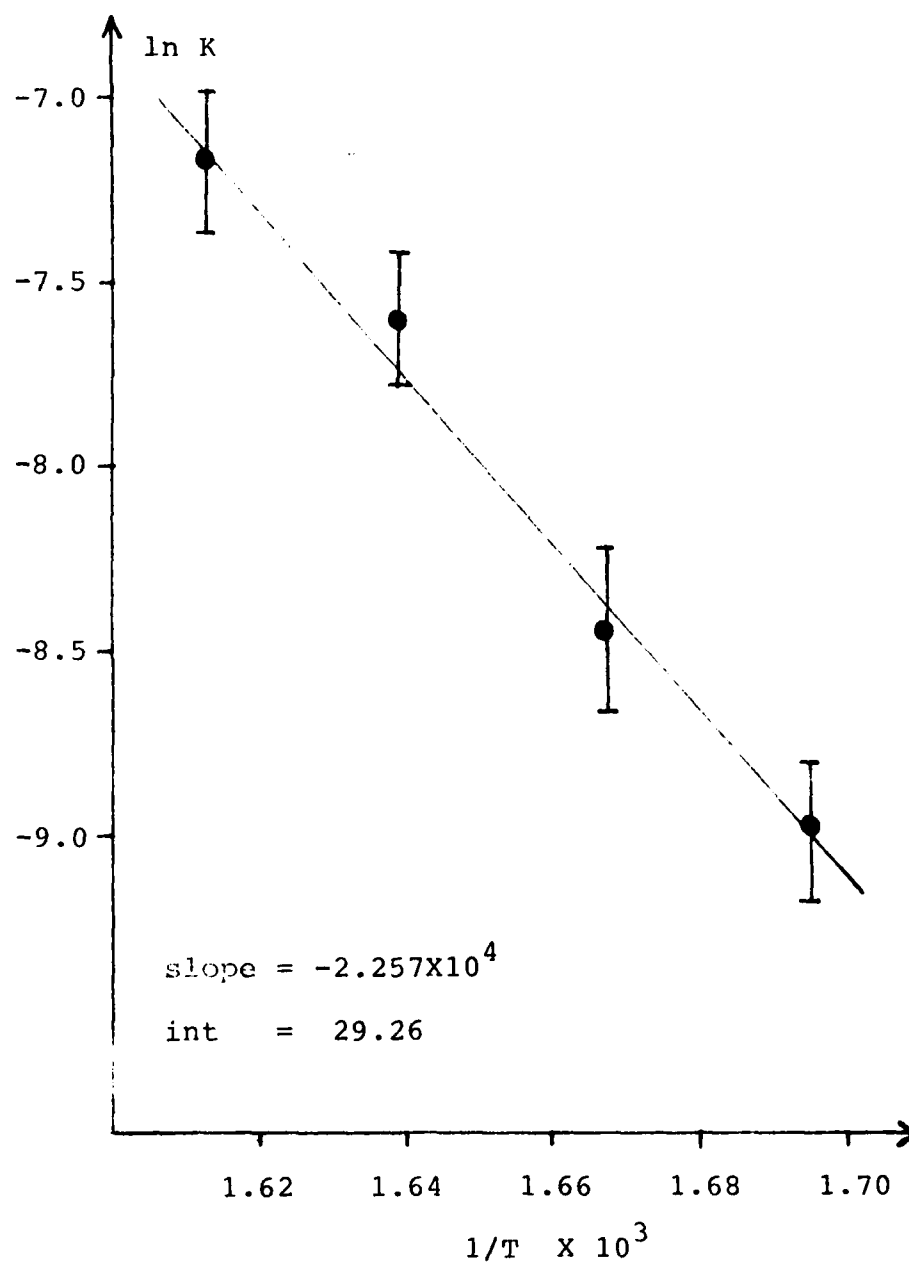


Figure 37j. Isothermal Crystallization Data for Activation Energy Calculation Step II ( $\text{As}_{1.0}\text{Sb}_{1.0}\text{S}_{2.67}^{\text{Bulk}}$ ).

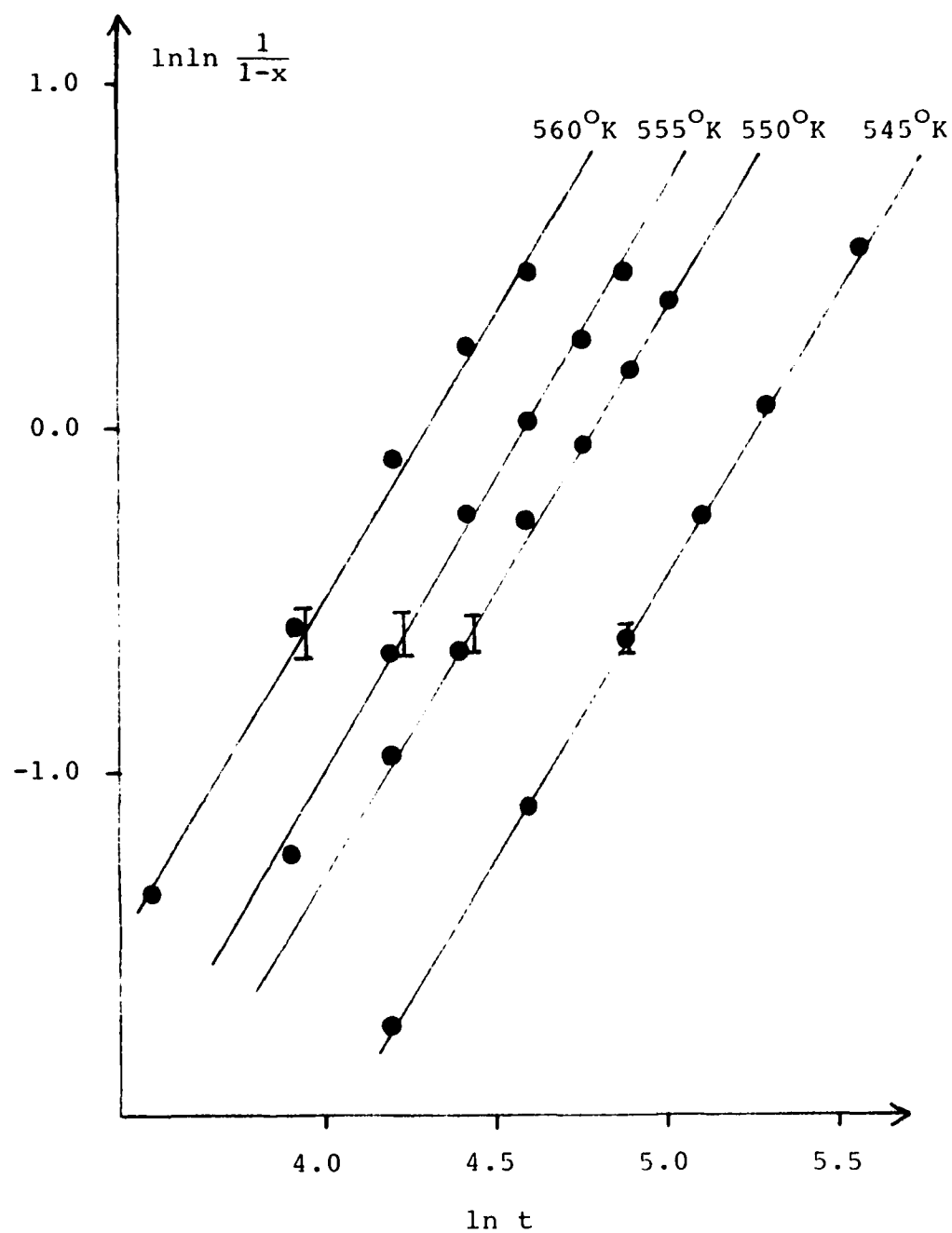


Figure 37k. Isothermal Crystallization Data for Activation Energy Calculation Step I ( $\text{As}_{0.8}\text{Sb}_{1.2}\text{S}_3$  Film).

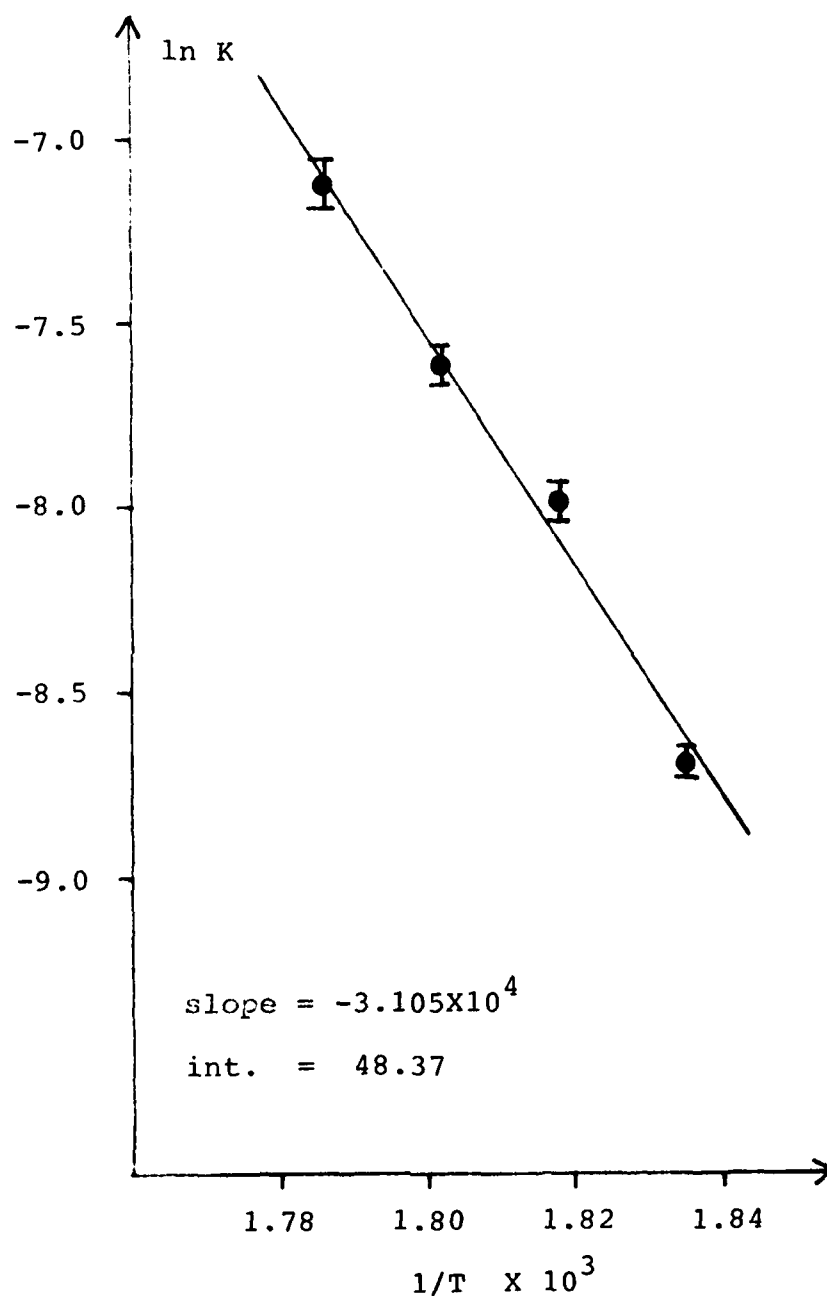


Figure 371. Isothermal Crystallization Data for Activation Energy Calculation Step II ( $\text{As}_{0.8}\text{Sb}_{1.2}\text{S}_3$  Film).

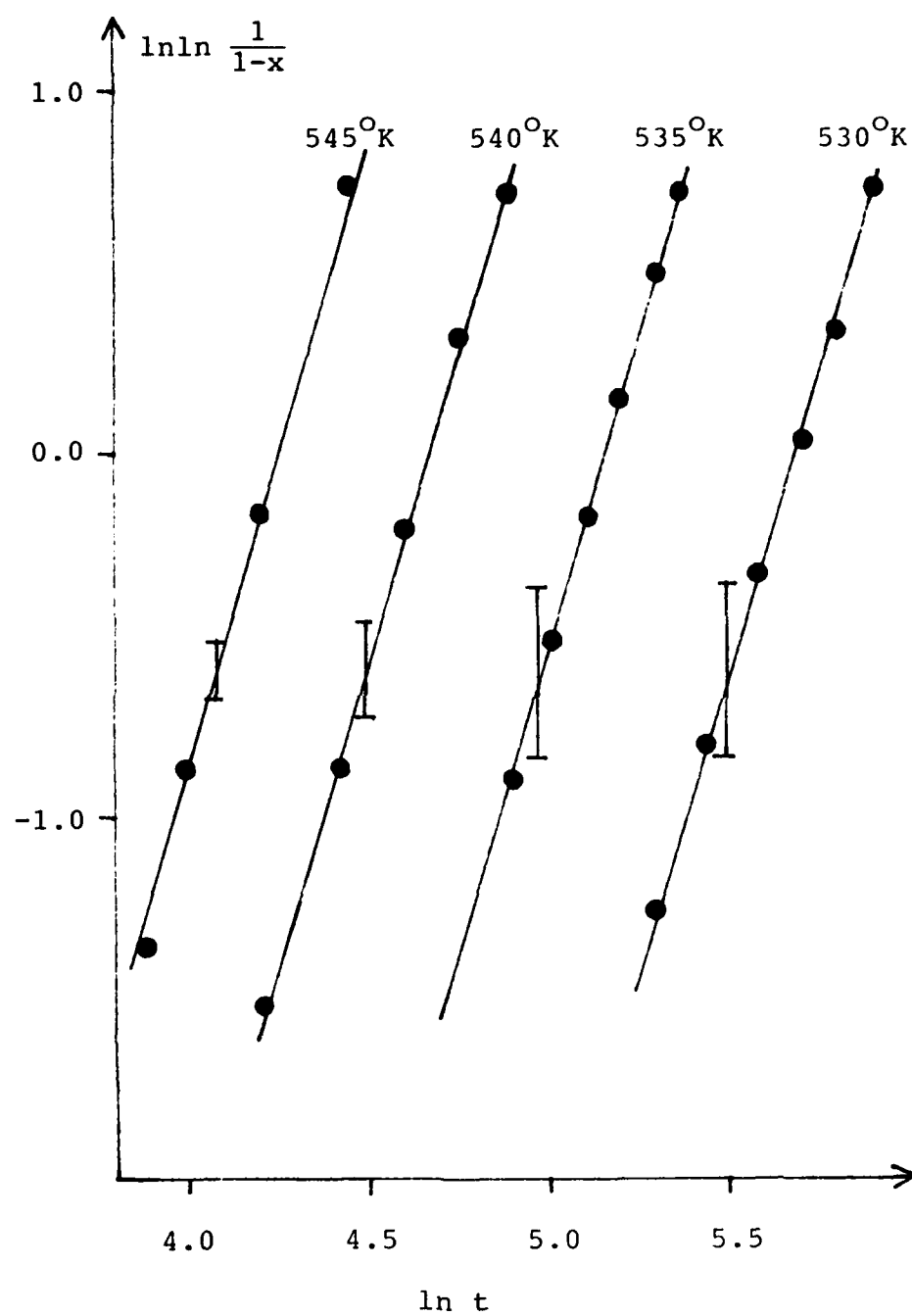


Figure 37m. Isothermal Crystallization Data for Activation Energy Calculation Step I ( $\text{As}_{0.4}\text{Sb}_{1.6}\text{S}_3$  Film).

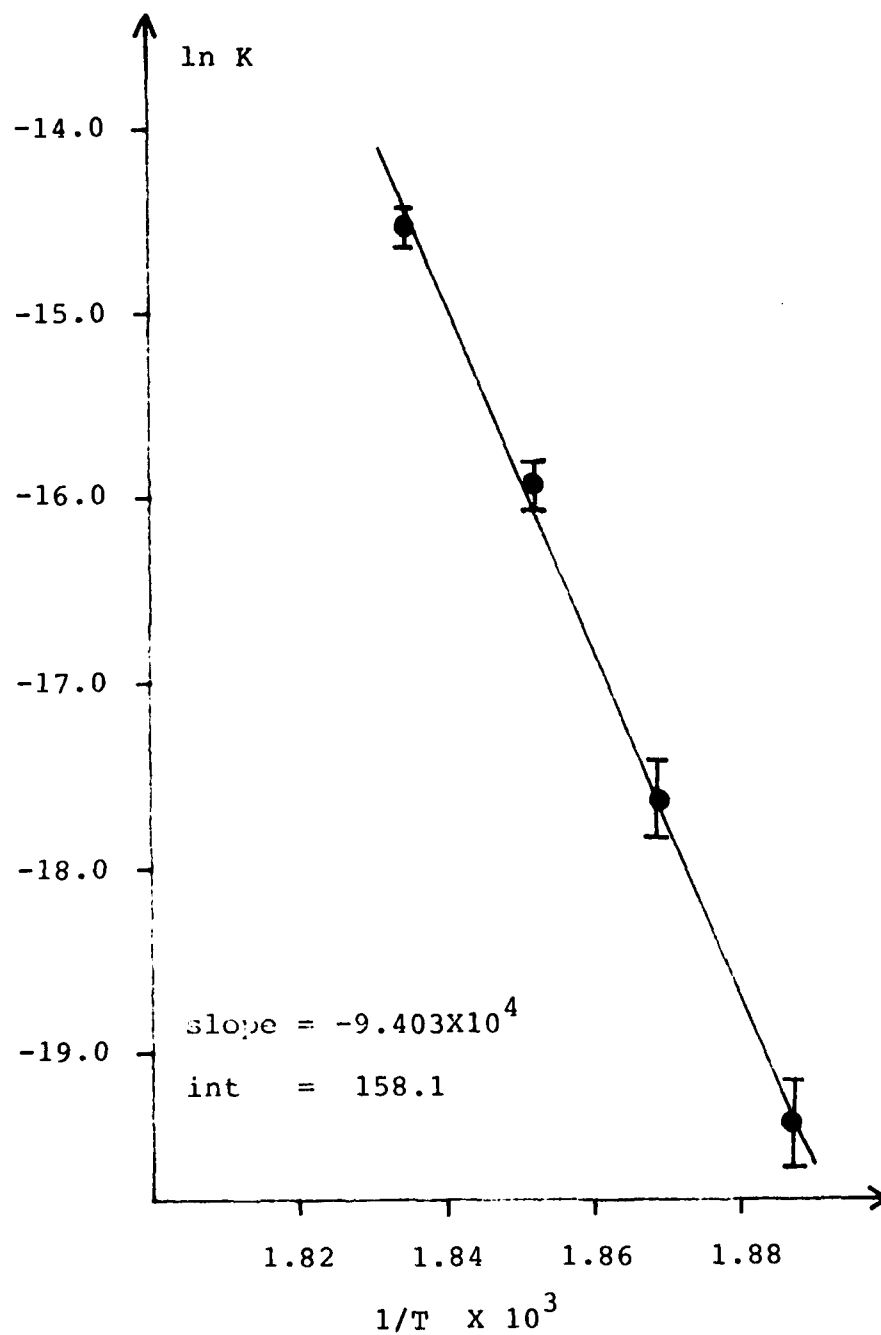


Figure 37n. Isothermal Crystallization Data for Activation Energy Calculation Step II ( $\text{As}_{0.4}\text{Sb}_{1.6}\text{S}_3$  Film).

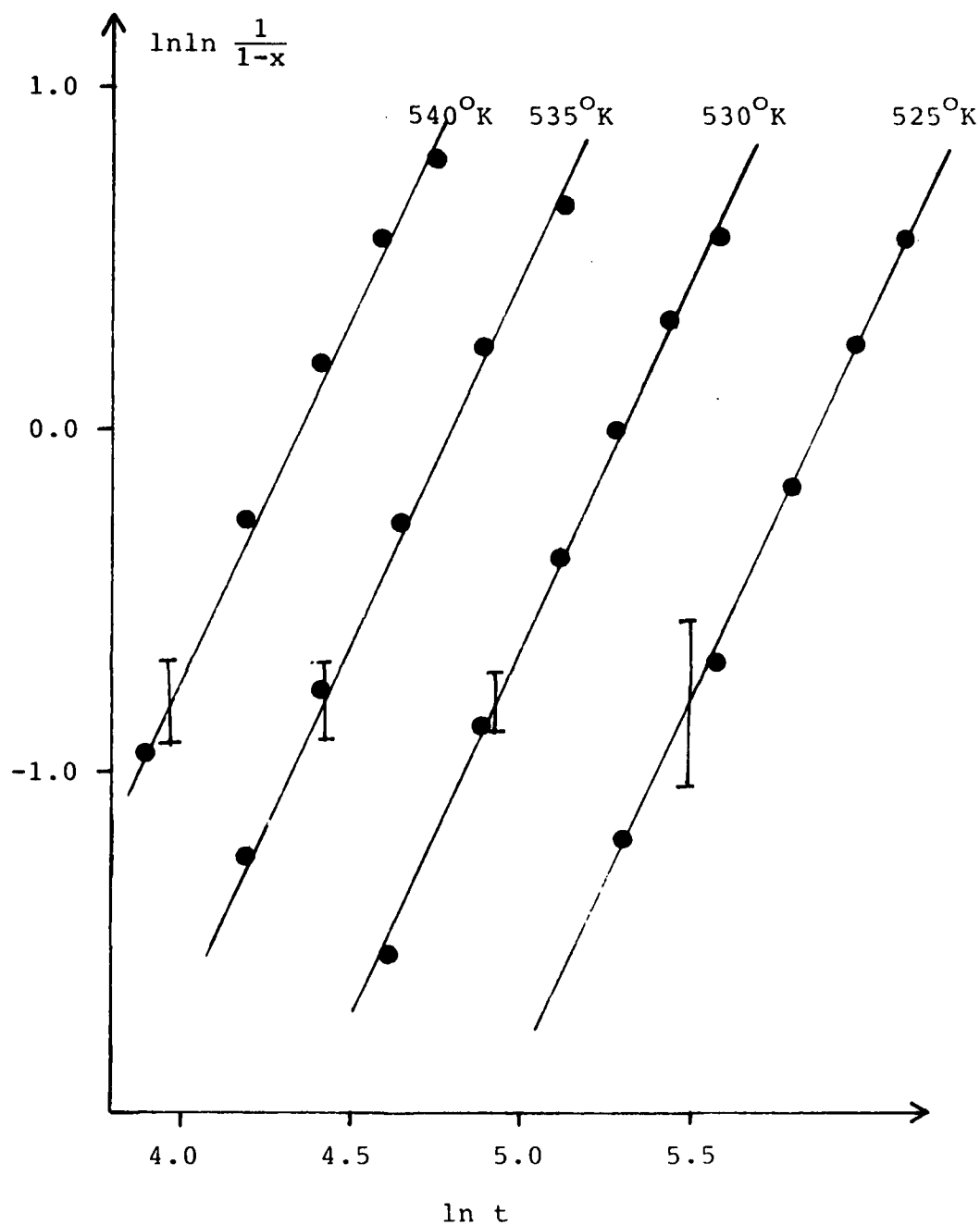


Figure 37o. Isothermal Crystallization Data for Activation Energy Calculation Step I ( $\text{Sb}_2\text{S}_3$  Film).

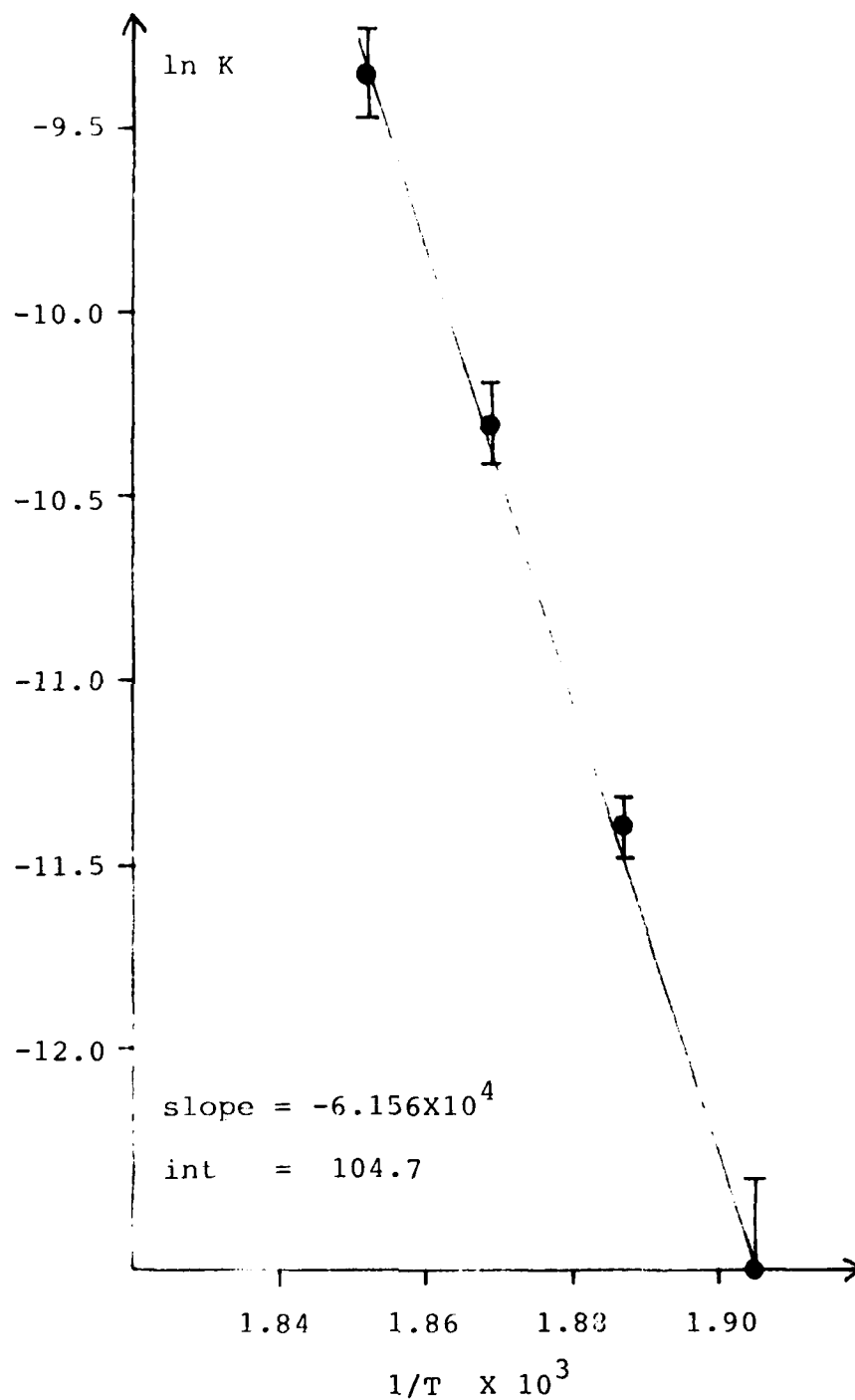


Figure 37p. Isothermal Crystallization Data for Activation Energy Calculation Step II ( $\text{Sb}_2\text{S}_3$  Film).

# REFERENCES

1. White, K., Chalcogenide Glasses (Part III), Chalcogenide Glass-Forming System, U.S. Air Force Report, AFWAL-TR-85-4122 (1985)
2. Rawson, H., Inorganic Glass Forming System, Non-Metallic Solids, Academic Press (1967)
3. Uhlmann, D.R. and Kreidl, N.J., Glass Science and Technology, vol.1, Glass Forming System, Academic Press, (1983)
4. Goriunova, N.A., Kolomiets, B.T. and Shilo, V.P., Soviet Phys. Tech. Phys., 3 (1958) 912-916
5. Kawamoto, Y. and Tsuchinashi, S., Yogyo-Kyokai-Shi, vol.7, No.10 (1969) 328-335
6. Kawamoto, Y. and Tsuchihashi, S., Yogyo-Kyokai-Shi, vol.79, No.3 (1971) 264-269
7. Tichy, L., Triska, A., Frumar, M., Ticha, H., and Klikorka, J., J. Non-Crystalline Solids, 59 (1982) 371-378
8. Berkes, J.S. and Myers, M.B., J. Electrochem. Soc., 118 (1971) 1485-1491
9. Orlova, G.M., Rasine, O.Z., and Krivenkova, N.P., J. Appl. Chem. USSR, vol.47, No.3 (1974) 510-513
10. Myers, M.B. and Berkes, J.S., J. Non-Crystalline Solids, 8-10 (1972) 804-815
11. Platakis, N.S. and Gatos, H.C., J. Electrochem. Soc., 119 (1972) 914-920
12. Das, G.C., Platakis, N.S., and Bever, M.B., J. Non-Crystalline Solids, 15 (1974) 30-44
13. Thornburg, D.D. and Johnson, R.L., J. Non-Crystalline Solids, 17 (1975) 2-8
14. Henderson, D.W. and Ast, D.G., J. Non-Crystalline Solids, 64 (1984) 43-70
15. El-Fouly, M.H. and Edmond, J.T., Phys. Stat. Sol. (a), 21 (1974) K43

16. Kingery, W.D., Bowen, H.K., and Uhlmann, D.R.,  
Introduction to Ceramics, 2nd ed., John Wiley & Sons  
(1976)
17. Trzebiatowski, W. and Bryjak, E., Z. Anorg. Chem.,  
238 (1938) 255-267
18. Kittel, C., Introduction to Solid State Physics, 4th  
ed., John Wiley & Sons (1971)
19. Search Manual, Powder Diffraction File, by Joint  
Committee on Powder Diffraction Standards, USA (1976)
20. Cahn, J.W., J. Am. Ceram. Soc., 52 (1969) 118
21. Uhlmann, D.R., J. Non-Crystalline Solids, 38-39 (1980)  
693-698
22. Zaluska, A., Zaluski, L., and Lasocka, M., J. Thermal  
Anal. vol.19 (1980) 257-262
23. Burke, J., The Kinetic of Phase Transformations in  
Metals, Pergamon press (1965)
24. Christian, J.W., The Theory of Transformations in  
Metals and Alloys, 2nd ed., Pergamon Press (1975)
25. Surinach, S., Baro, M.D., Clavaguera-Mora, M.T., and  
Clavaguera, n., J. of Non-Crystalline Solids, 58 (1983)  
209-217
26. Avrami, M., J. of Chem. Phys., 7 (1939) 1103-1112
27. Avrami, M., J. of Chem. Phys., 8 (1940) 212-224
28. Avrami, M., J. of Chem. Phys., 9 (1941) 177-184
29. Johnson, W.A. and Mehl, K.L., Trans. Am. Inst. Mining  
Met. Engns. 135 (1981) 315
30. Kemery, T. and Granasy, L., J. of Non-Crystalline  
Solids, 68 (1984) 193-202
31. De Bruijn, T.J.W., De Jong, W.A., and Von Den Berg,  
P.J., Thermochimica Acta, 45 (1981) 315-325
32. Henderson, D.W., J. Thermal Anal. vol.15 (1979) 325-331
33. Platakis, N.S., Sadagopan, V., and Gatos, H.C., J. of  
Electrochem. Soc. 116 (1969) 1436-143

34. Coutts, M.D. and Levin, E.R., J. of Appl. Phys., 38 (1967) 4039-4044
35. Hafiz, M.M., Ammar, A.A., and Hammad, F.H., Thin Solid Films, 60 (1979) 371-376
36. Rysava, N., Tichy, L., Barta, C., Triska, A. and Ticha, H., Phys. stat. sol. (a), 87, (1985) K13
37. Ramanan, V.R.V. and Fish, G.E., J. Appl. Phys., 53 (3) (1982) 2273-2275
38. Ozawa, T., Polymer, vol.12 (1971) 150-158
39. Moynihan, C.T., Easteal, A.J., Wilder, J., and Tucker, J., J. Phys. Chem., vol.78, No.26 (1974) 2673-2677
40. Schnaus, U.E., Moynihan, C.T., Gammon, R.W. and Macedo, P.B., Phys. Chem. Glasses, vol.11, No.6 (1970) 213-218
41. Moynihan, C.T., Easteal, A.J., DeBolt, M.A., and Tucker, J., J. Am. Ceram. Soc., vol.59 (1976) 12-15
42. DeBolt, M.A., Easteal, A.J., Macedo, P.B., and Moynihan, C.T., J. Am. Ceram. Soc., vol.59 (1976) 16-21
43. Easteal, A.J., Wilder, J.A., Mohr, R.K., and Moynihan, C.T., J. Am. Ceram. Soc., vol.60 (1977) 134-138
44. Ludwig, W., Voight, B., Lippmann, H.J. and Feltz, A., Thermal Analysis, vol.1 (1974) 893-903
45. Nunoshita, M., Arai, H., Hamanaka, Y. and Fujimoto, T., Amorphous and Liquid Semicond., vol.2 (1974) 753-759
46. Petrie, S.E.B., J. Polymer Science: part A-2, vol. 10, (1972) 1255-1272
47. Miller, I. and Freund, J.E., Probability and Statistics for Engineers, 2'nd ed., Prentice-Hall, Inc. (1977)
48. Fyans, R.L., The Perkin-Elmer Instrument News, order No.MA-8A (1975) 31-32
49. Jonker, W.P.A., Z. Anorg. Chem., 62 (1909) 89-107
50. Shimakawa, K., Baba, T., and Arizumi, T., Jap. J. Appl. Phys., 10 (1971) 1116-1117

51. Abrikosov, N., Bankina, V.F., Poretskaya, L.V., Shelimova, L.E., Skudnova, E.V., Semiconducting II-VI, IV-VI, and V-VI Compound, Monograms in Semiconductor Physics, Plenum Press, NY (1969)
52. Chen, C.H., Phillips, J.C., Tai, K.L. and Bridenbaugh, P.M., Solid State Comm., vol.38 (1981) 657-661
53. Thoeni, W.P., Thin Solid Films, 88 (1982) 385-397
54. Zdanowicz, L. and Miotkowska, S., Thin Solid Films, 29 (1975) 177-183
55. Al-Douri, A.A.J. and Heavens, O.S., Thin Solid Films, 100 (1983) 273-281
56. Nakhodkin, N.G. and Shaldervan, I., Thin Solid Films, 10 (1972) 109-122
57. Nakhodkin, N.G., Bardamid, A.F. and Novoselskaya, A.I., Thin Solid Films, 112 (1984) 267-277
58. Aziz, R.A. and Scott, G.D., Canadian J. of Phys., vol.34 (1956) 731-736
59. Apling, A.J. and Leadbetter, A.J., Amorphous and Liquid Semiconductors, Proc. Int. Conf. 5'th, ed; Stuke, J., vol.1 (1974) 457-462
60. Leadbetter, A.J., Apling, A.J., and Daniel, M.F., J. Non-Crystalline Solids, 21 (1976) 47-53
61. Apling, A.J., Leadbetter, A.J., and Wright, A.C., J. Non-Crystalline Solids, 23 (1977) 369-384
62. Martin, T.P., Solid State Comm., vol.47, No.2 (1983) 111-114
63. Nemanich, R.J., Connell, G.A.N., Hayes, T.M., and Street, R.A., Phys. Rev. B18, (1978) 6900-6914
64. Street, R.A., Nemanich, R.J., and Connell, G.A.N., Phys. Rev. B18, (1978) 6915-6919
65. Tohge, N., Kimoto, M., Minami, T., and Tanaka, M., yogyo- Kyokai-shi, 90 [3] (1982) 133-138
66. Daniel, M.F., Leadbetter, A.J., Wright, A.C., and Sinclair, R.N., J. Non-Crystalline Solids, 32 (1979) 271-293

67. Kumar, B. and White, K., Study on Chalcogenide Films,  
U.S. Air force Report, AFWAL-TR-85-4046 (1985)

END

10-86

DTIC